



**WICHITA STATE
UNIVERSITY**

UNIVERSITY LIBRARIES

**Comparison of finite element analysis of impact
on water and soil using Lagrangian, ALE, and SPH
approaches and airframe impact applications**

Item Type	Thesis
Authors	Seetamsetti, Arun Santosh
Publisher	Wichita State University
Rights	Copyright Arun Santosh Seetamsetti, 2012. All rights reserved
Download date	2026-05-20 05:01:57
Link to Item	http://hdl.handle.net/10057/5421

**COMPARISON OF FINITE ELEMENT ANALYSIS OF IMPACT ON WATER AND
SOIL USING LAGRANGIAN, ALE, AND SPH APPROACHES
AND AIRFRAME IMPACT APPLICATIONS**

A Thesis by
Arun Santosh Seetamsetti
Bachelor of Engineering, Jawaharlal Nehru Technological University, 2007

Submitted to the Department of Mechanical Engineering
and the faculty of the Graduate School of
Wichita State University
in partial fulfillment of
the requirements for the degree of
Master of Science

May 2012

© Copyright 2012 by Arun Santosh Seetamsetti
All Rights Reserved

**COMPARISON OF FINITE ELEMENT ANALYSIS OF IMPACT ON WATER AND
SOIL USING LAGRANGIAN, ALE AND SPH APPROACHES
AND AIRFRAME IMPACT APPLICATIONS**

The following faculty members have examined the final copy of this thesis for form and content, and recommend that it be accepted in partial fulfillment of the requirement for the degree of Master of Science with a major in Mechanical Engineering.

Hamid M. Lankarani, Committee Chair

Krishna Krishnan, Committee Member

Michael McCoy, Committee Member

DEDICATION

To my parents and sister for their continuous encouragement, love, and support
and to my dear friends

ACKNOWLEDGEMENTS

I express my sincere gratitude to my advisor, Dr. Hamid Lankarani, Professor of Mechanical Engineering, for his support, encouragement, and timely guidance throughout my graduate studies at Wichita State University. His continuous assistance made possible the successful completion of my thesis. I also express my gratefulness to Dr. Krishna Krishnan and Dr. Michael McCoy for being members of my thesis committee.

This thesis would not have been possible without Mr. Rasoul Moradi and Ms. Lavanya Vemuri—thank you so much for your valuable suggestions. I also thank Mr. Nilesh Dhole for his technical discussions and suggestions. It is with pleasure that I thank each and everyone who helped me in completing this research and making this thesis possible. I am indebted to all my colleagues from Wichita State University Library for their continual help during my research project.

Lastly, I am gratefully to my mother, father, sister, and relatives for their unconditional support and encouragement throughout my graduate studies. I would also like to convey respect to my late grandfathers and uncle, who inspired me to pursue graduate studies. I thank my friends in the United States and India for providing me emotional and moral support during my studies in Wichita. And special thanks go to my friends—Ms. Rohitha, Mr. Murali, and Mrs. Chris Feeny.

ABSTRACT

According to Federal Aviation Administration (FAA) reports on aircraft accidents, 80 percent of all crashes occur on water and land. The research in this thesis used computational finite element modeling and analysis to study the effects of impacts on water and soft soil with respect to the structural integrity of an aircraft's airframe during a crash. The effects of these impacts play a vital role in the design phase of an aircraft.

The objective of this research was to compare the computational finite element technique for impact on water and soil, and to correlate it with the experiments. The nonlinear explicit finite element code together with the equation of state (EOS) and fluid-structure interaction (FSI) are used in the arbitrary Lagrangian-Eulerian (ALE) technique. A validation study of water and soft-soil properties on impact analyses was carried out in three different experimental phases using the following: a rigid spherical ball, a penetrometer, and a flask ball. Finally, an airframe structure study was conducted in water and soil. Initially, the impact simulations were carried out using Lagrangian analysis, followed by the ALE technique, and then the smoothed particle hydrodynamics (SPH) method. Acceleration was observed as an important parameter to validate in the analysis. Both ALE and SPH methods showed more accurate results than those obtained using Lagrangian analysis and were similar to that of the experimental data. Comparing the results from analyzing water and soil impacts with a rotorcraft indicated that water impact produces 33% less g-value and around 90% deformation compared to soil impact, thus indicating that impact on a water surface might be safer than impact on a soil surface. The impact study on water and soil was intended to evaluate the general behavior of the deformation, or g-value, for structural analyses only, and results show that the Lagrangian approach is recommended, if the soil and water is of small interest.

TABLE OF CONTENTS

Chapter	Page
1. INTRODUCTION	1
1.1 Background.....	1
1.1.1 Review of Airplane Accidents	1
1.1.2 Review of Rotorcraft Accidents.....	4
1.2 Aircraft Ditching Certification.....	5
1.2.1 Airplane Ditching Regulations	6
1.2.2 Rotorcraft Ditching Regulations.....	7
1.3 Motivation for This Study.....	8
1.4 Literature Review.....	11
1.5 Objective of Thesis	21
1.6 Organization of Thesis.....	21
2. FINITE ELEMENT METHOD AND METHODOLOGY	23
2.1 Finite Element Method	23
2.1.1 Lagrangian Technique	25
2.1.2 Eulerian Technique.....	25
2.1.3 Arbitrary Lagrangian-Eulerian Technique.....	26
2.1.4 Smoothed Particle Hydrodynamics Technique.....	27
2.2 Finite Element Methodology	29
3. MODEL DEVELOPMENT AND VALIDATION OF IMPACT ON WATER	31
3.1 Water Properties.....	32
3.2 Model Development and Validation of Water Impact Analysis Using Rigid Sphere	32
3.2.1 Lagrangian Approach for Water Impact Analysis Using Rigid Sphere	35
3.2.2 ALE Approach for Water Impact Analysis Using Rigid Sphere.....	37
3.2.3 SPH Approach for Water Impact Analysis Using Rigid Sphere	39
3.3 Model Development and Validation of Water Impact Analysis Using Ball and Flask.....	41
3.3.1 Lagrangian Approach for Water Impact Analysis Using Ball and Flask.....	41
3.3.2 ALE Approach for Water Impact Analysis Using Ball and Flask.....	43
3.3.3 SPH Approach for Water Impact Analysis Using Ball and Flask	44
3.4 Model Development and Validation of Water Impact Analysis Using Penetrometer	46
3.4.1 Lagrangian Approach for Water Impact Analysis Using Penetrometer	47
3.4.2 ALE Approach for Water Impact Analysis Using Penetrometer.....	48
3.4.3 SPH Approach for Water Impact Analysis Using Penetrometer	49

TABLE OF CONTENTS (continued)

Chapter	Page
4. MODEL DEVELOPMENT AND VALIDATION OF IMPACT ON SOIL	51
4.1 Validation of Soft Soil Properties	51
4.2 Model Development and Validation of Soft Soil Impact Analysis Using Penetrometer	52
4.2.1 Lagrangian Approach for Soft Soil Impact Analysis Using Penetrometer	52
4.2.2 ALE Approach for Soft Soil Impact Analysis Using Penetrometer	54
4.2.3 SPH Approach for Soft Soil Impact Analysis Using Penetrometer	56
5. APPLICATION OF AIRPLANE AND HELICOPTER IMPACT ON WATER AND SOFT SOIL	58
5.1 Rotorcraft Impact Application	58
5.1.1 Rotorcraft Water Impact	58
5.1.2 Rotorcraft Soil Impact	64
5.2 Airplane Impact Application	69
5.2.1 Airplane Soil Impact	69
5.2.3 Airplane Water Impact	74
6. MODEL COMPARISON, RESULTS, AND DISCUSSION	80
6.1 Water Impact Simulation	80
6.1.1 Rigid Ball Impact on Water	80
6.1.2 Ball Impact on Water in Flask	81
6.1.3 Penetrometer Impact on Water Surface	82
6.2 Soil Impact Simulation	83
6.3 Rotorcraft Impact Simulation	84
6.3.1 Rotorcraft Impact on Water	84
6.3.2 Rotorcraft Impact on Soil	85
6.4 Airplane Impact Simulation	86
6.4.1 Airplane Impact on Soil	86
6.4.2 Airplane Impact on Water	87
6.5 Summary	88
7. CONCLUSIONS AND FUTURE RECOMMENDATIONS	90
7.1 Conclusions	90
7.2 Future Recommendations	91
LIST OF REFERENCES	93

LIST OF TABLES

Table	Page
1.1	Number of Incidents from 1943 to Present Resulting from Various Factors, [1, 2].....2
1.2	Accidents on Water and Land Reported by FAA for 2006 [5].....3
1.3	Water-Impact Accidents from 1959 to 2006 [5, 9].....3
1.4	Data Characterizing Controlled Ditching, Vertical Descent with Limited Control, and Fly-In Impact [11].3
1.5	Rotorcraft Landings on Different Terrain and Percentage of Occurrence [15].4
1.6	Rotorcraft Landings on Soft Surfaces and Percentage of Occurrence [15].5
1.7	Apparatus Used in Experiment [32].16
3.1	Material Properties of Water Used in Water Impact Analysis [9, 40].....33
3.2	Linear Polynomial Parameters [9].33
3.3	Grüneisen Parameters in Case 2 [41].....34
3.4	Material Properties of Rigid Body Used in Water Impact Analysis [24].34
3.5	Material Properties of Air Used in ALE Technique [35].37
3.6	Material Properties of Rigid Ball Used in Flask Experiment [26].....41
3.7	Material Properties of Penetrometer Used in Water Impact Analysis [23].46
4.1	Material Properties of Penetrometer Used in Soil Impact Analysis [30].....51
4.2	Material Properties of Soil Used in Soil Impact Analysis [30].51
5.1	Material Properties of Rotorcraft [32].60
5.2	Material Properties of Airplane [27].....70
6.1	Summary of G-Values90
6.2	Computation Time for Simulation (8 core CPU in HIPECC)89
6.3	Deformation of Rotorcraft.89

LIST OF FIGURES

Figure	Page
1.1. Landing of aircraft on water surface [16].	6
1.2. Energy absorption in rigid surface impact (a) and soft surface impact (b) [15].	9
1.3. FEM representation: (a) ball test experiment, (b) graphical representation of ball test experiment, and (c) quarter model of fuselage after impact in water pit [23].	12
1.4. Test setup with penetrometer [28].	13
1.5. Graphical FEM representation of penetrometer test [31].	13
1.6. Apparatus used in hydrodynamic impact experiment: (a) ball and flask, (b) capture of ball impacting flask, and (c) graphical FEM representation of ball and flask experiment [32].	15
1.7. Test setup of tri-axial compression test on soil [19].	16
1.8. Test site for soil test [19].	17
1.9. Graphical representation of test data in acceleration [19].	17
1.10. Angles in aircraft landing [35].	18
1.11. Test setup of rotorcraft: (a) initially, (b) raised to a certain height, and (c) subjected to impact [36].	19
1.12. Test setup for vertical drop test [36].	19
1.13. Accelerometer data: (a) experimental results of helicopter impacting water [36], (b) ALE results obtained by Randhawa experiment using LS-DYNA [32].	20
1.14. Structural damage: (a) bottom of helicopter frame, and (b) bulged panel on helicopter surface [36].	20
2.1. Langrangian mesh (L) and Eulerian mesh (E) and their deformation with respect to mesh and material [37].	25
2.2. Arbitrary Langrangian-Eulerian (ALE) mesh and its deformation with respect to mesh and material [37].	26

LIST OF FIGURES (continued)

Figure	Page
2.3 ALE block diagram [37].	27
2.4. Lagrangian, Eulerian, and ALE deformation with respect to nodes, material, nodal trajectory, and material point trajectory [37].	27
2.5 Kernel spline or function showing smoothing kernel between nodes (W), distance between nodes (r), diameter of particle (h), and mass (m) [38].	28
2.6. FEM methodology chart.	29
2.7 Methodology for validation of water and soft-soil impact analyses.	30
3.1. Mesh density and element size of rigid sphere: (a) mesh density of 14 and element size of 0.005 m, and (b) element size of 0.0125 m.	33
3.2. Lagrangian simulation of rigid body impact.	36
3.3 Graph of Lagrangian simulation with different material properties.	37
3.4. Mesh in ALE experiment setup.	38
3.5. ALE simulation of rigid body impact.	38
3.6. Graph of acceleration vs. time for rigid ball in ALE simulation.	39
3.7. SPH simulation of rigid body impact.	40
3.8. Graph of acceleration vs. time for rigid ball in SPH simulation.	40
3.9. Lagrangian simulation of ball and flask experiment.	42
3.10. Graph of displacement vs. time for ball in Lagrangian simulation.	42
3.11. ALE simulation of ball and flask experiment.	43
3.12. Graph of displacement vs. time for ball in ALE simulation.	44
3.13. SPH simulation of ball and flask experiment.	45
3.14. Graph of displacement vs. time for ball in SPH simulation.	45
3.15 Lagrangian simulation water impact analysis using penetrometer.	48

LIST OF FIGURES (continued)

Figure	Page
3.16. Graph of acceleration vs time for penetrometer in Lagrangian simulation. Case 1 mesh seeding was 110x110x23, and case 2 mesh seeding was 110x110x46.....	48
3.17 ALE simulation water impact analysis using penetrometer.	49
3.18 Graph of acceleration vs. time for penetrometer in ALE simulation.....	49
3.19 SPH simulation on water impact using penetrometer.....	50
3.20. Graph of acceleration vs time for penetrometer in SPH simulation. Case 1 mesh seeding was 110x110x23, and case 2 mesh seeding was 110x110x46.....	50
4.1 Stress vs. strain curve for soft soil [10].....	52
4.2. Test setup of soil impact analysis.	53
4.3. Lagrangian simulation of soil impact using penetrometer.....	54
4.4. Graph of acceleration vs. time for soil impact analysis in Lagrangian simulation.....	54
4.5 ALE simulation of soil impact using penetrometer.	55
4.6 Graph of acceleration vs. time for soil impact in ALE simulation.	56
4.7 SPH simulation of soil impact analysis using penetrometer.....	57
4.8 Graph of acceleration vs. time for soil analysis in SPH simulation.....	57
5.1. Dimensions of Huey UH1H helicopter [42].	58
5.2. Modeled rotorcraft using 7,066 shell elements.....	59
5.3 Lagrangian simulation of rotorcraft in water.	60
5.4. Deformation of rotorcraft.....	61
5.5 Graph of acceleration vs. time for rotorcraft in water in Lagrangian simulation.....	61

LIST OF FIGURES (continued)

Figure	Page
5.6 ALE simulation of rotorcraft in water.	62
5.7. Graph of acceleration vs. time for rotorcraft in water in ALE simulation.....	62
5.8. SPH simulation of rotorcraft in water.....	63
5.9. Graph of acceleration vs. time for rotorcraft in water in SPH simulation.....	64
5.10. Deformation of rotorcraft in soil.....	64
5.11. Lagrangian simulation of rotorcraft in soil.....	65
5.12. Graph of acceleration vs. time for rotorcraft in soil in Lagrangian simulation.....	66
5.13. ALE simulation of rotorcraft in soil.....	67
5.14. Graph of acceleration vs. time for rotorcraft in soil in ALE simulation.....	67
5.15. SPH simulation of rotorcraft in soil.....	68
5.16. Graph of acceleration vs. time for rotorcraft in soil in SPH simulation.	69
5.17. Airplane used in experiment with dummy [35].....	69
5.18. Deformation of airplane.....	70
5.19 Lagrangian simulation of airplane in soil.	71
5.20. Graph of acceleration vs. time for airplane in soil in Lagrangian simulation.....	71
5.21. ALE simulation of airplane in soil.....	72
5.22. Graph of acceleration vs. time for airplane in soil in ALE simulation.	73
5.23 SPH simulation of airplane in soil.	74
5.24. Graph of acceleration vs. time for airplane in soil in SPH simulation.	74

LIST OF FIGURES (continued)

Figure	Page
5.25. Deformation of airplane with respect to von Mises stress.....	75
5.26 Lagrangian simulation of airplane in water.	75
5.27 Graph of acceleration vs. time for airplane in water in Lagrangian simulation.....	76
5.28 ALE simulation of airplane in water.....	77
5.29. Graph of acceleration vs. time for aircraft in water in ALE simulation.	77
5.30. SPH simulation of aircraft in water.	78
5.31. Graph of acceleration vs. time for aircraft in water in SPH simulation.....	79
6.1. Graph of acceleration vs. time for rigid ball impact on water comparing Lagrangian, ALE, and SPH approaches to experiment.	80
6.2. Graph of displacement vs. time for ball impact on water in flask comparing Lagrangian, ALE, and SPH approaches to experiment.	81
6.3 Graphs of penetrometer on water surface in Lagrangian, ALE, and SPH simulations.....	82
6.4. Graph of acceleration vs. time for soil test comparing Lagrangian, ALE, and SPH approaches to experiment.	83
6.5. Graph of rotorcraft impact on water comparing Lagrangian, ALE, and SPH approaches to experiment.	84
6.6. Graph of acceleration vs. time for rotorcraft impact on soil comparing Lagrangian, ALE, and SPH formulations.	85
6.7. Graph of acceleration vs. time for airplane impact on soil comparing Lagrangian, ALE, and SPH formulations.	86
6.8. Graph of acceleration vs. time for aircraft impact on water comparing Lagrangian, ALE, and SPH formulations.	88
6.9. Deformation of rotorcraft in water and soil.	89
7.1. Stress tensors for improving structure.	91

LIST OF ABBREVIATIONS

ALE	Arbitrary Lagrangian-Eulerian
AMM	ALE Multi-Material
ARA	Applied Research Associates
ATD	Anthropomorphic Test Devices
CLE	Coupled Lagrangian-Eulerian
DOF	Degrees of Freedom
EOS	Equation of State
FAA	Federal Aviation Administration
FAR	Federal Aviation Regulation
FDM	Finite Difference Method
FEA	Finite Element Analysis
FEM	Finite Element Method
FVM	Finite Volume Method
FSI	Fluid-Structure Interaction
GAC	German Aerospace Center
IDRF	Impact Dynamics Research Facility
MKS	Metre Kilogram Second
NASA	National Aeronautics and Space Administration
NTSB	National Transportation Safety Board
SPH	Smoothed Particle Hydrodynamics
SAE	Society of Automobile Engineering
WSU	Wichita State University

CHAPTER 1

INTRODUCTION

1.1 Background

According to FAA reports, 60% of crash impacts are not survivable. Of those, 55% of the fatalities are due to impact on the surface of water, and the other 5% are due to impact with primarily the ground, rocks, mountains, and other surfaces. It is necessary for an aircraft/rotorcraft to be certified. These airframes must meet a required list of regulations, standards, advisory circulars, and military specifications. The U.S. Department of Transportation National Transportation Safety Board (NTSB) along with the Federal Aviation Administration (FAA) has provided design guidelines to meet airworthiness and crashworthiness models. These regulations deal with airworthiness design elements involving payload, take off, tail models, and aerodynamics. The three factors mainly considered in any crashworthiness testing are protection of the airframe structure with respect to occupant safety, minimization of the crash, and safety against the potential threat of fire and rapid evacuation of the airplane occupants. The objective of these regulations is to maximize passenger safety. Regulations and certifications are not economical. On the other hand, computational techniques, which can be utilized to carry out non-destructive testing in a crash analysis, are economical. Modeling water and soft soil material properties is complicated. Due to the complexity and nature of soft surfaces, these materials exhibit nonlinear characteristics.

1.1.1 Review of Airplane Accidents

Accidents that occurred between 1943 until the present have been summarized from the aviation database and are shown in Table 1.1 [1].

TABLE 1.1

NUMBER OF INCIDENTS BETWEEN 1943 AND PRESENT
RESULTING FROM VARIOUS FACTORS [1, 2]

Accidents	12,199
Criminal Occurrences (excluding hijackings)	496
Hijackings	1,037
Incidents	187
Other Occurrences	700
Unknown Occurrences	561
Total	15,177

Various accident reports illustrating scenarios from 1959 to 2006 [3, 4, 5, 6, 7] are listed in Tables 1.2 and 1.3. Johnson as well as the Society of Automotive Engineers [5, 8] reviewed the data of various crash investigations from 156 ground/water accidents. As shown in Table 1.2, the number of land impacts was 142, and the number of water impacts was 14. The number of on-board occupants totaled 12,648, and the number of fatalities from accidents on land was 3,573, and the number of fatalities from accidents on water was 224. In the 224 fatalities involving a water impact, most were the result of drowning. Serious injuries that occurred during a land impact totaled 1,046 and those that occurred during a water impact totaled 80.

TABLE 1.2

ACCIDENTS ON WATER AND LAND REPORTED BY FAA FOR 2006 [5]

	Land Impact	Water Impact	Total
Accidents	142 (91%)	14	156
On-Board Occupants	12,648 (92%)	1,097	13,745
Fatalities	3,573 (94%)	224 (218 by drowning)	3,797
Serious Injuries	1,046	80 (at least)	1,126

Table 1.3 shows a summary of accidents on water during various time periods: 1959–69, 1970–79, 1980–89, 1990–99, and 2000–06. These statistics show that the greatest percentage of fatalities (56%) occurred during 1970–79, and after that, there was a dramatic decrease in fatalities. This was due to the introduction of FAA regulations, which improved the structural integrity of airframes and hence decreased the number of fatalities in crash incidents.

TABLE 1.3

WATER-IMPACT ACCIDENTS FROM 1959 TO 2006 [5, 8]

Period of Time	Accidents	On-Board Occupants	Fatalities	Percentage of Fatalities
1959–1969	9	786	55	7
1970–1979	5	311	174	56
1980–1989	9	1,343	36	3
1990–1999	6	989	192	19
2000–2006	3	408	173	42

Table 1.4 shows FAA-specified speeds and angles during various types of accidents. In controlled ditching [9, 10], the forward speed is below 10 m/sec and the vertical speed is below 3 m/sec, with the pitch angle varying between 0° and 5°. In a vertical descent with limited control, the forward and vertical speeds are between 0 and 35 m/sec and up to 8 m/sec, respectively.

TABLE 1.4

DATA CHARACTERIZING CONTROLLED DITCHING, VERTICAL DESCENT WITH LIMITED CONTROL, AND FLY-IN IMPACT [11]

Accident Categories	Forward Speed	Vertical Speed	Pitch Angle	Roll and Yaw Attitude
Controlled Ditching	Below 10 m/sec	Below 3 m/sec	0°–5° nose up	Level roll attitude Minimal yaw angle
Vertical Descent with Limited Control	0–35 m/sec	Up to 8 m/sec	±10°	± 20° roll angle Significant yaw angle
Fly-In Impact	Up to 50 m/sec	Usually below 3 m/sec	0°–5° nose down	

1.1.2 Review of Rotorcraft Accidents

A survey conducted in the 1990s [12, 13] showed that 24% of the world's civil helicopter crashes occurred on a water surface. According to a survey by Toso [9, 14] from 1976 and 2004, 12 fatal accidents involving aircraft claimed 18 lives. According to this report, the last accident occurred in 2002 and claimed 11 lives. Since no survey was conducted specifically on rotorcraft, less data was available for review. Most of the accidents involved defense-based machinery, so that data was not made available to the public.

As shown in Table 1.5, the location and percentage of rotorcraft accidents from 1980 to 1985 on various terrain were as follows [15]: 34.7% on flat terrain, 5.8% on water, 32.2% on rolling terrain, 7.4% in the desert, and 19.8% in the mountains. The number of rotorcraft impacts on various surface areas follows: 33 (13%) on a prepared surface, 160 (63%) on sod, 38 (15%) on a soggy surface, 16 (6.3%) on snow, 3 (1.2%) on ice, and 4 (1.6%) on water, as shown in Table 1.6.

TABLE 1.5

ROTORCRAFT LANDINGS ON DIFFERENT TERRAIN
AND PERCENTAGE OF OCCURRENCE FROM 1980 TO 1985 [15]

Terrain	Number of Rotorcraft	Percent
Flat	84	34.7
Water	14	5.8
Rolling	78	32.2
Desert	18	7.4
Mountain	48	19.8
Total	242	99.9

TABLE 1.6
 ROTORCRAFT LANDINGS ON SOFT SURFACES
 AND PERCENTAGE OF OCCURRENCE FROM 1980 TO 1985 [15]

Surface	Number of Rotorcraft	Percent
Prepared	33	13
Sod	160	63
Soggy	38	15
Ice	3	1.2
Snow	16	6.3
Water	4	1.6

1.2 Aircraft Ditching Certification

Different types of landing approaches are mentioned in the pilot training manuals. These include normal, crosswind, turbulent air, short-field, soft-field, power-off, emergency, faulty, hydroplaning, and landing. In emergency situations, aircraft are designed to land on water and soil, including soft landings, hard landings, and emergency landings with hydroplaning scenarios. These landings are classified according to the pilot's control as either planned or unplanned.

Ditching takes place under an emergency/forced landing and hydroplaning. In a "planned" landing, the water and soft soil-medium conditions are taken into consideration. With these types of landing, there might be a decrease in the number injuries and therefore possibly less casualties. When the impact is "unplanned," the aircraft occupants and crew are not aware of the imminent crash. A high-velocity impact with loads may cause more damage and subsequently result in a higher probability of injury, even severe or fatal. When setting down an aircraft on land, wind direction and speed must be considered, as shown in Figure 1.1.

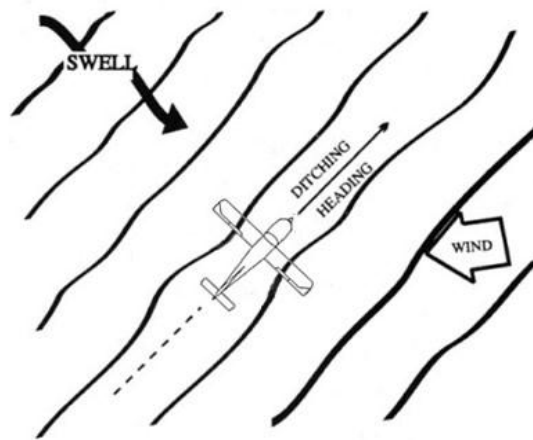


Figure 1.1. Landing of aircraft on water surface [16].

1.2.1 Airplane Ditching Regulations

Ditching has been emphasized more in certification contexts. Both planned and unplanned impacts on water are considered in an investigation to certify an aircraft/ rotorcraft for impact. The major ditching requirements for a large transport vehicle are given under FAR Part 25 [17] in the following sections:

§25.561 Emergency Landing Conditions

§25.801 Ditching

§25.803 Emergency Evacuation

§25.807 Emergency Exits

§25.1411 Safety Equipment

§25.1415 Ditching Equipment

Other sections of the Federal Aviation Regulations, Parts 121 and 125 [18, 19, 20, 21], must also be considered for emergency evacuation. They include requirements relative to equipment and evacuation procedures for the crew and pilot:

§121.291 Demonstration of Emergency Evacuation Procedures

§121.339 Emergency Equipment for Extended Over-Water Operations

§121.340 Emergency Floatation Means

§121.417 Crewmember Emergency Training

§125.209 Emergency Equipment: Extended Overwater Operations

From a structural point of view, aircraft are designed to maintain crash g-values within human tolerances, and devices to absorb these forces need to be incorporated into the aircraft structure. In the future, seats and seat belt certification will be considered important in the certification process. If belts do not retract or extend properly, then there might be fatal accidents. Doors and windows must be designed for safety and able to withstand maximum pressure loads. In the event of an impact on water, there must be protection to keep the water from rushing inside the aircraft, especially the cabin. Doors and windows should also be protective and not jam during escape.

1.2.2 Rotorcraft Ditching Regulations

The manufacturers of rotorcraft are required to authenticate ditching during testing to fulfill the requirements of the FAA. These are provided with FAR 29 [22, 23] relative to transport rotorcraft. The following sections of FAR 29 deal with rotorcraft ditching:

§29.801 Ditching

§29.807 Passenger Emergency Exits

§29.1411 Safety Equipment

§29.1415 Ditching Equipment

FAR 25 and FAR 29 [22, 23] provide a brief description of the overall review that a designer must consider when building an aircraft or rotorcraft. This includes structural integrity, mechanisms during ditching phenomena, and floating characteristics.

1.3 Motivation for this Study

In the crash incidents examined, 60% of them were not survivable [24]. Of those crashes, 55% of the fatalities were due to impact on a water surface, and the other 5% occurred mainly on the ground, rocks, mountains, and other surfaces. This percentage proves that even impacts on water and soil are not survivable instances. In the past, due to inadequate development in airworthiness and crashworthiness, more crashes occurred. These accidents took place on water and land surfaces, resulting in more damage to the aircraft structures and thus causing fatal injuries to the on-board passengers. To decrease the severity of injury, some regulations and certification procedures were developed by the FAA, which have helped aircraft and airframes sustain structural deformation when subjected to water (ditching). Regulations and certification of aircraft are not economical but they are required according to the rules of the FAA. Many aircraft companies want to satisfy these FAA standards without wasting money and materials. Computational methods are meant for carrying out non-destructive testing in crash analysis. By applying these computational methods to certify aircraft, the cost would be reduced because fewer materials would be wasted.

Previous studies conducted in this field focused more on rigid surfaces, but by implementing a nonlinear finite element method (FEM), material such as water and soil can be used in these impact tests. If a body undergoes impact on a rigid floor, the load concentration is toward the surface of the frame. A larger load on the surface may lead to larger deformations. When no indentation is made on the ground as the result of an impact, the ground is considered a rigid floor when deformation of the frame occurs. When considering a soft surface, the load is not distributed uniformly. Due to the nature of the soft surface, waves or craters are formed on the impacting surface. When impact occurs on a soft surface, the load is equally distributed

across the entire body; therefore, energy is absorbed equally throughout the frame, and there will be less damage compared to that which would occur on of a rigid surface. Figure 1.2 shows the difference in energy absorption between a rigid impact (a) and a soft surface impact involving nonlinear materials (b). Energy absorption on the rigid surface is calculated because of actual structural deformation sustained by the frame, but energy absorption on the soft surface is calculated as both structural deformation and soft-surface deformation.

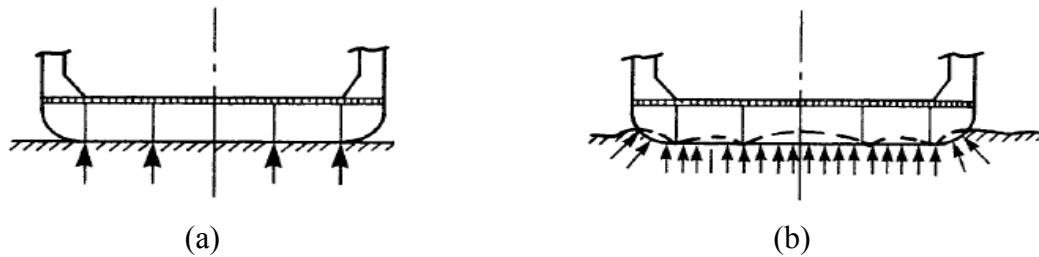


Figure 1.2. Energy absorption in rigid surface impact (a) and soft surface impact (b) [15].

Modeling water and soft soil material properties is more complicated than modeling other engineering materials. Due to the complexity and nature of soft surfaces, these materials exhibit nonlinearly material characteristics. Many analyses have been conducted by researchers on water impact, and these can be used for validating material properties for fluid-structure interaction (FSI). In the case of soil, material properties can be obtained by using a tri-axial compression test, such as that conducted at Applied Research Associates, Inc. (ARA). These properties can be used extensively for soil-impact analysis. Soil properties and validation of this material property will be explained in detail in Chapter 4, and the application will be discussed in Chapter 5.

Full-scale dynamic certification testing of aircraft or rotorcraft is quite an expensive and time-consuming process. One feasible solution to solving this problem is by implementing finite element analysis (FEA). A finite element method (FEM) is a mathematical approach that can approximately solve a partial differential equation [25], and its practical application is known as FEA. Earlier studies conducted on FEA modeling have been limited to impact on rigid mediums

like concrete or hard ground. Advancements in FEA have resulted in the development of a nonlinear finite element code, which is intended to solve a complex problem, and a detailed study is discussed in Chapters 3 and 4. The present research emphasizes material properties and structural deformation with respect to this nonlinear finite element analysis. Nonlinearity in material can be observed in mediums such as water and soft soil. Another important nonlinear parameter is based on the size and shape of the object, or geometrical nonlinearity. A limited study was done on water and soft soil with respect to crashworthiness and material properties [26, 27].

During the certification process, FAR 25 and FAR 29 must be carried out by the Federal Aviation Administration [28, 29]. In these regulations, water impacts are considered, so research is carried out on this medium. Because of this material's nonlinear nature, a limited study has been proposed.

As previously mentioned, nonlinear problems are mainly due to material properties and a complex model. These problems are considered engineering problems, which are basically solved using mathematical models and, in turn, are solved using differential equations and a set of conditions, such as initial and boundary conditions. Fundamental basic formulas are used to solve these differential equations. The governing equations from mathematical models are mainly represented as conservation of mass, energy, and forces. These mathematical models are generally used for finding exact solutions to simple problems. However, practical engineering problems are complex: rigid bodies impacting water, rigid bodies impacting soft soil, aircraft being impacted at high speeds. These analyses are not easy to solve with an ordinary governing differential equation.

Advancements in the computer software and hardware technology allow these complex problems to be analyzed using computer-aided numerical methods.. These FEA techniques with computer-aided methods can solve these problems and be used for dynamic testing of aircraft.

1.4 Literature Review

Pentecote and Kindervater, from the German Aerospace Center (GAC) [23], conducted an experiment to validate water impact using the explicit finite element code PAM-CRASH. The analyses were based on local/global methodologies using PAM-CRASH with a combination of a finite element code and a hybrid code, or DRI-KRASH. The main purpose of this research was to derive a methodology to assess an entire aircraft's structural integrity. Initially, the water medium has to be validated using the FEA, that involves hydrodynamics, and viscous nature of water. The main guideline considered in the selection of a fluid material is viscosity. In this impact analysis, a PAM-CRASH isotropic plastic hydrodynamic material model governed by an equation of state (EOS) linear polynomial was used to exhibit the nature of this material. Viscosity was neglected, and the simulation was carried out only during the initial milliseconds. Figure 1.3 illustrates the experiment and FEM representation. Figure 1.3 (a) illustrates ripples in the form of contours on the surface of the water, which represents the splash formation. Figure 1.3 (b) shows a graphical representation of results from the experiment and the FEM analysis conducted by Pentecote and Kindervater, acceleration values for the experiment and FEM as 91 G and experimental is 69 G. The experimental graphs were passed through 600 Hz SAE [7] filter, and FEM WAS passed through a 1000 Hz filter.

The next phase concentrated on a non-rigid fuselage model (90 cm long and 30 cm in diameter) with an impact velocity around 1,000 cm/sec and a pitch angle of 1.3° . A half model consisting of 2,192 shell elements for the fuselage was considered for the FEM analysis with

boundary conditions. Results from PAM-CRASH were used as input in DRI-KRASH, as shown in Figure 1.3 (c).

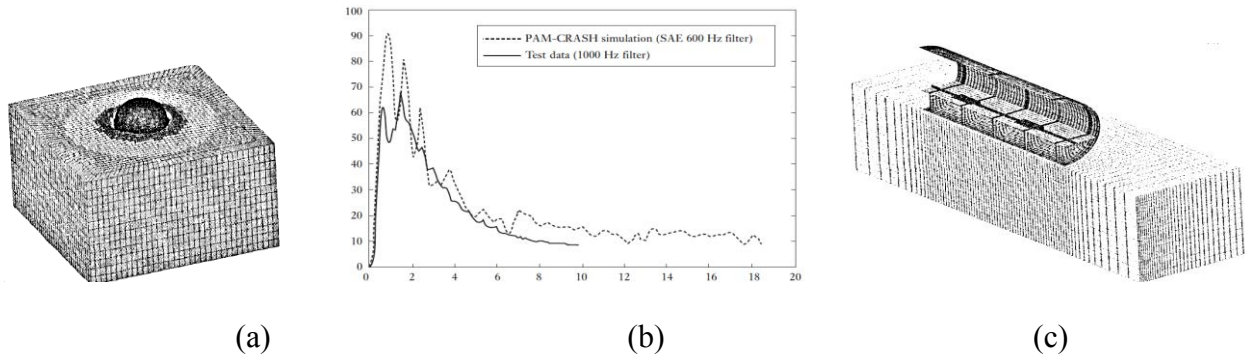


Figure 1.3. FEM representation: (a) ball test experiment, (b) graphical representation of ball test experiment, and (c) quarter model of fuselage after impact in water pit [23].

Jackson and Fuchs, from NASA Langley Research Center [31], conducted a simulation of a multi-terrain impact on water, which improves the prediction of rotorcraft crashworthiness in a water medium. Their analyses were based on two vertical drop tests using a fuselage. The first case test was conducted with a composite fuselage 5 feet in diameter on a water surface, and the second cast test involved honeycomb energy absorbers on the fuselage. To validate water properties in these impact tests, a drop test with a penetrometer was conducted. The experimental test setup is shown in Figure 1.4. Their research was divided in two types: experimental and FEM. In the experimental phase, the composite fuselage was subjected to impacting water from a height of 70 feet from vertical drop towers; therefore, the velocity of the fall was 27 ft/sec. Another experiment was conducted with energy absorbers. Following the experimental work, the FEM model was validated with the experimental data. The FEM used in this research was based on the arbitrary Lagrangian-Eulerian (ALE) and smoothed particle hydrodynamics (SPH) methods with a varying rolling angle.



Figure 1.4. Test setup with penetrator [28].

In this validation, a mesh study was also carried out by varying the size of the mesh. Results obtained with the SPH method was validated with experimental results. An experimental study, conducted at the Langley Research Center, involved a penetrator dropped freely at a velocity of 7.62 m/sec. The diameter of the penetrator was 0.664 m, and the diameter of the water tank was 1.81 m. The results obtained from this test were passed through 1,000 Hz loss-pass filters with SAE J211 requirements, as shown in Figure 1.5. Then a mesh study was conducted using mesh variation for validating water with SPH. It was concluded that the SPH method results in a higher mesh density and is better than the ALE method.

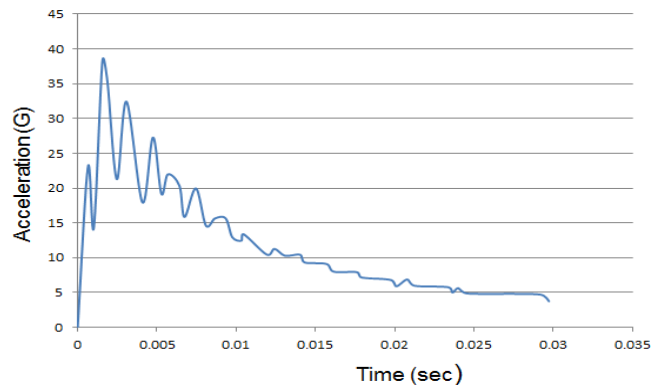


Figure 1.5 Graphical FEM representation of penetrator test [31].

Randhawa [27] studied hydrodynamic impact on the surface of water. An experiment using two balls with different masses was conducted by Randhawa and Lankarani [32] at Wichita State University (WSU). These balls were impacted on water, and the experiment was

carried out using a high-speed camera, which captured displacement at each millisecond. Specifications of the apparatus and experimental setup, which included a Kodak Ektapro motion analyzer, are listed in Table 1.7.

TABLE 1.7
EXPERIMENTAL APPARATUS [32]

Glass Flask	Radius 8.3 cm, height 25.4 cm
Water Level	15.24 cm
Drop Height of Balls	10.16 cm
Impact Velocity	141.18 cm/sec
Ball Material	Rubber plastic
Ball-I Radius	2.156 cm
Ball-I Mass	13.7e-03 kg
Ball-II Radius	1.3309
Ball-II Mass	40.8e-03 kg
High-Speed Camera	Kodak EKTAPRO Motion Analyzer

Figure 1.6 (a) and (b) shows a pictorial representation of the apparatus used to carry out this hydrodynamic impact experiment at a velocity of 141.18 cm/sec. The two balls were made to impact water in a glass flask, and the impact analysis was conducted six times with two balls of two different masses and three iterations for each ball. The analyses with ball-II were successful, and data was validated with the FEM. The graph in Figure 1.6 (c) shows how displacement varies with time steps.

In this analysis, Lagrangian and ALE methods were compared. The ALE method showed promising results. Therefore, the ALE simulation was used considered for the water impact analysis involving rotorcraft FEA Model. Results from the rotorcraft experiment were used as input for the MADYMO code. It was concluded that the ALE results obtained from the water impact were better than results obtained using the Lagrangian method.

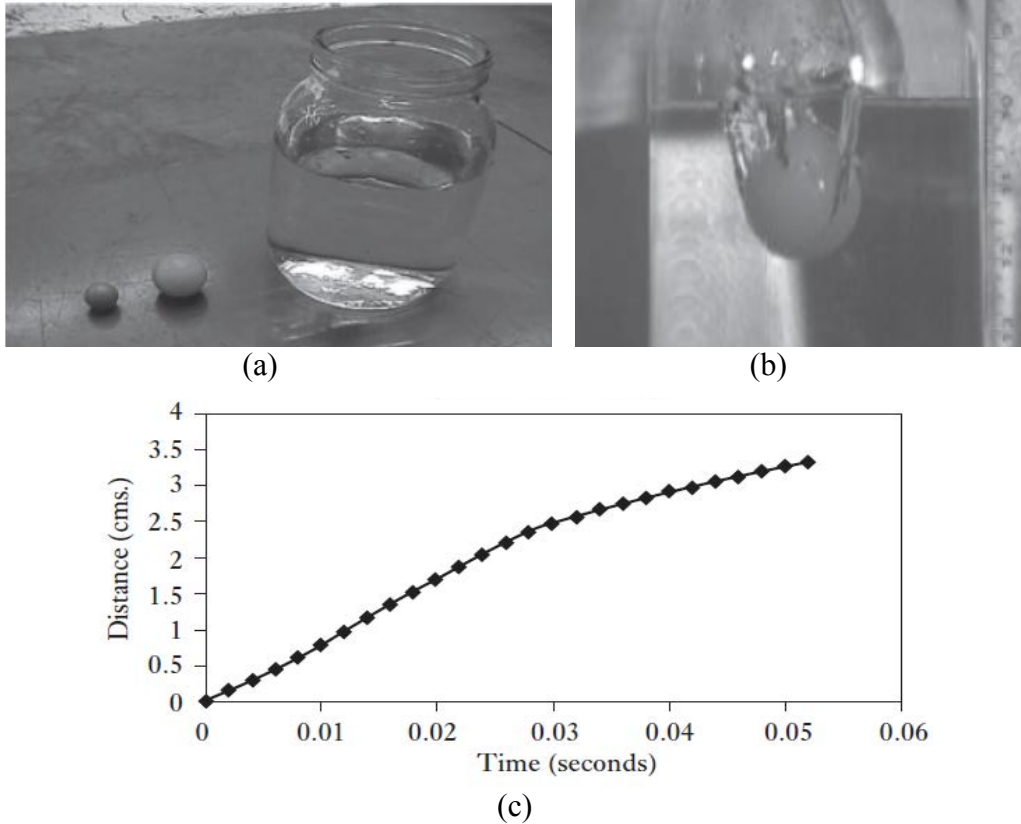


Figure 1.6. Apparatus used in hydrodynamic impact experiment: (a) ball and flask of water, (b) ball impacting water in flask, and (c) graphical FEM representation of ball and flask experiment [32].

Ramalingam and Lankarani [24], investigated aircraft crashworthiness during an impact on soil. This study emphasized the development of a soil model that could be used for simulating a soil impact with huge structures such as aircraft or rotorcraft. Validation of the soil impact was carried out using sphere and cone impactors in a drop test; the validating parameter was based on penetration of the impactor. Later on, aircraft with a predetermined velocity and angle of impact replaced these impactors. NASA has conducted this actual test, and acceleration data was obtained from the center of mass of the airplane model. This study was conducted using nonlinear finite element codes.

Fasanella et al. [19] conducted testing for a geometric boilerplate of the Orion capsule on a soft-soil landing. Applied Research Associates, Inc. [13, 3] determined the soil properties.

ARA provided ten material properties that were used by NASA for the soil landing, including hard-clay at the Cuddeback dry lake bed near California, Florida sand, etc. The modeling of MAT 5 was robust, relatively hard to construct, and pressure dependent. Due to the shear failure surface, this soil has more deviatoric stresses and material flow. Soft soils are confined to prevent flowing under gravitational loads due to the pressure gradient with soil depth.

The two different sands were clean and mixed with clay, which are present in NASA Langley [13] soils. Moisture is another important factor. The strength test was carried out using a tri-axial compression test. Figure 1.7 shows how the experiments were set up for analyzing and how the properties were extracted.

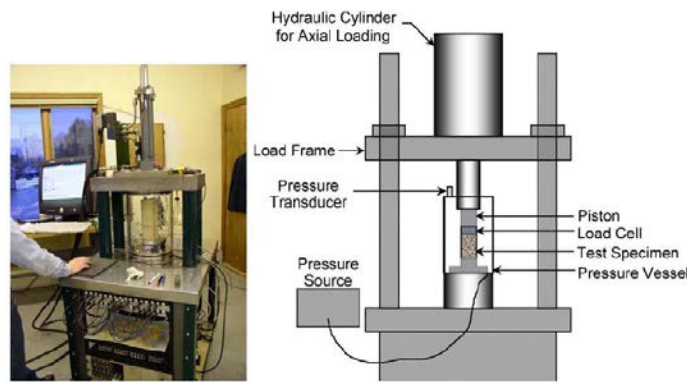


Figure 1.7 Test setup of tri-axial compression test on soil [19].

Fasanella et al. [19] validated soil for the boilerplate impact on soil pits. During impact analysis, boilerplates were subjected to impact on the surface of the soil using a vertical drop test. In this analysis, soil properties were validated, and a penetrometer test was used to determine the properties. The test site for the soil test is shown in Figure 1.8. Five tests were conducted randomly in that analysis, and tests 4 and 5 resulted in no error, as shown in the graph in Figure 1.9. Later on, these soil properties were used to do an analysis with a boilerplate in a space capsule.

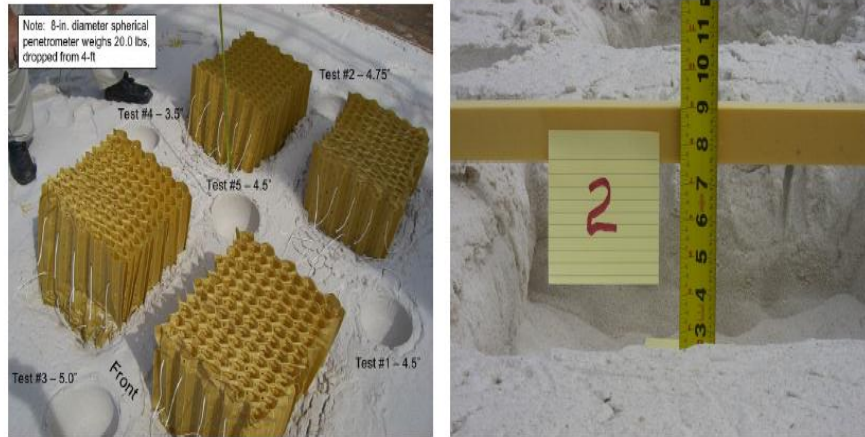


Figure 1.8. Test site for soil test [19].

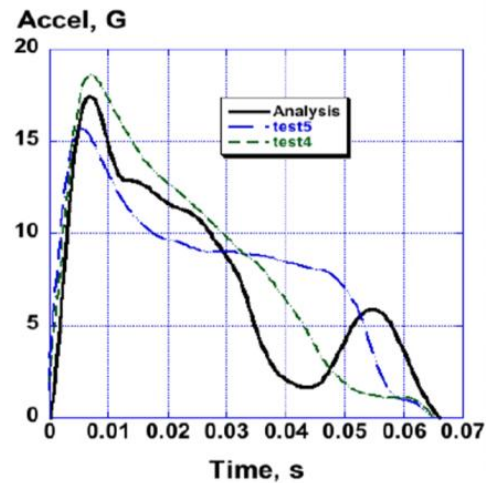


Figure 1.9. Graphical representation of test data in acceleration [19].

Vaughan and Hayduk [18] investigated the impact of a single-engine airplane specimen on a soil surface. In this test, yaw, roll, and pitch played important roles in minimizing impact forces on the structure. These pitch, yaw and roll angles are represented as θ , ψ , and Φ , respectively, as shown in Figure 1.10. This was a pullback test, where the aircraft at a certain velocity was pulled back. The angles were adjusted as shown in Figure 1.10.

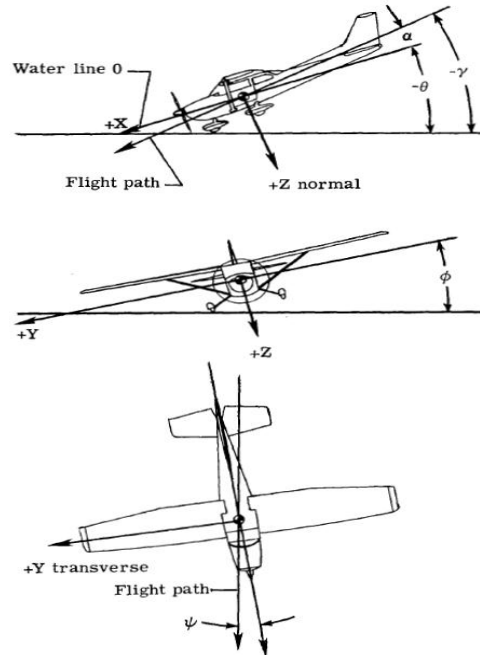


Figure 1.10. Angles in aircraft landing [35].

In this test, the specimen was subjected to a crash with a negative pitch angle as it impacted the soil. The velocity of the specimen was 25 m/sec. Angles maintained during the test were as follows: flight path angle -32° , pitch angle -34.5° , yaw angle 2° , and roll angle -1.5° . When the aircraft came in contact with the soil, the fuselage and cabin underwent large deformations, and structural integration was observed. Initially the engine penetrated the soil and then the cabin. In this test, anthropomorphic test devices (ATDs) were placed inside the aircraft to determine the injury criteria. In this research, acceleration on the floor of the aircraft was nominally 20 g to 25 g, as stated in the research by Ramalingam [26].

In the experimental phase of one study conducted by Richards and Kelley, Simula Technologies, Inc., and the U.S. Army [36], a helicopter was dropped from a height of 9 feet. The velocity was calculated to be around 24 ft/sec. In this test, the fuselage impacted the surface of water. The weight of the testing fuselage skin was 1,450 pounds. With the help of a crane, the test article was suspended over a water pit, as shown in Figures 1.11 and 1.12.

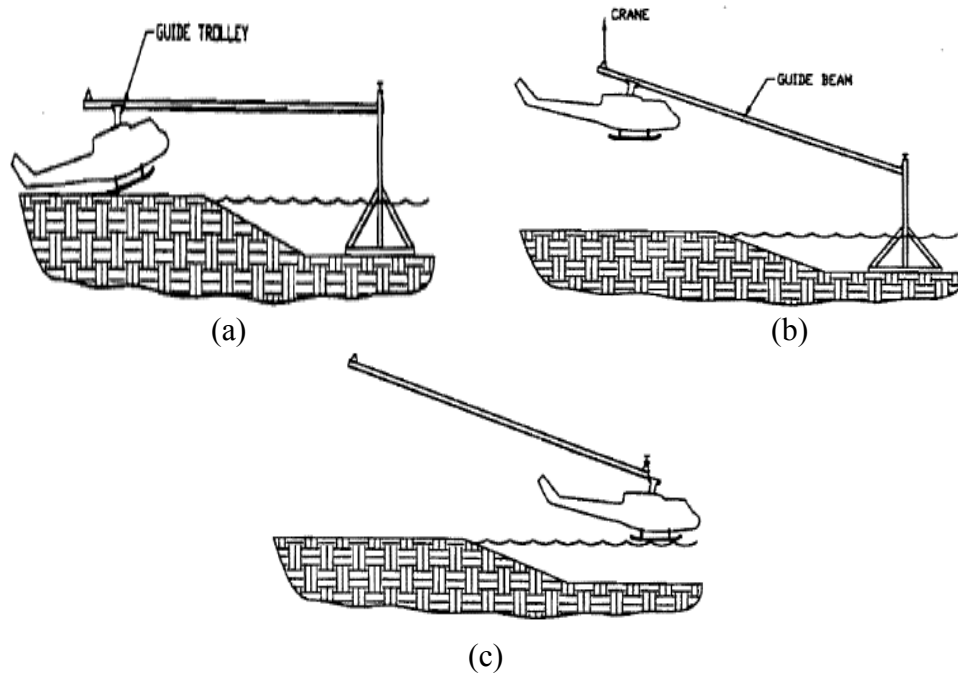


Figure 1.11. Test setup of rotorcraft: (a) initially, (b) raised to a certain height, and (c) subjected to impact [36].

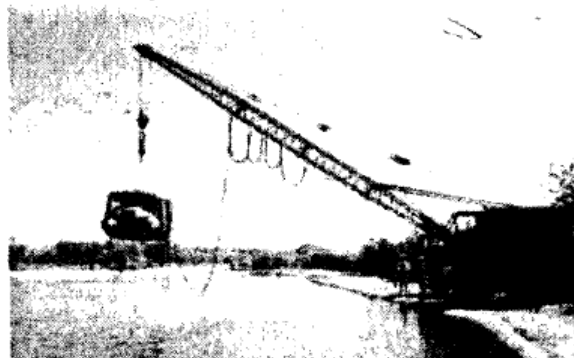


Figure 1.12 Test setup for vertical drop test [36].

The impact pulses were extracted with the help of transducers and an accelerometer. Accelerometer data, shown in Figure 1.13, was obtained using a 10,000 Hz VXI-based data acquisition system and digitally filtered at 300 Hz. The maximum peak was 69 g, and the minimum peak was 27.9 g, as shown in Figure 1.13 (b). From Figure 1.14, it can be seen that damage occurred on the bottom of the fuselage. Structural damage during impact included a

cracked small Plexiglas bubble and a bulged panel, as shown in Figure 1.14 (a) and (b), respectively.

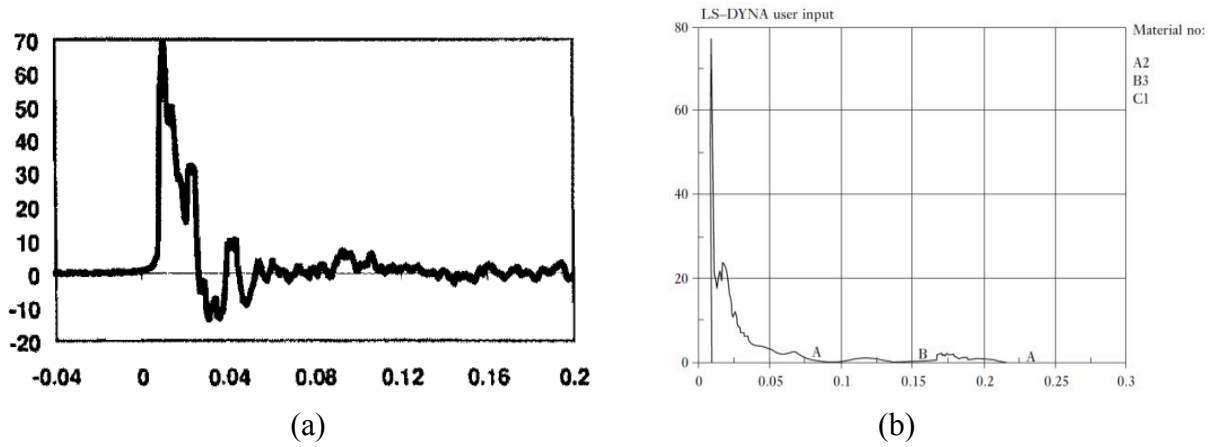


Figure 1.13. Accelerometer data: (a) experimental results of helicopter impacting water [36], (b) ALE results obtained by Randhawa experiment using LS-DYNA [32].

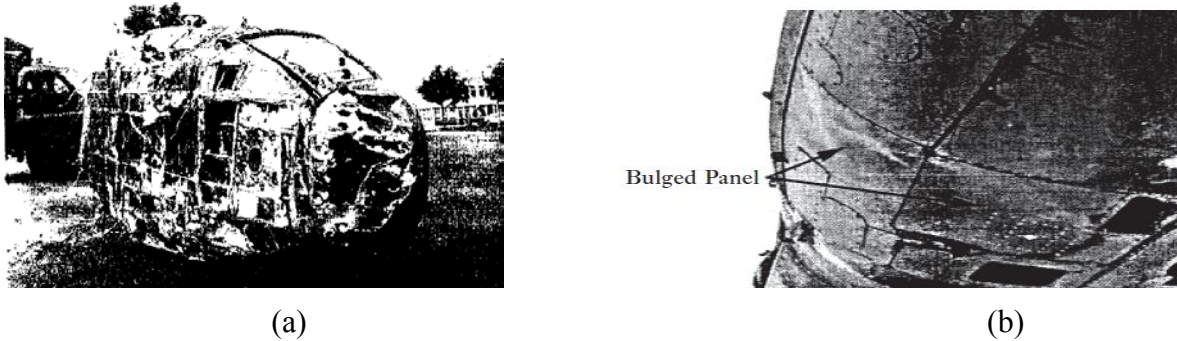


Figure 1.14. Structural damage: (a) bottom of helicopter frame, and (b) bulged panel on helicopter surface [36].

Randhawa [27] used the ALE method along with LS-DYNA. Material properties assumed for the analysis were MAT_ELASTIC_FULID. In this analysis, water was validated using an experiment conducted in a water flask, which was discussed previously. Tri-mesh was considered for the helicopter, and quad mesh was considered for the water and air domains. Dimensions of the water pool were 960x960x240 cm, the mesh seeding was 20x20x15, and the elements used were solid elements.

Other individual techniques for modeling either water or soil impact are found in the literature, but none have compared the different techniques or compared the water and soil impacts.

1.5 Objective of Thesis

The main objective of this thesis was to carry out different types of crash-testing analysis with respect to water and soft soil, and applications on three different airframes. Within the framework of this thesis, numerical methodologies were developed and evaluated on the airframe during impact on water and soft-soil mediums. Initial material modeling was carried out on a simple ball test and then a penetrometer was used. Different numerical methodologies, such as Lagrangian, arbitrary Lagrangian and Eulerian, and smoothed particle hydrodynamics, were used in all experiments and the results compared. A challenging aspect of this study was implementing different material properties into different domains such as water and soft soil, and then applying them to determine aircraft crashworthiness. To conclude the thesis, water and soil results are compared, results are summarized, and the potential attributes of each method are discussed.

1.6 Organization of Thesis

Chapter 1 of this thesis describes the statistics of soil and water impact. It also explains crash regulations, research centers, and equipment used, including detailed discussions. Chapter 2 explains the theory behind finite element analysis and a brief description of techniques, such as Lagrangian, ALE, and SPH, and the methodology used in the validation procedure.

Chapters 3 and 4 explain the use of Lagrangian, ALE, and SPH concepts for a simple ball test, sphere test, and penetrometer test conducted by different researchers. First, these material

properties are validated using the Lagrangian method. Then ALE and SPH are implemented to compare the data, and the same process is used to validate soil properties.

In Chapter 5, airplane and rotorcraft crash landing scenarios are presented and experimental data compared. In Chapter 6, the results obtained by various numerical analyses are discussed, and Chapter 7 presents conclusions and future impact study work .

CHAPTER 2

FINITE ELEMENT METHOD AND METHODOLOGY

2.1 Finite Element Method

Generally, all physical phenomena are computed using partial differential equations in the science and engineering domains. These equations, with some irregularities, cannot be solved using classical analysis, so discretized methods are used. These discrete methods are computed using a numerical approach utilizing partial differential equations, and they are solved approximately. This is known as the finite element method (FEM), which is widely used to solve stress analysis, heat transfer and fluid flow, and electromagnetism. By using a computer code, these analyses are solved using high-performance computers. FEM means dividing a complex shape into a number of small finite discrete shapes, which can then be used to solve complex equations. These divided finite shapes are known as elements. The discrete complex model using a node and elements is known as mesh generation, and the collection node and element in the model is known as the mesh. These meshes are usually divided according to shapes of the element.

FEMs are divided into two types of finite element analysis: linear and nonlinear. Linear finite element analysis is used for static and small analyses such as strain, rotation, displacement of small beams, shell and solids, and small changes of temperature that can be observed. Linear analysis is easier to compute and cost effective, and the solutions will be accurate. However, linear analysis has some disadvantages: it cannot solve large-deformation problems, high-performance design, true material behavior, and complex impacts such as those involving water and soft soil. Basically, linear analysis can be used for material properties that obey Hooke's Law (i.e., linear relationship between stress and strain) and small deformations such as plane

stress. Nonlinear analysis is carried out on material properties that cannot obey Hooke's law and depend on a temperature gradient. However, through the application of nonlinear analysis, a full-scale analysis can be carried out.

Nonlinear finite element analysis is basically used for large deformable designs and for complex material properties. This type of analysis is classified according to mathematical models in continuum mechanics and their correlation; it is primarily used in the automobile industry. For example, in crash tests, the prototype model is replaced with a numerical model to carry out full-scale crash testing. This analysis can also be used in manufacturing processes and in the electronic industry with drop tests, etc. It is solved in the following steps: development of a model, formulation of the governing equation, discretization of the equation, solution of the equation, and results.

In nonlinear analysis, some important nonlinearities are due to the material, geometrical, boundary conditions, and displacement boundary conditions. In this research, material and geometric nonlinearity were observed. Nonlinear materials occur as the result of stress-strain, force-displacement, or material properties, which will change according to load or properties and will not always obey Hooke's law. Geometrical nonlinearity is due to strain-displacement with respect to solids, large displacement, large strain, large rotation, etc. Nonlinear finite element analysis techniques are classified according to algorithms of continuum mechanics into two classical methods: Lagrangian and Eulerian. With the use of this method, new methods have been developed: coupled Lagrangian-Eulerian (CLE), arbitrary Lagrangian-Eulerian, and the meshless smoothed particle hydrodynamics.

2.1.1 Lagrangian Technique

The Lagrangian method or technique is widely used in FEM analysis. In this method, nodes are connected to each other with a material medium. These connecting nodes are an imaginary, or integration, point. In this computational process, mesh is attached to material and therefore moves along with it (during compression, expansion, etc.), as shown in Figure 2.1. Mass, momentum, and energy move with the nodes depending on which material deforms with the mesh. The Lagrangian method is used in solid material formulation.

The Lagrangian technique is simple and faster to compute because there are no convection terms, the time for each analysis is less, and irregular geometry can be computed. The disadvantage of this method is movement of the mesh and material with respect to the material. Large deformation results may be inaccurate because remeshing does not occur.

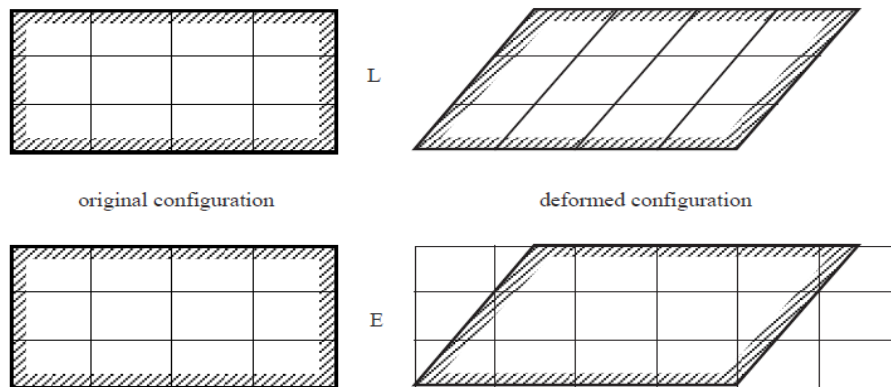


Figure 2.1. Lagrangian mesh (L) and Eulerian mesh (E) and their deformation with respect to mesh and material [37].

2.1.2 Eulerian Technique

The Eulerian technique is widely used in the finite volume method (FVM). The reference mesh moves across a fixed mesh based on deformation, as shown in Figure 2.1. As can be seen later on in Figure 2.4, which provides information about the methodology, the material and mesh are updated as a Lagrangian formulation, and the mesh does not move but the material flows

through it. For this reason, the Lagrangian formulation uses fluid analysis, whereby the mesh will not change during the entire computation process, and large deformations can be solved.

In the Eulerian technique, the domain mesh is fluid, and flow of the material is in the mesh. The principle of hydrodynamics is solved using the multi-material Eulerian method for calculating mass, momentum, and energy flux in the fixed mesh.

2.1.3 Arbitrary Lagrangian-Eulerian Technique

In the ALE formulation, as shown in Figure 2.2, there are two types of mesh. One is the reference mesh (domain mesh or medium), and the other is the material mesh (deformation mesh or mesh used for analysis), as shown in Figure 2.3. In this method, the reference mesh with the material mesh moves with arbitrarily defined conditions such as water, soil, or any substance according to the kind of simulations. In this method, the material and reference meshes are updated with the Lagrangian formulation, and these element history variables are mapped onto the updated mesh.

The main objective of the ALE method is to utilize both Lagrangian and Eulerian formulations according to conditions required for the analysis and result-based simulations. In this formulation, the Lagrangian time steps are known as advection steps. Here, nodes are changed in small fractions according to the material property, as shown in Figure 2.4.

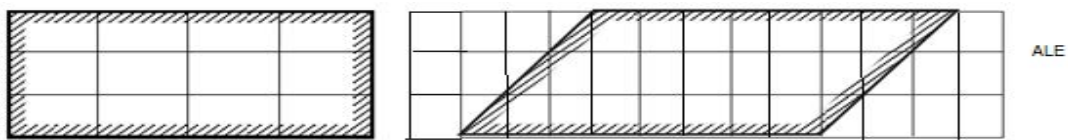


Figure 2.2. Arbitrary Lagrangian-Eulerian (ALE) mesh and its deformation with respect to mesh and material [37].

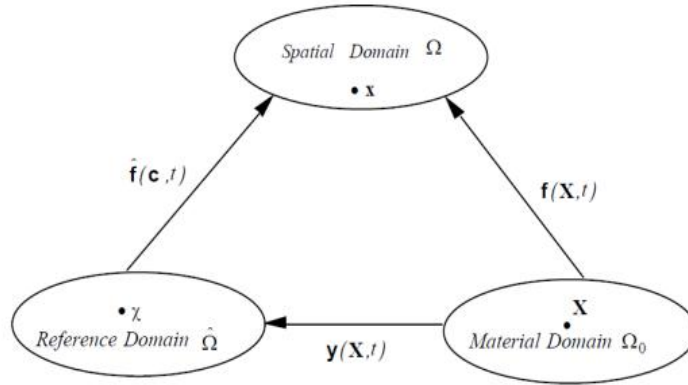


Figure 2.3 ALE block diagram [37].

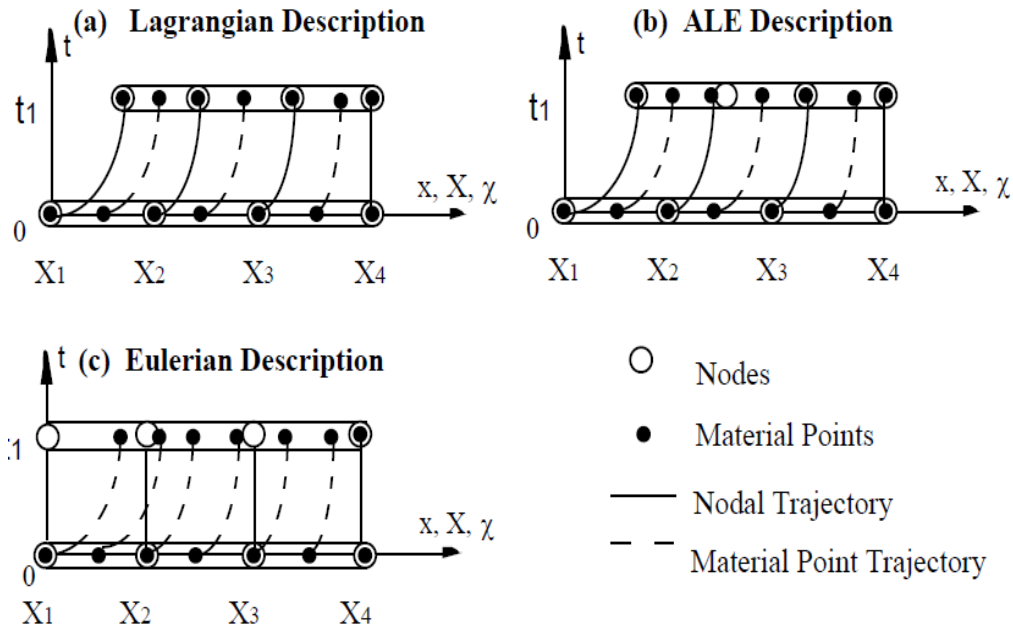


Figure 2.4. Lagrangian, Eulerian, and ALE deformation with respect to nodes, material, nodal trajectory, and material point trajectory [37].

2.1.4 Smoothed Particle Hydrodynamics Technique

In the SPH method, the set of particles has material properties and moves with coordination governing the conservation equation. This method is used to calculate dynamic fluid flows along with deformation. The SPH technique is mesh-free and has a similar formulation to that of the Lagrangian method since the particles are considered to be nodes. The importance of this mesh-free method is due to its adaptive nature and time step and its own

arbitrary distribution of particles. This method is used in representing the problem domain and acts like a computational variable approximation scenario. This method is different from those for the FEM or finite difference method (FDM). The formulations are based on Lagrangian simulation and particles approximation.

In the SPH method, computation is based on a sorting technique. The distance between nodes, or smoothing length, is represented mathematically using a kernel spline or function, as shown in Figure 2.5. If the distance between smoothing lengths is less, then the solution converges without error. Computation time for this analysis is less than any FEM or FVM analysis.

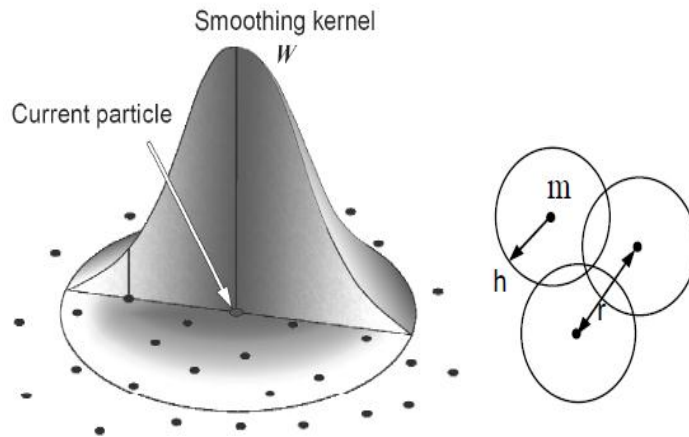


Figure 2.5 Kernel spline or function showing smoothing kernel between nodes (W), distance between nodes (r), diameter of particle (h), and mass (m) [38].

The particle approximation of a function is

$$\prod^h f(x) = \int f(y)W(x-y,h)dy \quad (2.1)$$

where W is the kernel (or smoothing) function.

The kernel function, using θ , is defined as

$$W(x,h) = 1/h(x)^d * \theta(x) \quad (2.2)$$

where d is the space dimensions, h is the smoothing length, which varies in time and space, and $W(x,h)$ should be the centrally peaking function. The most common smoothing kernel function used along with the SPH method is the cubic B-spline, which is defined by choosing θ as

$$\theta(u) = C \times \begin{cases} 1 - \frac{3}{2}u^2 + \frac{3}{4}u^3 & \text{for } |u| \leq 1 \\ \frac{1}{4}(2 - |u|)^3 & \text{for } 1 \leq |u| \leq 2 \\ 0 & \text{for } 2 < |u| \end{cases} \quad (2.3)$$

2.2 Finite Element Methodology

The basic methodology for FEM is shown in Figure 2.6. In this flowchart, the entire test setup is divided into the numerical simulation and the experiments. Numerical solutions are solved using Lagrangian, ALE, and SPH methods. These solutions are compared in the simulation results, and the numerical simulation results are compared with the experimental results. Figure 2.6 also describes the method of validation.

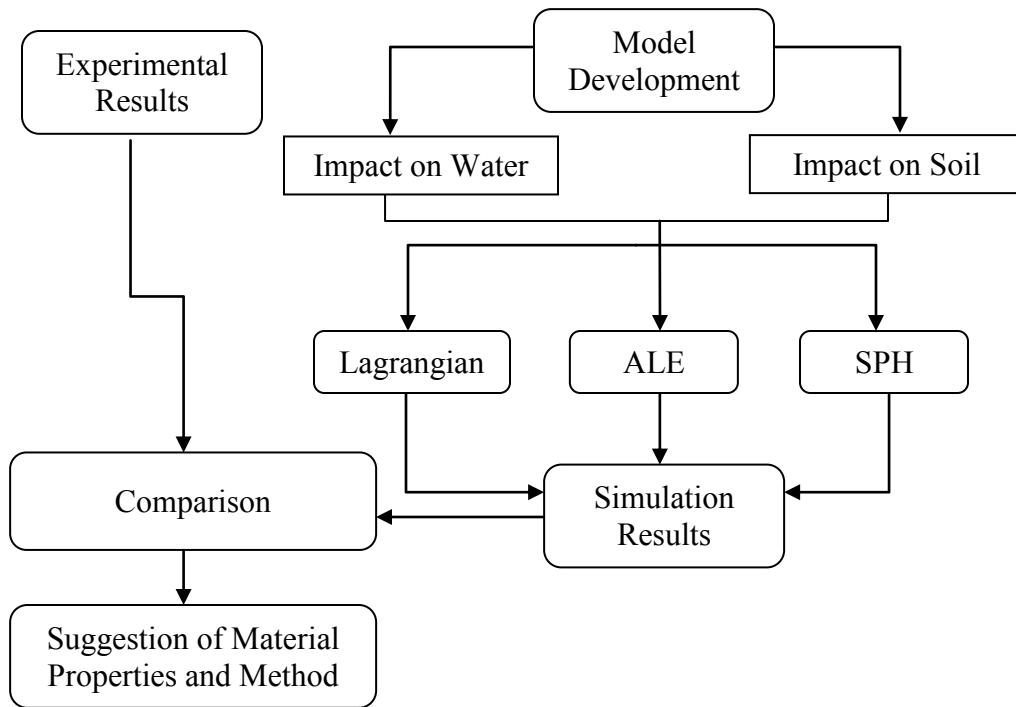


Figure 2.6. FEM methodology chart.

As shown in Figure 2.7, in the beginning of the FEM, the mesh is completed and refined until the solution converges. Mesh refinement is carried out using Lagrangian and ALE methods, while nodes are arranged in a denser manner using the SPH technique. The distance between two nodes and the number of nodes play an important role in SPH analysis. Later, a rigid body is subjected to impact with water and soft soil. If the solution converges, then it is compared with the experimental results. If the solution does not converge, then those material properties must be changed or altered accordingly. If material properties are corrected, then the refinement of the mesh must carry over until the solution converges and correlates with the experimental results. In addition, this solution is compared with ALE and SPH results. Then the FEM is applied to one aircraft and rotorcraft, which are subject to the vertical drop test, IDRf gantry test, and later controlled impact testing.

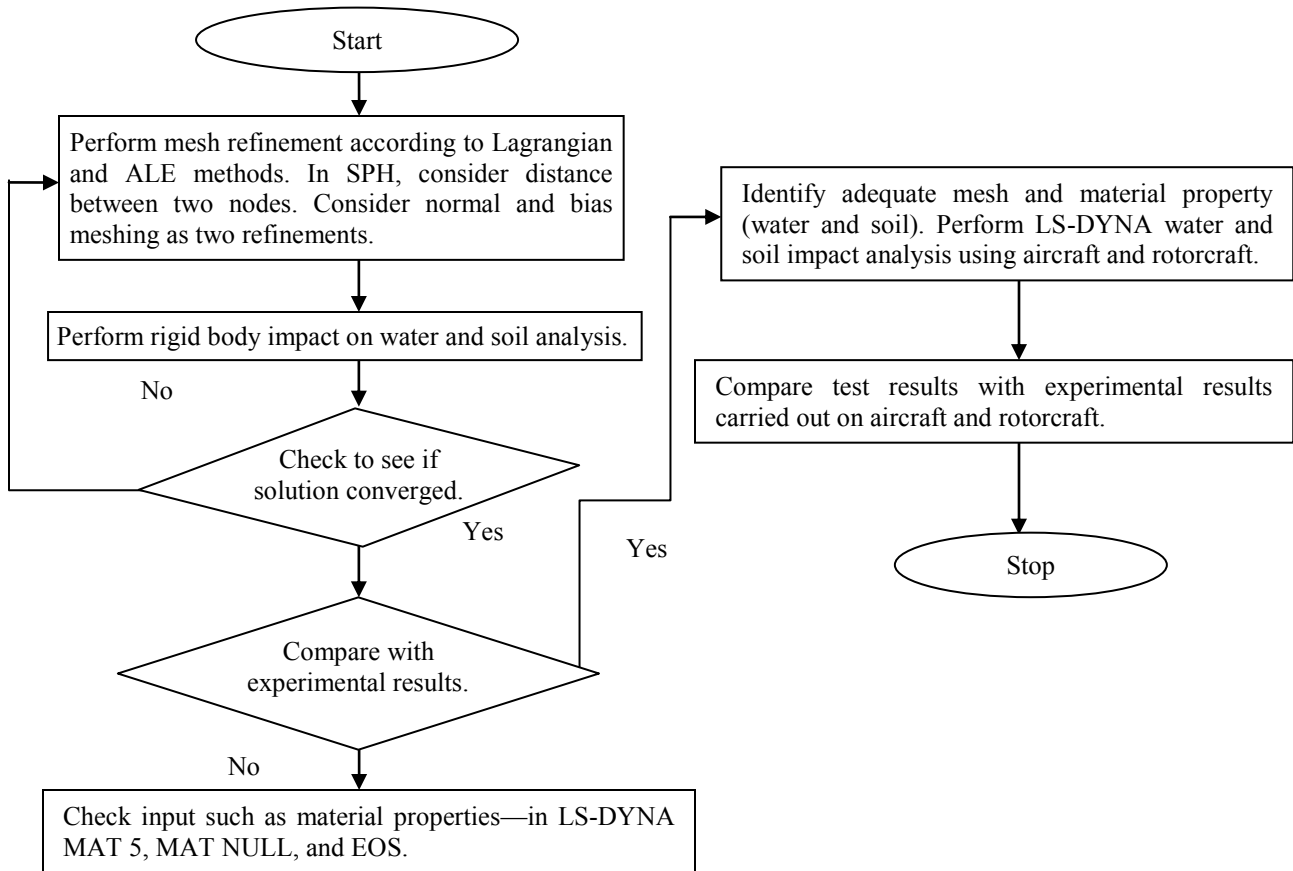


Figure 2.7 Methodology for validation of water and soft-soil impact analyses.

CHAPTER 3

MODEL DEVELOPMENT AND VALIDATION OF IMPACT ON WATER

LS-DYNA uses nonlinear FEM codes for transient dynamic finite element programs. LS-DYNA capabilities include simulating complex models that replicate real-time experiments. The nonlinear FEM code can be implemented to solve complex mathematical problems in engineering domains.

Earlier finite element methods were restricted to structural mechanics, whereas finite volume methods were subjected to fluid mechanics. After the evolution of continuum mechanics, complex problems were simplified in order to solve FEM problems. Using continuum mechanics in FEM codes, FVM problems were made soluble by using ALE and SPH formulations.

In FEM analyses, complex geometries are divided into small elements known as discrete elements. These are classified into shell, solid, beam, rod, and truss elements. In the research by Pentecote and Kindervater [23], a one-dimensional element such as a beam, rod, or mass was used to carry out aircraft impact analysis on water. Therefore, the selection of the element plays an important role in this research. Solid elements are used to model water and soil bodies, while structures such as aircraft, helicopters, rigid balls, and penetrometers are modeled using shell elements.

Nonlinear analyses are mainly dependent on two factors: material properties and geometry. Nonlinear material properties do not obey Hook's law of the stress-strain curve. Nonlinear materials that have high failure rates, such as very soft material like water, are usually modeled in LS-DYNA using MAT_NULL material with the help of the equation of state, which imparts additional material properties. Two types of EOS generally used for water impact analysis are linear polynomial and Grüneisen.

3.1 Water Properties

Material properties of water were validated using the three cases considered below, which have unique significance in water-impact research. First, water-impact analysis validation was carried out at the Germany Aerospace Centre [9]. Here, a rigid sphere with a velocity of 11.8 m/sec was impacted on the surface of water. Later, Jackson and Fuchs at the NASA Langley Research Center, Hampton [17], conducted experimental validations on water impacts using a penetrometer. Here, a penetrometer was subjected to free fall from a certain height and its velocity was calculated at 7.6 m/sec at the time of impact. In both research studies, the validation results were processed at the center of gravity on the body coming in contact with water, and the acceleration plot was observed. Another experiment was carried out by Ramalingam and Lankarani [24] and Randhawa and Lankarani [32] on water impact analysis using a flask and ball to validate water properties using the displacement parameter.

3.2 Model Development and Validation of Water Impact Analysis with Rigid Sphere

The validation procedure from the Pentecote and Kindervater experiment [23] was considered and implemented in LS-DYNA. In the validation analysis, more emphasis was placed on material modeling in order to better exhibit water properties and in order to use the obtained material properties in other water applications in impact simulations. Due to the material modeling in FEA, elements exhibit viscosity and a hydrodynamic nature. Widely used water properties in LS-DYNA for water impact are listed in Table 3.1.

Figure 3.1 shows the mesh density and element size of the rigid sphere that was subjected to impact at a velocity of 11.8 m/sec onto a water medium. The mass of the rigid sphere was assumed to be 3.79 kg. Tables 3.2 and 3.3 show the properties of water used in these analyses. Shell and solid elements were considered for modeling the rigid ball and water pit. The water pit

dimensions were 0.56x0.56x0.25 m, and the mesh seeding was 112x112x25. Water was modeled using solid elements with a mesh size of 0.005 m, and the rigid sphere was modeled using a shell element size of 0.0125 m. The mesh density of the rigid sphere was 14, as shown in Figure 3.1 (b), and material properties of the Aluminum 7075-T6 rigid sphere are found in Table 3.4.

TABLE 3.1

MATERIAL PROPERTIES OF WATER USED IN WATER IMPACT ANALYSIS [9, 40]

Property	Case 1	Case 2	Case 3
EOS	Linear Polynomial	Grüneisen	Linear Polynomial
Density (Kg/m ³)	1000	1000	1000
Pressure Cut-Off (Kg /m.sec ²)	-1e11	-1e11	-1e11
Viscosity Coefficient	8.68e-4	8.68e-4	8.68e-4
Bulk Modulus (Pa)	2.25e-9	-	2.25e-9
Initial Internal Energy (E ₀)	0	0	0
Initial Relative Volume (V ₀)	0	1	1

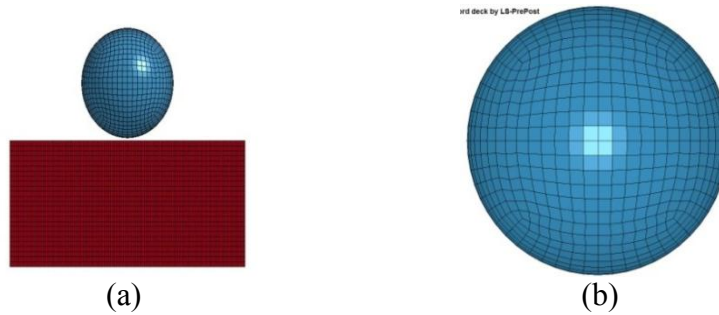


Figure 3.1. Mesh density and element size of rigid sphere: (a) mesh density of 14 and element size of 0.005 m, and (b) element size of 0.0125 m.

TABLE 3.2

LINEAR POLYNOMIAL PARAMETERS [9]

Parameter	Case 1	Case 3
C ₀ (Pa)	2.25e-9	2.25e-9
C ₁ (Pa)	0	7.5e9
C ₂ (Pa)	0	1.25e10

TABLE 3.3

GRÜNEISEN PARAMETERS IN CASE 2 [41]

Velocity of Sound, C (m/sec ²)	1480
Grüneisen Gamma (γ_0)	0.4934
Volume Correction (a)	1.397
Coefficient (S ₁)	2.56
Coefficient (S ₂)	-1.986
Coefficient (S ₃)	0.2286

TABLE 3.4

MATERIAL PROPERTIES OF RIGID BODY USED IN WATER IMPACT ANALYSIS [24]

Mass (kg)	3.76
Young's Modulus (Pa)	7.2e10
Poisson's Ratio	0.33
Shell Thickness (m)	0.005

As mentioned previously, MAT_NULL was assumed for the water material properties in the LS-DYNA-based research. Equations (3.1) and (3.2) are the linear polynomial equation and Grüneisen equation, respectively, and other additional information to solve the equation is provided in Tables 3.2 and 3.3. Results are almost similar with respect to experimental results.

The linear polynomial equation is

$$P = C_0 + C_1\mu + C_2\mu^2 + C_3\mu^3 + (C_4 + C_5\mu + C_6\mu^2)E \quad (3.1)$$

where C_n values other than those found in Table 3.2 are zero.

The Grüneisen equation is

$$p = \frac{\rho_0 C^2 \mu \left[1 + \left[1 - \frac{\gamma_0}{2} \right] \mu - \frac{a}{2} \mu^2 \right]}{\left[1 - (S_1 - 1)\mu - S_2 \frac{\mu^2}{\mu + 1} - S_3 \frac{\mu^3}{(\mu + 1)^2} \right]} + (\gamma_0 + a\mu) \quad (3.2)$$

3.2.1 Lagrangian Approach for Water Impact Analysis with Rigid Sphere

Lagrangian analysis was carried out to validate the water property. Here, water was modeled using solid elements while considering boundary conditions. The surface around the water pit and bottom region were constrained in the X, Y, and Z directions and rotational degrees of freedom (DOF). The bodies were in contact with each other using the contact card CONTACT_AUTOMATIC_SURFACE_TO_SURFACE, in which the slave and master surfaces automatically reorganize the nodes during analysis and establish contact between the surfaces. Another global loading condition in the analysis was LOAD_DENSITY_DEPTH, which is used for analyzing underground and submerged structures for preload and hydrostatic pressure on the body. The INITIAL_VELOCITY_RIGID_BODY card was used to generate velocity.

The rigid sphere material properties are shown previously in Table 3.4. In this analysis, the rigid spherical body was subjected to impact on the surface of water. The impact ripples that formed on the surface of water were replicated in the simulation, as shown in Figure 3.2.

Figure 3.3 is a graph that shows water properties were closer to the original experiment results. In these three cases, the MAT NULL card was used as the common card, and the EOS cards differed in the three cases. After applying the EOS to material properties, an analysis was simulated. Mesh refinement is another important parameter and plays a significant role in construction of the water pit in FEM analysis. Mesh studies were carried out to obtain suitable mesh for the water impact analyses. The mesh size had to be 0.005 m.

Figure 3.3 shows graphs of the three cases based on material properties defined using EOS of the water impact analysis. In these cases, an initial peak can be observed while the rigid body is in contact with the water, and reaches a maximum ranging between 70 to 80 g, which

then subsides. Later on, the peaks are small and caused by hydrodynamic forces. The maximum g-values obtained are 79 g in case 1, 74.5 g in case 2, and 74 g in case 3, as shown in Figure 3.3.

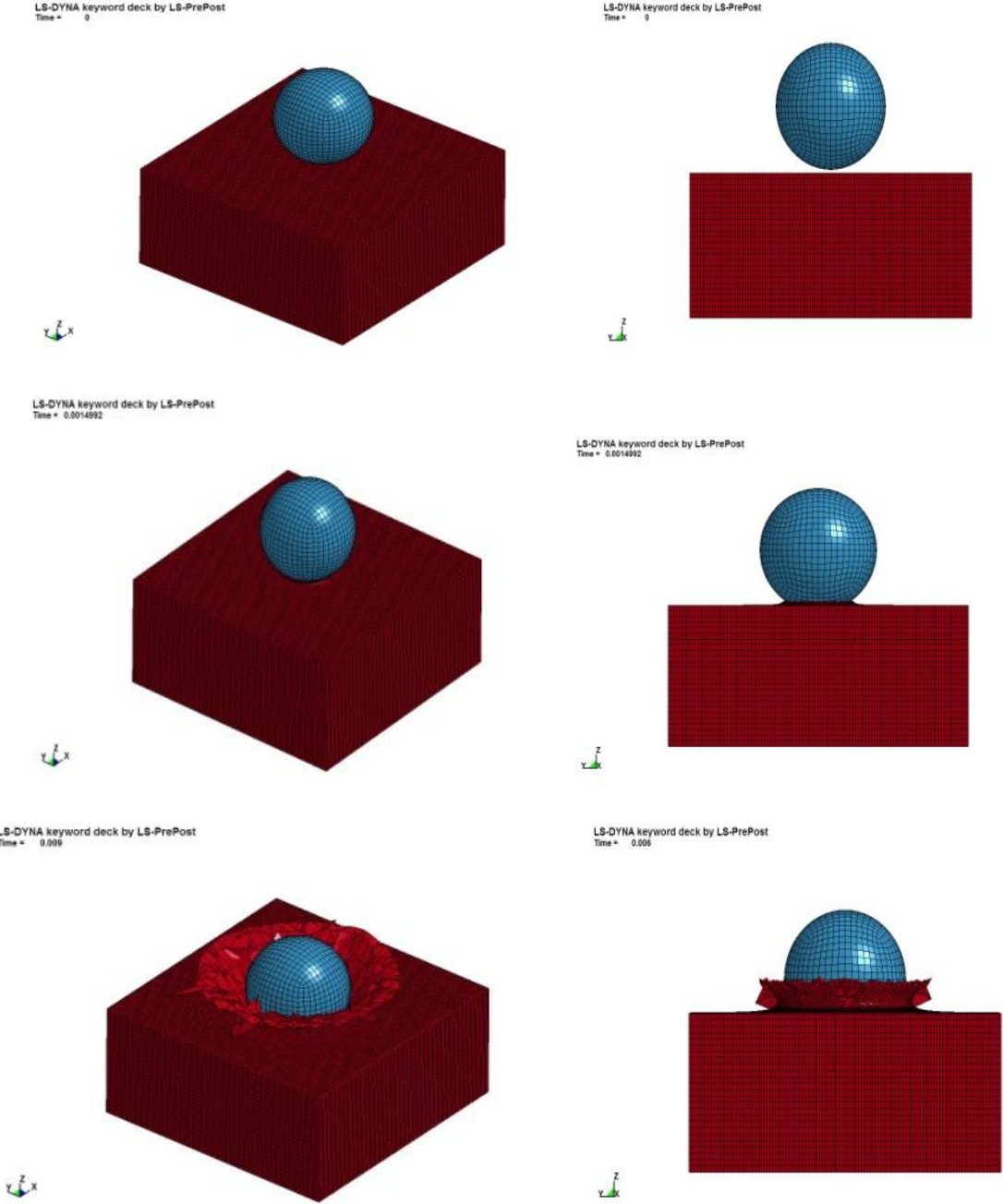


Figure 3.2. Lagrangian simulation of rigid body impact.

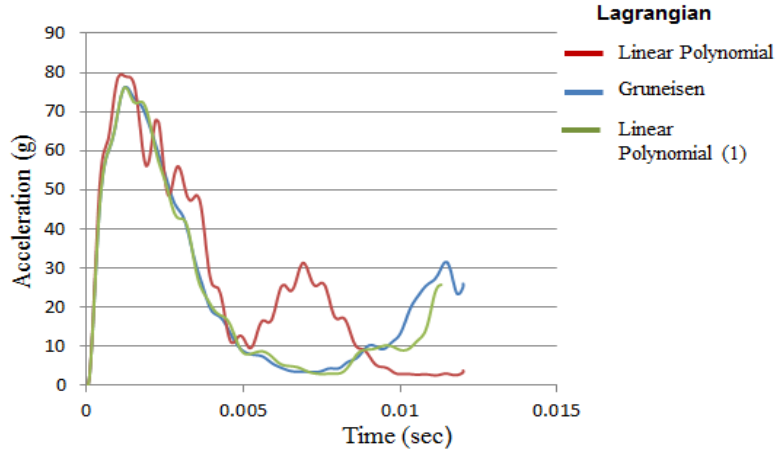


Figure 3.3 Graph of Lagrangian simulation with different material properties.

3.2.2 ALE Approach for Water Impact Analysis with Rigid Sphere

ALE analysis was carried out to validate the water properties. In this simulation, material properties of the water, soil, and rigid sphere were identical to those shown previously in Tables 3.1,3.2; boundary conditions, initial velocity, and body meshes were similar to those in the Lagrangian simulations. An air medium was added to the ALE modeling to observe material flow. In ALE analysis, mesh size of the air was similar to that of the water pit. Material properties of air are listed in Table 3.5. Figure 3.4 represents the mesh used in the ALE analysis, while the material properties of air were defined using MAT_NULL and EOS. Contact between the rigid sphere and water was replaced with a constrained card (CONSTRAINED_LAGRANGE_IN_SOLID), which was used as a coupling mechanism in the fluid-structure interaction. Mesh flow from the water region to the air region can be seen in Figure 3.5.

TABLE 3.5

MATERIAL PROPERTIES OF AIR USED IN ALE TECHNIQUE [35]

Density (Kg/m ³)	1.745e-5
Viscosity Coefficient	1.252
Velocity of Sound C (m/sec ²)	343.7
Grüneisen Gamma (γ_0)	1.4

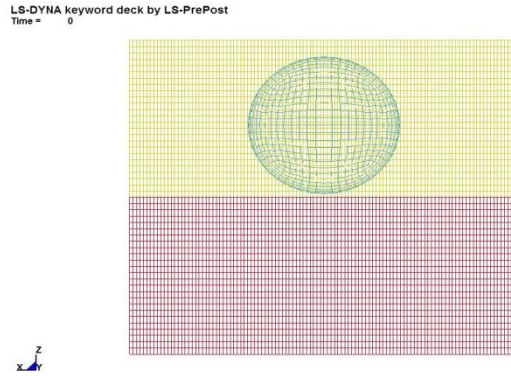


Figure 3.4. Mesh in ALE experiment setup.

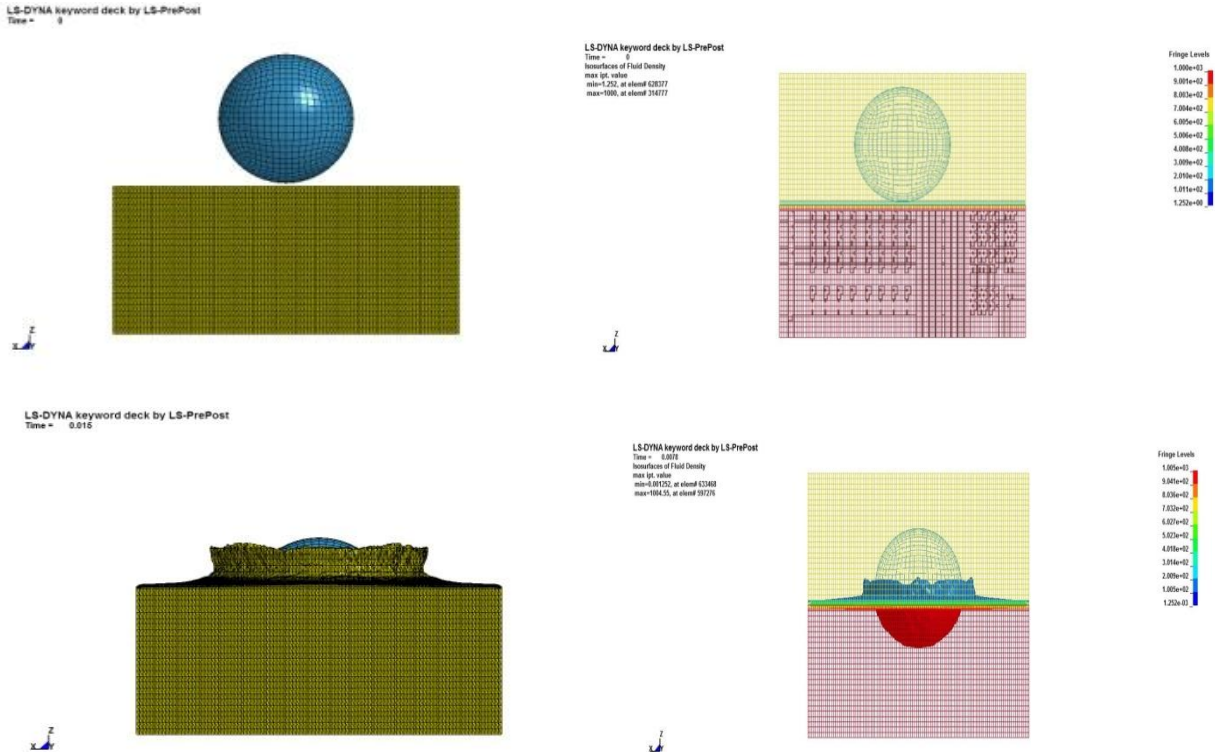


Figure 3.5. ALE simulation of rigid body impact.

Figure 3.6 shows the ALE simulation of a rigid sphere passing through air and impacting a water surface. Maximum acceleration obtained for the rigid sphere was 70 g. The hydrodynamic forces of water can be observed in the next highest peak at 59 g.

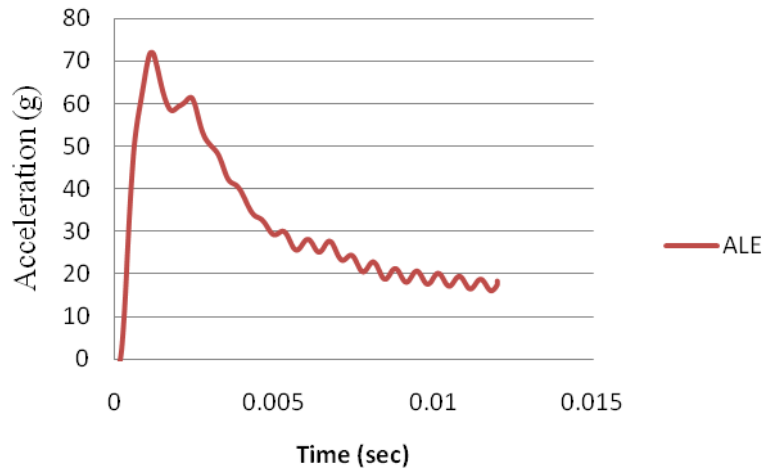


Figure 3.6. Graph of acceleration vs. time for rigid ball in ALE simulation.

3.2.3 SPH Approach for Water Impact Analysis with Rigid Sphere

SPH analysis was also carried out to validate water properties. SPH analysis is also known as meshless analysis. The material properties were identical to the above two cases. The analysis setup was similar to that of the Lagrangian analysis, apart from the modeling method. The difference between the SPH method and previous methods is that water is not modeled using elements but rather nodes. The water pit was modeled using nodes, and the distance between each node was 0.005 m because mesh size is considered, as mentioned in the above cases. The contact card used to establish contact between the two surfaces was CONTACT_AUTOMATIC_SURFACE_TO_NODES, which is similar to the CONTACT_AUTOMATIC_SURFACE_TO_SURFACE card. Figure 3.7 shows the water simulation using the SPH method, including the nodes making a splash. Initially water particles penetrated through the rigid surface. To control the penetrations in the simulation, the contact thickness was

increased. In impact simulations, the spline distance plays an important role in withstanding impact, and the distance must be between 0.2 and 1.2.

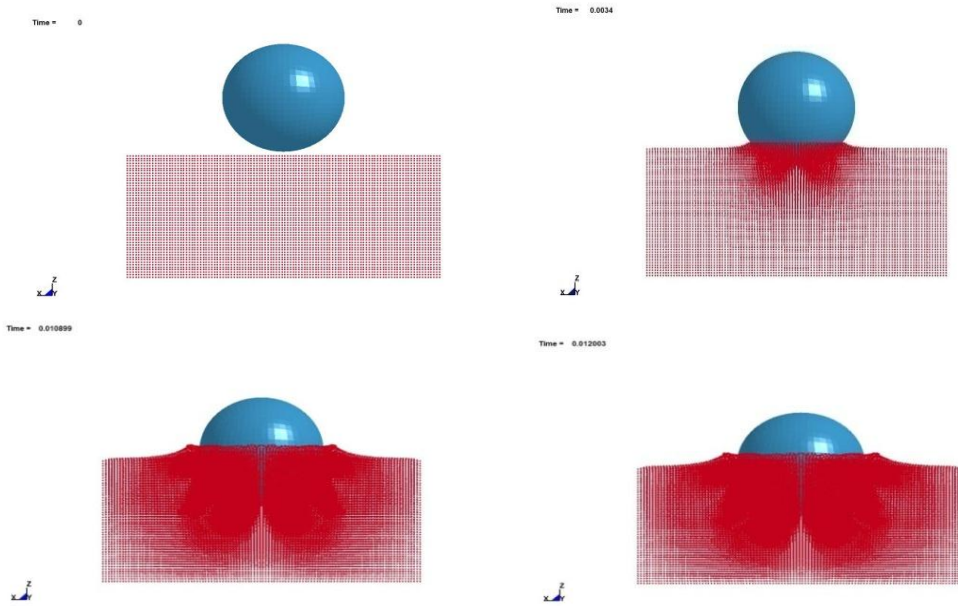


Figure 3.7. SPH simulation of rigid body impact.

Figure 3.8 represents acceleration versus time using the SPH method. Results were passed through filters with SAE 1000 Hz in order to cancel out the noise. The maximum peak obtained was 75 g, which is higher than results obtained from Lagrangian and ALE methods.

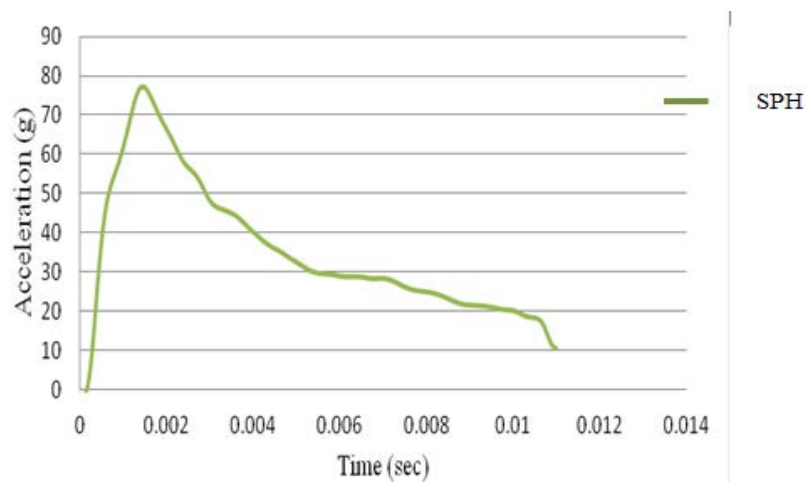


Figure 3.8. Graph of acceleration vs. time for rigid ball in SPH simulation.

3.3 Model Development and Validation of Water Impact Analysis Using Ball and Flask Experiment

In the water property validation, the displacement parameter was analyzed with the help of a ball and flask simulation and later compared with the experimental results. A ball was released from a predetermined height and equalized to 1.41 m/sec velocity. The material properties were assumed to be the same as in the previous case. The water flask had a radius of 0.058 m and was 0.154 m high with mesh seeding of 32x32x15. The boundary condition, contact cards, constraint cards, control cards, and mesh size were kept the same as in previous methods. Material properties of the Aluminum 7075-T6 rigid ball are listed in Table 3.6.

TABLE 3.6

MATERIAL PROPERTIES OF RIGID BALL USED IN FLASK EXPERIMENT [26].

Mass (kg)	40.8e-03 kg
Young's Modulus (Pa)	7.2e10
Poisson's Ratio	0.33
Shell Thickness (m)	0.001

3.3.1 Lagrangian Approach for Water Impact Analysis Using Ball and Flask Experiment

In this Lagrangian analysis, a ball was released from a certain height and equalized to 1.41 m/sec velocity. Material properties, mesh size, and LS-DYNA cards required to run the simulation were similar to that of the previous analysis discussed in Section 3.2.1 using the Lagrangian method. As shown in Figure 3.9, the ball hit the surface and penetrated through the water. Compared to Section 3.2.1, the initial velocity was assumed to be less because of those elements that were not distorting.

Figure 3.10 shows the relationship of displacement vs. time of analysis. This graph is similar to that exhibiting the experimental results. At 0.04 sec, the ball impacted the surface of the water.

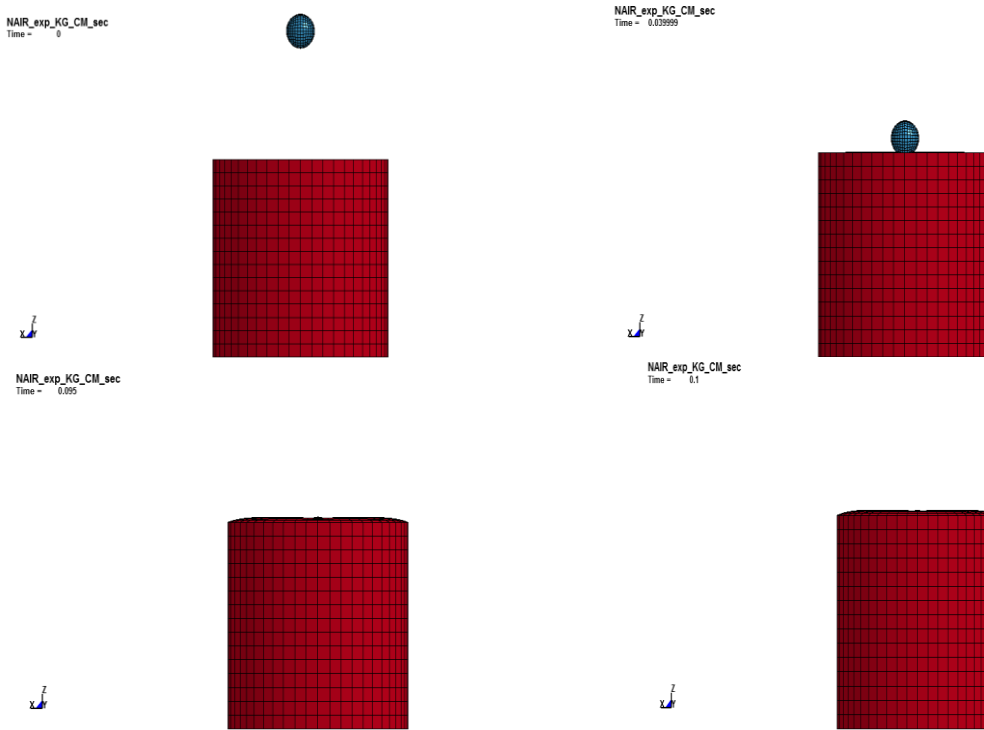


Figure 3.9. Lagrangian simulation of ball and flask experiment.

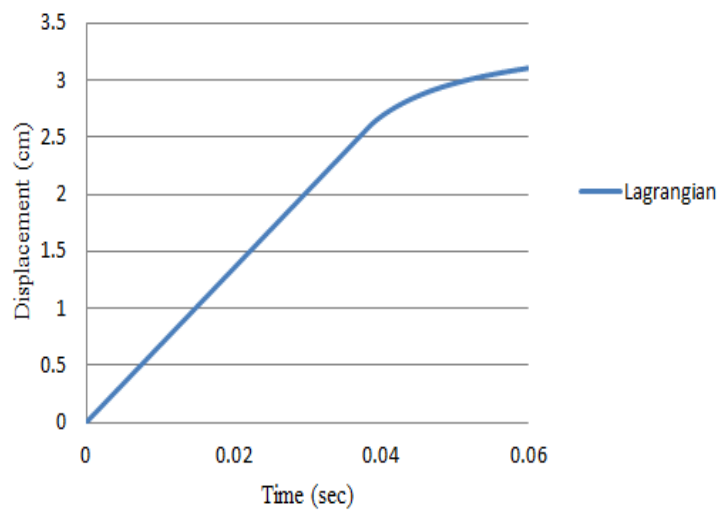


Figure 3.10. Graph of displacement vs. time for ball in Lagrangian simulation.

3.3.2 ALE Approach for Water Impact Analysis Using Ball and Flask Experiment

In ALE analysis, material and mesh size were similar to that of the simulations mentioned in Sections 3.2.2 and 3.3.1. As can be seen in Figure 3.11, air mesh is hidden for better view of the results. The constraint card imparted velocity to the rigid sphere. Air mesh was also modeled in a manner similar to that of water so that the material could flow. The computational time was much higher than compared to that of the Lagrangian analysis because of the additional air mesh, which increased the number of elements.

Figure 3.12 shows a graph of the ALE results, which are similar to those of the Lagrangian and experimental results. As can be seen, resistance was offered by water at a contact time of 0.04 sec. The MAT NULL material exhibited a linear increment graph, but after applying the EOS equation to that material, a hydrodynamic property on the water can be observed in the displacement vs. time graph.

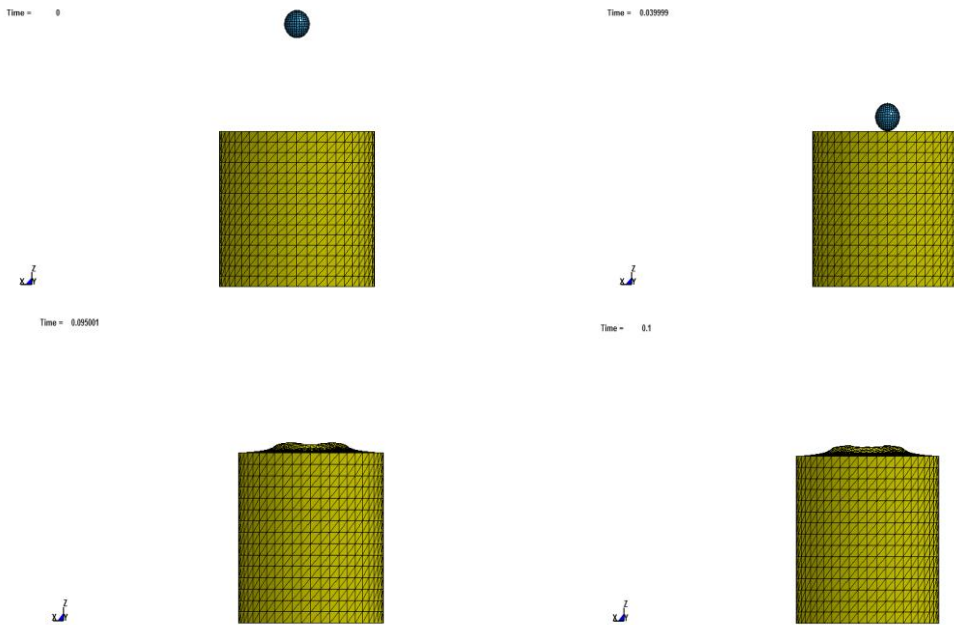


Figure 3.11. ALE simulation of ball and flask experiment.

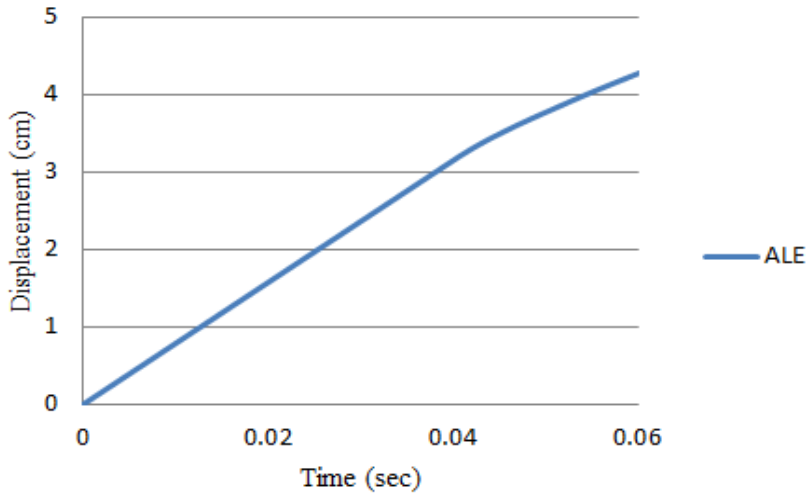


Figure 3.12. Graph of displacement vs. time for ball in ALE simulation.

3.3.3 SPH Approach for Water Impact Analysis Using Ball and Flask Experiment

The SPH water impact analysis using the ball and flask was similar to the SPH analysis using the rigid sphere, as discussed in section 3.2.3. In SPH simulation, nodes play a vital role in withstanding velocity during impact analysis. Individual nodes are bound to each other by a spline function, which can be controlled with SECTION_SPH. Figure 3.13 shows the animation of the SPH analysis carried on a flask containing water.

Figure 3.14 plots displacement vs. time for SPH analysis. Because formulations for SPH are derived from the Lagrangian method, results may be similar to that of the Lagrangian analysis, but the characteristics and applications are different. The MAT NULL material exhibits a linear increment in the graph due to application of the EOS equation. Hydrodynamic properties can be observed in the displacement vs. time graph.

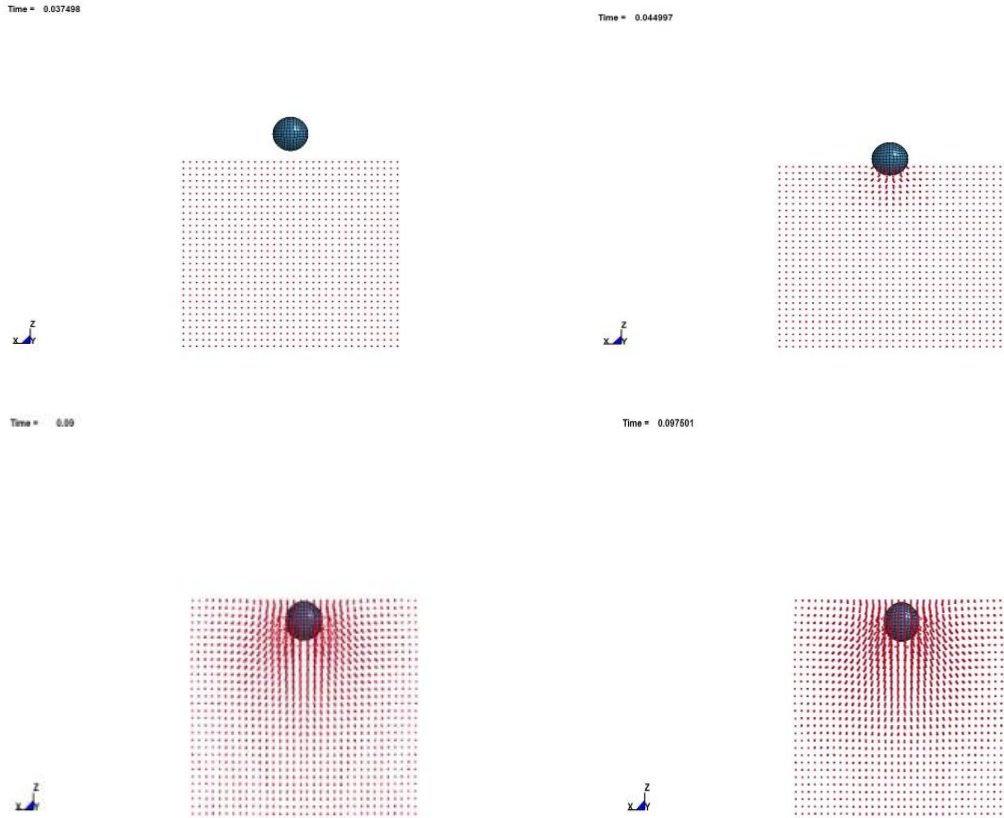


Figure 3.13. SPH simulation of ball and flask experiment.

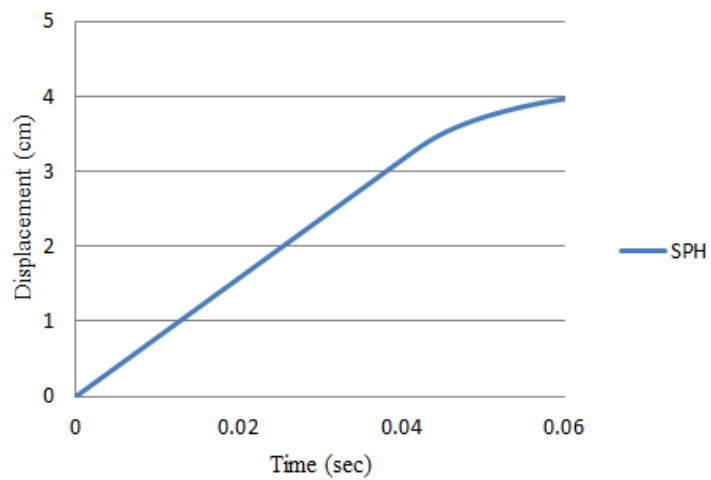


Figure 3.14. Graph of displacement vs. time for ball in SPH simulation.

3.4 Model Development and Validation of Water Impact Analysis Using Penetrometer

Water validation impact analysis was carried out using a penetrometer in which the bob was semi-spherical with a circular bottom. The mesh was maintained at 0.03 m. Material properties used for this analysis had to be identical as mentioned in case 3 in Section 3.2. The material properties of the penetrometer are list in Table 3.7. The mesh style is shown in Figure 3.15 for different cases of mesh seeding. The water body dimensions were 0.9 m radius and 0.9 height. In case 1, the mesh seeding was 110x110x23, and in case 2, the mesh seeding was 110x110x46. In the numerical analysis, contact, control card, boundary conditions, and other parameters were similar to that of previous water-impact simulations. The mass of the penetrometer was around 29.03 kg, the shape of the water body was assumed to be cylindrical in nature, and the container was similar to that of the water dam. Simulation was done on a freely falling body analysis from a certain height at a velocity of 7.28 m/sec. The entire diameter of the water dam was assumed to be 0.6096 m. In the analysis, the rigid body was assumed to be aluminum. The simulation, shown in Figure 3.15, aimed to validate the water material property and mesh style used for the SPH analysis.

TABLE 3.7

MATERIAL PROPERTIES OF PENETROMETER USED IN WATER IMPACT ANALYSIS [23]

Mass (kg)	29.03
Young's Modulus (Pa)	7.2e10
Poisson's Ratio	0.33
Shell Thickness(m)	0.005

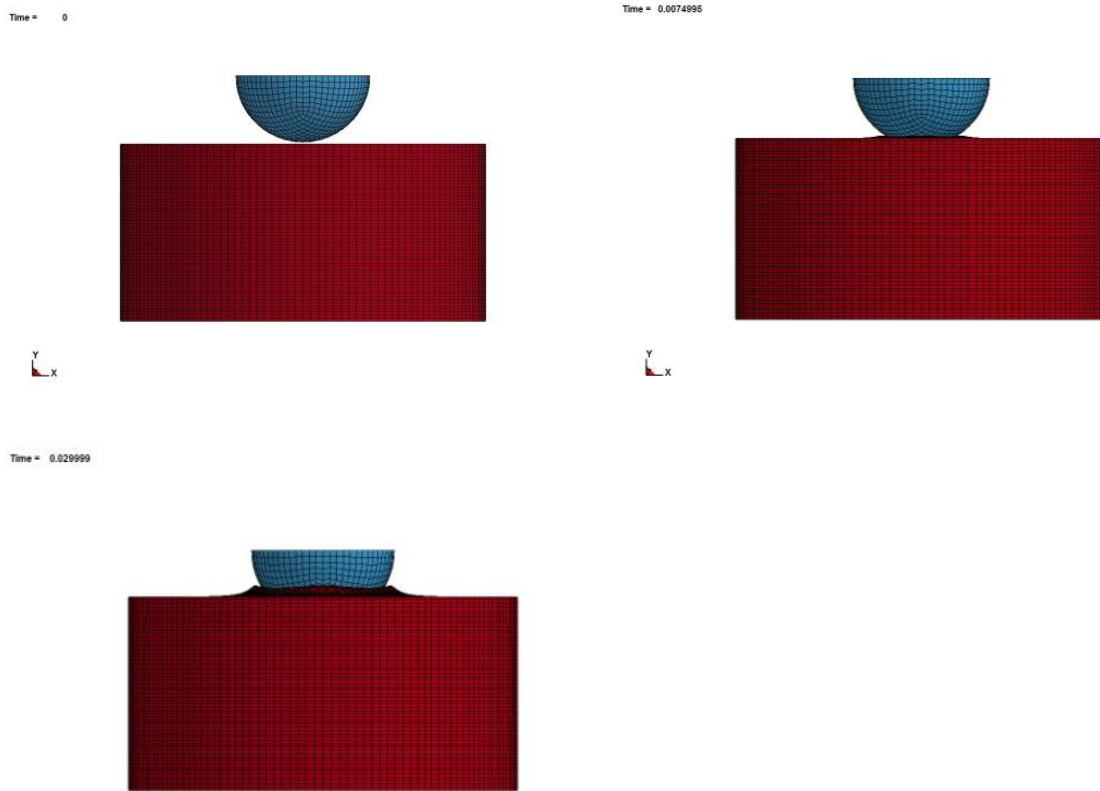


Figure 3.15. Lagrangian simulation of water impact using penetrometer.

3.4.1 Lagrangian Approach for Water Impact Analysis Using Penetrometer

In the Lagrangian approach to the penetrometer impact analysis, the bob was subjected to impact on the surface of the water after dropping from a certain height. Material properties and all other important requirements were the same as from the previous analysis, as mentioned in Section 3.3.1 about the Lagrangian method. A water pit was constructed as a cylinder. Figure 3.15 shows the bob hitting the surface and penetrating the water. The animation here indicates that water splash can be observed. The penetrometer was considered to be a free falling body with velocity less than 7.28 m/sec. Analysis was divided into two cases—case 1 and case 2—according to mesh seeding. The mesh seeding in case 1 was 110x110x23 and in case 2 was 110x110x46.

Figure 3.16 are graphs of acceleration vs. time in cases 1 and 2. The second peak in case 1 is 38 g, but in case 2, the second peak is around 55 g. There is visual evidence of hydrodynamic forces. Early analysis did not concentrate on finding the buoyancy effect, but by conducting this analyses, it is evident that the water property used in this FEM analysis replicates real water. Therefore, in the application part of this experiment, a same mesh size of 0.005 m and water properties were maintained.

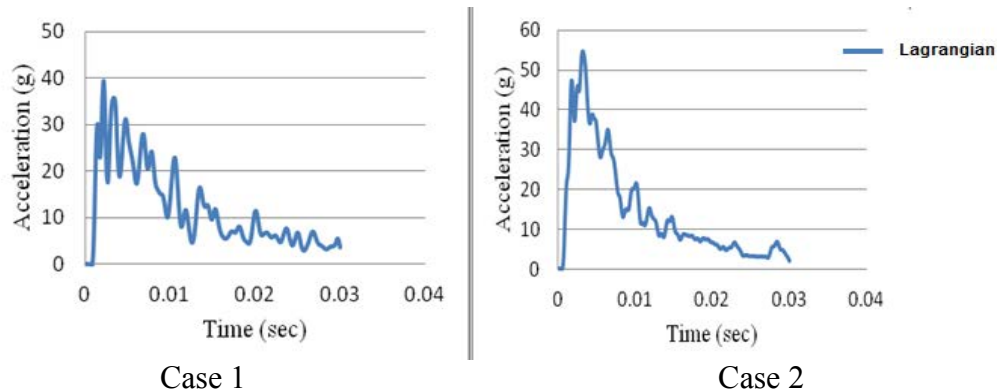


Figure 3.16. Graph of acceleration vs time for penetrator in Lagrangian simulation. Case 1 mesh seeding was $110 \times 110 \times 23$, and case 2 mesh seeding was $110 \times 110 \times 46$.

3.4.2 ALE Approach for Water Impact Analysis Using Penetrator

ALE analysis of a water impact using a penetrator, as shown in Figure 3.17, was similar to that of the water impact ALE simulation discussed in Section 3.2.2. Mesh size and air properties were similar to those in the Lagrangian water impact analysis mentioned in the earlier analysis involving the ALE method. A constraint card was used to apply velocity, as discussed in earlier ALE cases. ALE formulations typically undergo adaptive mesh due to advection. Results from the ALE analysis when the mesh was varied showed consistency. Figure 3.18 shows a small peak initially and later another peak of 42 g at 0.04 second. This graph is plotted in acceleration vs. time. Simulation results when the mesh was varied were similar.

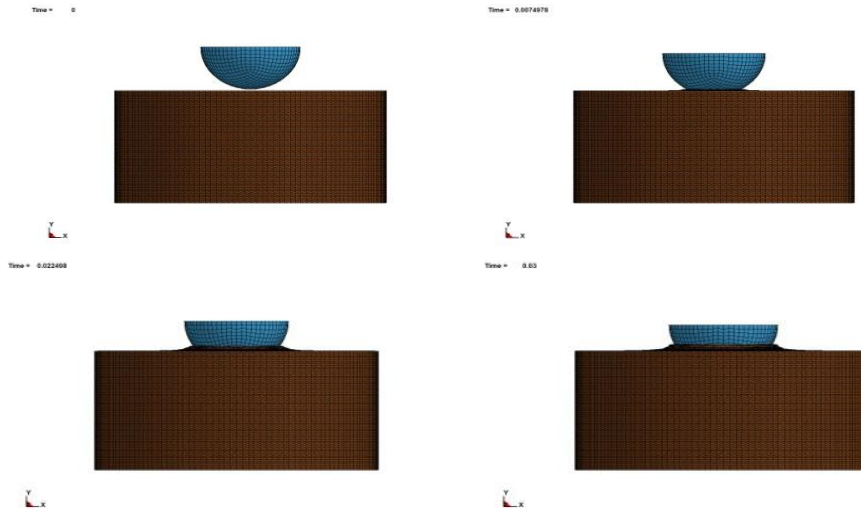


Figure 3.17 ALE simulation water impact analysis using penetrometer.

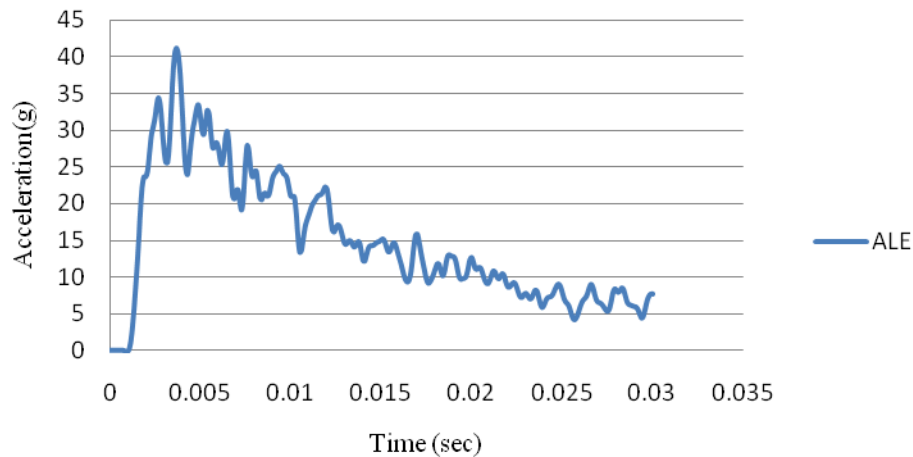


Figure 3.18 Graph of acceleration vs. time for penetrometer in ALE simulation.

3.4.3 SPH Approach for Water Impact Analysis Using Penetrometer

SPH analysis was carried out in a similar fashion as mentioned in the earlier SPH analysis. Analysis was divided into two cases depending on mesh density. In SPH analysis, mesh density is referred to as mesh seeding or mesh size. The basic differences between both cases are the number of nodes and distance between nodes. In both cases, mesh size was maintained around 0.01 m, but the mesh seeding differed: case 1 was 110x110x23 and case 2 was 110x110x46. Figure 3.19 shows the particles forming waves in the SPH simulation.

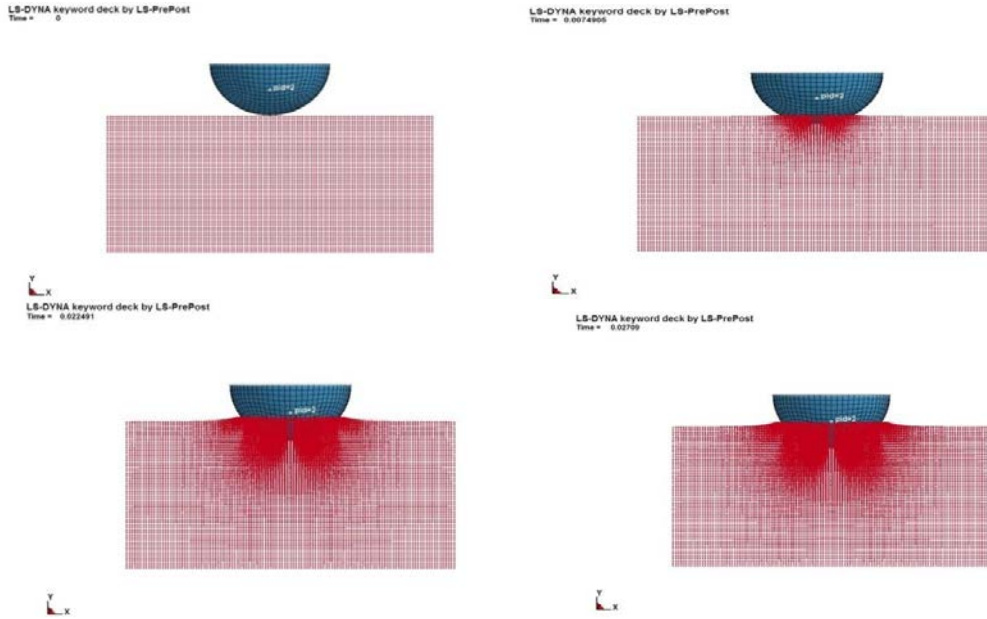


Figure 3.19 SPH simulation on water impact using penetrometer.

Figure 3.20 plots acceleration and time in the SPH analysis. The case 1 graph is shown in Figure 3.20 (a) and the case 2 graph in Figure 3.20 (b). In case 1, the maximum peak was at 52 g and not equivalent to the experimental graph, which was around 38 g. In case 2, the maximum peak was around 39 g, which is similar to the experimental results. In this research, the distance maintained between each node was 0.005 m for the impact analysis on water using both a helicopter and an aircraft. Due to the mesh density, the number of nodes in the analysis also increased, resulting in a high computational time.

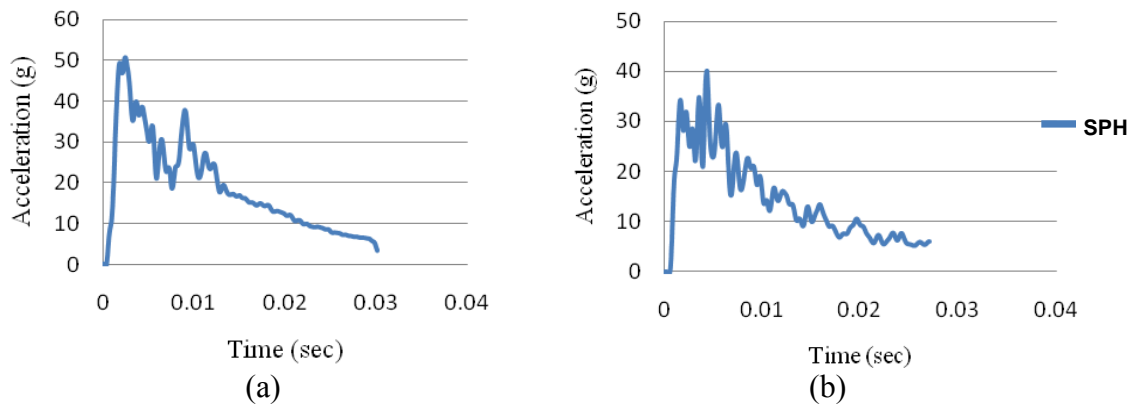


Figure 3.20. Graph of acceleration vs time for penetrometer in SPH simulation. Case 1 mesh seeding was 110x110x23, and case 2 mesh seeding was 110x110x46.

CHAPTER 4

MODEL DEVELOPMENT AND VALIDATION OF IMPACT ON SOIL

4.1 Validation of Soft Soil Properties

The soft soil material properties were obtained from NASA-conducted research. Fasanella et al. conducted soft soil experiments at NASA [19] with a penetrometer, and all experimental data was compared to numerical simulations. The soil was also a nonlinear material, where the MAT_SOIL_AND_FOAM material card was utilized. The National Transportation Safety Board has developed soil barrier testing. Soil material modeling is of a soft and crushable nature and is solved like foam-related problems. Material properties of the penetrometer and soil are shown in Tables 4.1 and 4.2, respectively. The stress vs. strain curve for soft soil is shown in Figure 4.1.

TABLE 4.1

MATERIAL PROPERTIES OF PENETROMETER USED IN SOIL IMPACT ANALYSIS [19]

Mass (kg)	9.071
Young's Modulus (Pa)	7.2e10
Poisson's Ratio	0.33
Shell Thickness(m)	0.005

TABLE 4.2

MATERIAL PROPERTIES OF SOIL USED IN SOIL IMPACT ANALYSIS [19]

Density (Kg/m ³)	1.46e3
Shear Modulus (Pa)	1.84e6
Pressure Cut-Off (Kg/m sec ²)	6.894e3
Yield Function Constant for Plastic Yield Function (A ₂)	0.2

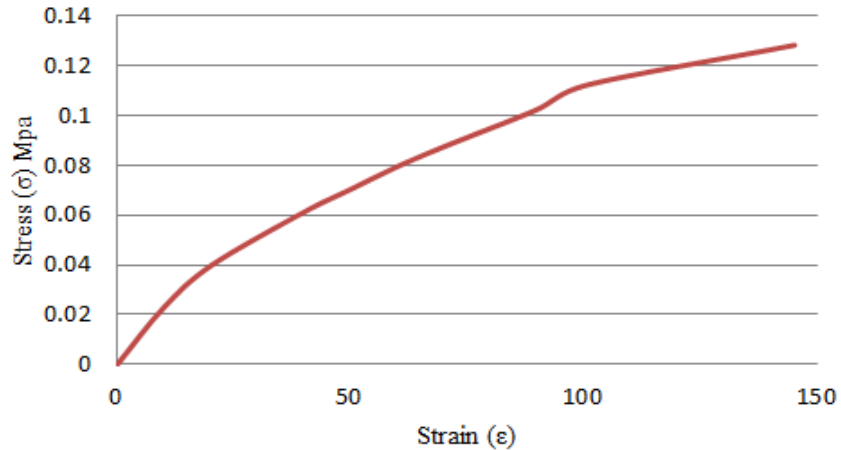


Figure 4.1 Stress vs. strain curve for soft soil [10].

4.2 Model Development and Validation of Soft Soil Impact Analysis Using Penetrometer

In the validation of soft soil, a rigid hemisphere shaped as a penetrometer was used to impact soil at a velocity of 4.876 m/sec using the metre kilogram second (MKS) unit system. Mass of the hemisphere-shaped penetrometer was 9.071 kg. Shell and solid elements were considered for modeling the rigid sphere and the water. The soil pit dimensions were 0.91x0.91x0.61 m, and the mesh seeding was 50x50x50. The soil model developed used solid elements with a mesh size of nearly 0.012 m and rigid shell elements of 0.012 m. In the analysis, mesh used by the soil pit was biased at the center and more emphasized on the surface of the soil that underwent impact. The test setup in Figure 4.2 shows the penetrometer impacting the surface of the soil and the resulting crater formation.

4.2.1 Lagrangian Approach for Soft Soil Impact Analysis Using Penetrometer

In the numerical simulation, soil was modeled using solid elements while considering boundary conditions for the soil pit. The surrounding surface and bottom region were constrained in the X, Y, and Z directions and rotational degrees of freedom. In this analysis, a gravity card was also activated. The analysis was similar to that of a water analysis with respect to material

nonlinearity, but material modeling was carried out using a MAT_SOIL_AND_FOAM formulation. The analysis consisted of 12,500 solid elements in the soil. The accelerometer data was taken from validation; therefore, the accelerometer data had many disturbances. To minimize this, filters were used to cut off frequencies in the graph. The contact card used in the simulation was CONTACT_AUTOMATIC_SURFACE_TO_SURFACE.

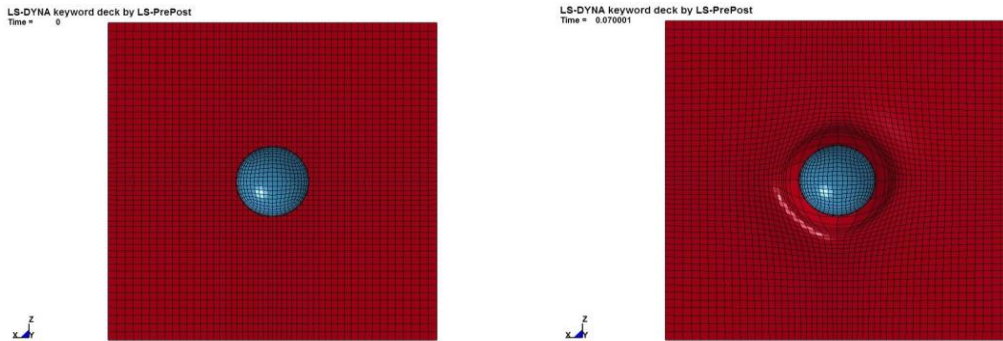


Figure 4.2. Test setup of soil impact analysis.

Figure 4.3 shows the impact of a rigid body on a soil surface in Lagrangian analysis. The penetrometer was subject to an initial velocity of 4.876 m/sec. Initially there was a resistance to penetration of the bob inside the soil. When a body impacts with soft soil, the velocity will decelerate and is differentiated with respect to time in order to derive the acceleration, which is used as parameter to validate this experiment. Resistance can be observed in the simulation with the help of graphs showing acceleration vs. time. Material properties of the penetrometer and soil used in this analysis are shown previously in Tables 4.1 and 4.2.

Figure 4.4 is a plot of the acceleration vs. time with respect to the penetrometer's center of gravity. According to experimental results, the graph obtained had to be between 16 g and 21 g. Figure 4.4 shows that the maximum peak is at 17.5 g in less than a 0.01-second time step. Another small peak is at 11 g after a fall from the second peak. Penetration into the soil dispersed in all directions; dissipation may cause a crater, as shown previously in Figure 4.2.

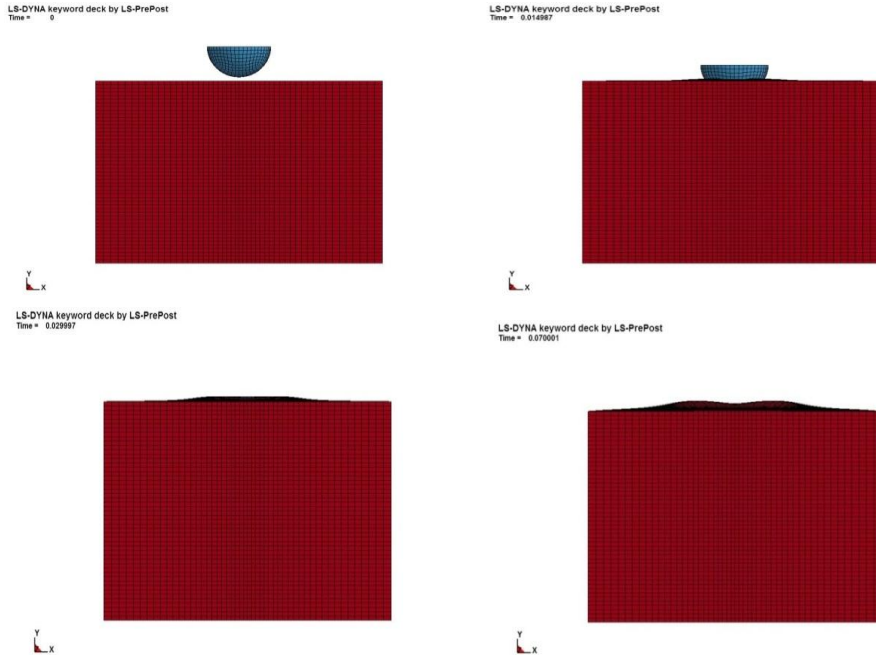


Figure 4.3. Lagrangian simulation of soil impact using penetrometer.

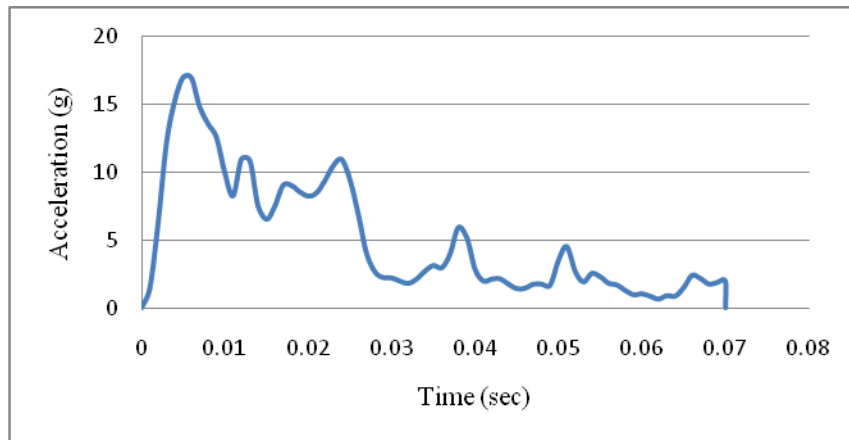


Figure 4.4. Graph of acceleration vs. time for soil impact analysis in Lagrangian simulation.

4.2.2 ALE Approach for Soft Soil Impact Analysis Using Penetrometer

ALE analysis of a soft-soil impact is also similar to that of Lagrangian analysis, as discussed in Section 4.2.1, but a dummy mesh is involved. Velocity is provided by the card `CONSTRAINED_LAGRANGE_IN_SOLID`, and also used as contact to be established between both Lagrangian and Eulerian mesh. In ALE analysis, the ALE multi-material (AMM) group

approach cannot be used. By using the AMM group card, simulation will undergo a negative advection cycle. Because solutions do not converge, the simulation will be terminated due to negative volume and velocity. Another ALE approach was adapted in this simulation which is carried by void material property. The SECTION_SOLID method was replaced with the 11th formulation (multi-material group) and then with the 12th formulation. The INITIAL_VOID card had to be utilized. By using this card, the entire part that is mentioned in the void card is nullified and considered dummy mesh. In Figure 4.5, air mesh has been displayed as well as an isometric layer view for a better pictorial representation.

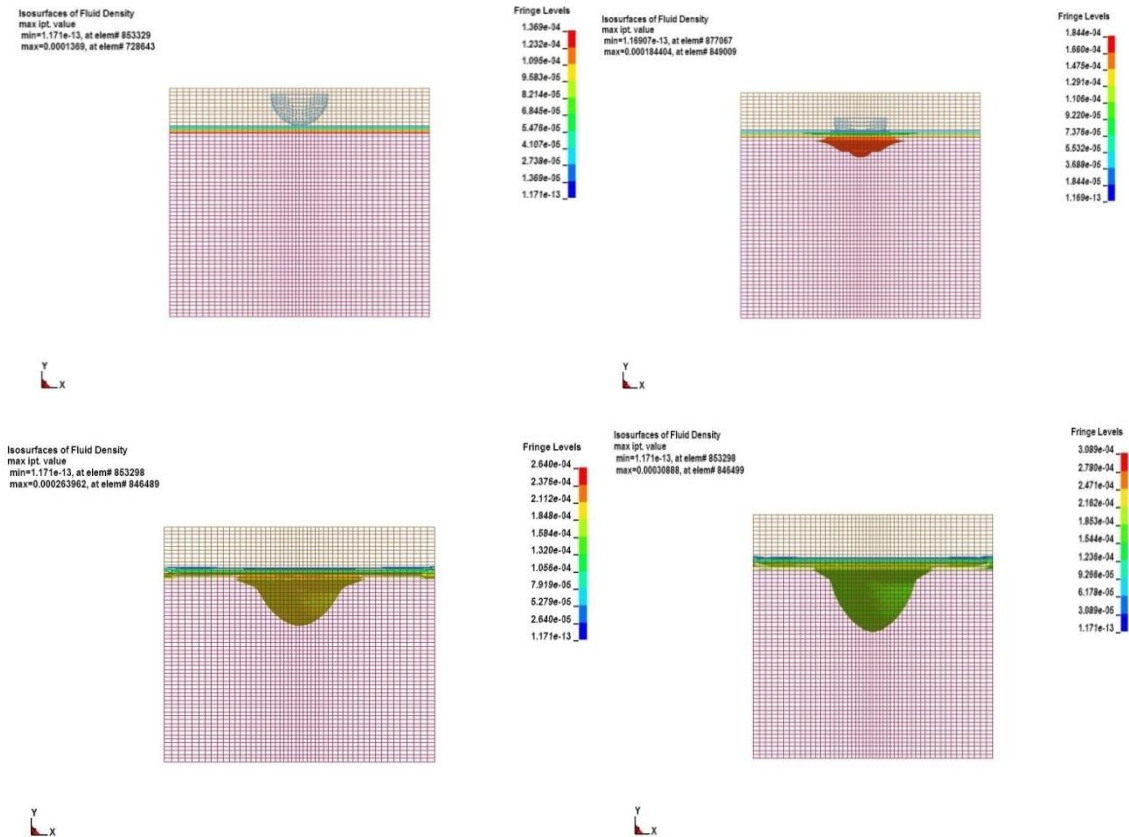


Figure 4.5 ALE simulation of soil impact using penetrometer.

Figure 4.6 represents a graph of acceleration vs. time in an ALE simulation while impacting the soil. In the analysis, the maximum peak is 20.2 g, and in the experiment, the

maximum peak is around 16 g to 21 g. Results of the analysis are in the acceptable region and similar to the experimental results.

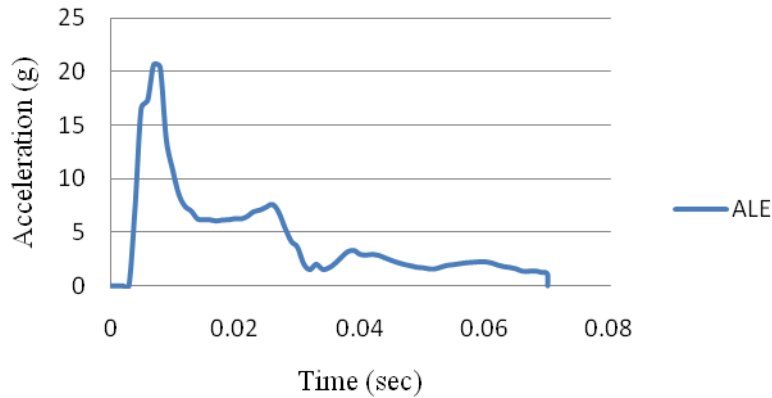


Figure 4.6 Graph of acceleration vs. time for soil impact in ALE simulation.

4.2.3 SPH Approach for Soft Soil Impact Analysis Using Penetrometer

Animation of the SPH method simulation is shown in Figure 4.7. Analysis was carried similarly as in the earlier SPH analysis. The control cards were similar but new cards known as CONTROL_SPH were used. The SECTION_SPH card was also used for simulation. Material and boundary conditions were similar as in the previous analysis. Arranged biased nodes can be observed in the simulation.

Figure 4.8 shows the relation of acceleration vs. time for the SPH analysis. In this graph, the maximum g obtained is 15.6 g, and another peak is at 11 g. Experimental results had to be between 16 g and 21 g, and peak values ranged between the solutions. As shown in Figure 4.8, at 0.06 sec, the penetrometer came into state rest and the soil absorbed the energy.

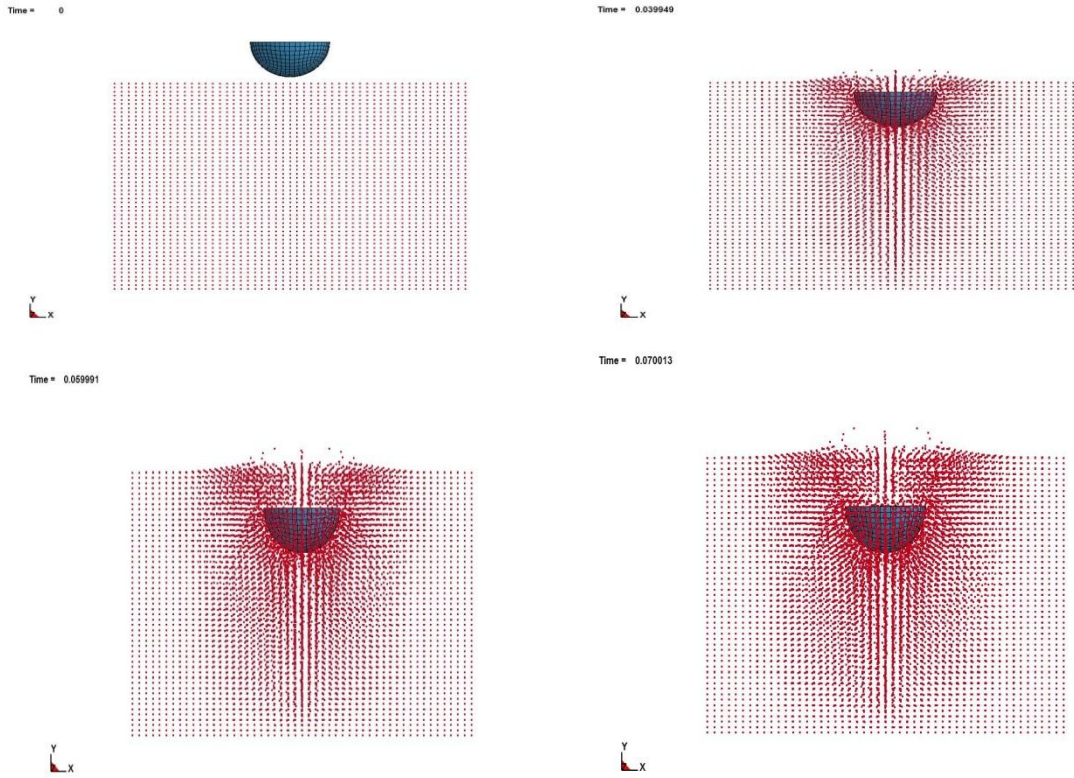


Figure 4.7 SPH simulation of soil impact analysis using penetrometer.

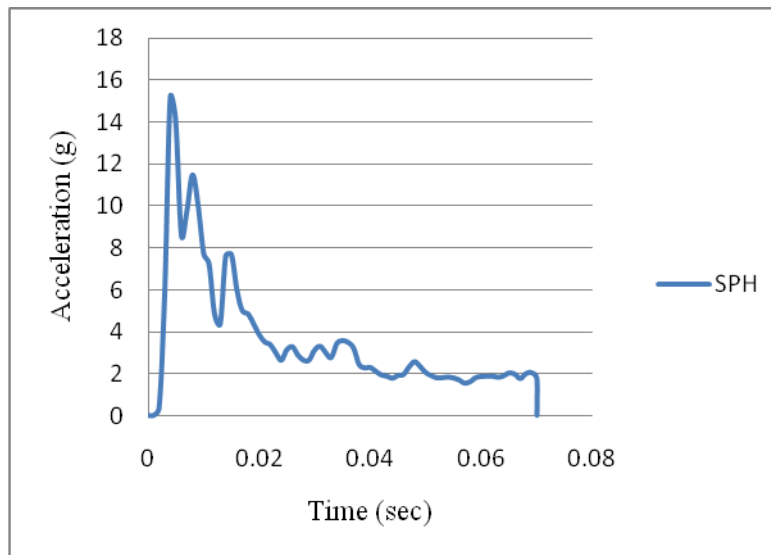


Figure 4.8 Graph of acceleration vs. time for soil analysis in SPH simulation.

CHAPTER 5

APPLICATION OF AIRPLANE AND HELICOPTER IMPACT ON WATER AND SOFT SOIL

5.1 Rotorcraft Impact Application

5.1.1 Rotorcraft Water Impact

This chapter discusses the results of a helicopter/rotorcraft that was subjected to impact on water and soil in order to observe the structural deformation while it underwent a crash landing. According to one FAR, a helicopter must undergo some regulations on ditching, as mentioned in Chapter 2. To meet the FEA regulation, an analysis was initiated with the help of a Huey UH1H rotorcraft, which was subjected to impact on water and soil. The dimensions of this helicopter, as represented in Figure 5.1, were considered for the analyses. The helicopter for the analysis was modeled using CAD software CATIA V18, and the discretized model was meshed using Hypermesh 10.0, as shown in Figure 5.2.

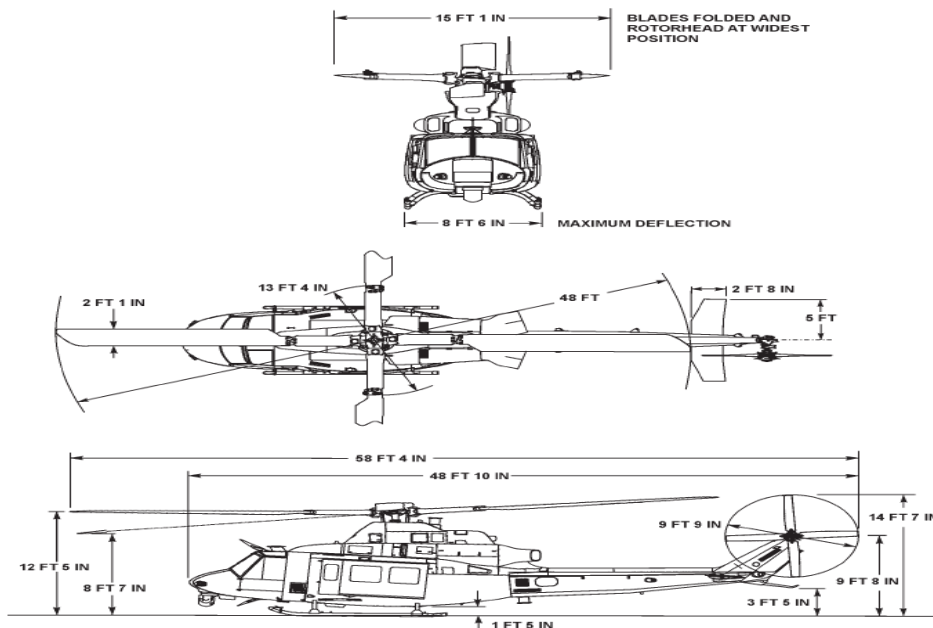


Figure 5.1. Dimensions of Huey UH1H helicopter [42].

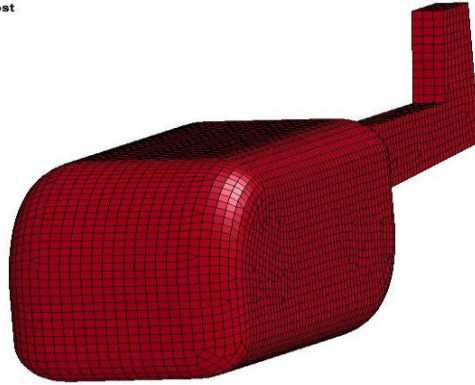


Figure 5.2. Modeled rotorcraft using 7,066 shell elements.

In the impact analysis, the mesh size for the rotorcraft was maintained around 0.001 m, as shown in Figure 5.2. The experiment was carried out on the helicopter fuselage alone, so only the fuselage dimensions were considered. The dimensions of the rotorcraft were as follows: main rotor diameter of 14.6 m, tail rotor diameter of 2.59 m, overall length of 17.61 m, length of fuselage of 12.78 m, and rotorcraft height of 4.42 m. The blades and landing gear were not considered in the design for the impact analysis on the fuselage because the center of gravity location would have been affected due to the presence of additional structures on the helicopter. The water pit used for the analysis consisted of the same water properties as discussed in Chapter 3.

The boundary condition, control cards, hourglass, contact, and section cards were identical to that of the previous water impact analysis carried out in Chapter 4. However, the major difference in this application impact analysis is that the rigid bodies were replaced with deformable bodies representing the actual rotorcraft structure. The water pit dimensions considered for analysis were 1.5x0.72x0.25 m, and the mesh seeding was 300x143x25. The number of shell elements in the rotorcraft was 7,066 and the number of solid elements in the water was 1,079,599. The weight of the rotorcraft was 1,030 kg. The material card used in this analysis was MAT_PLASTIC_KINEMATIC, and the material properties are shown in Table 5.1.

TABLE 5.1

MATERIAL PROPERTIES OF ROTORCRAFT [32]

Young's Modulus (Pa)	7.2e10
Poisson's Ratio	0.33

5.1.1.1 Lagrangian Approach for Water Impact Analysis with Rotorcraft

The Lagrangian analysis of a water impact with a rotorcraft was similar to that of all impacts carried out on water in Chapter 4. The material properties of the water and rotorcraft are shown previously in Tables 3.2, 3.3, and 5.1. Waves were formed due to the presence of EOS formulation in material properties, as mentioned in Chapter 4.

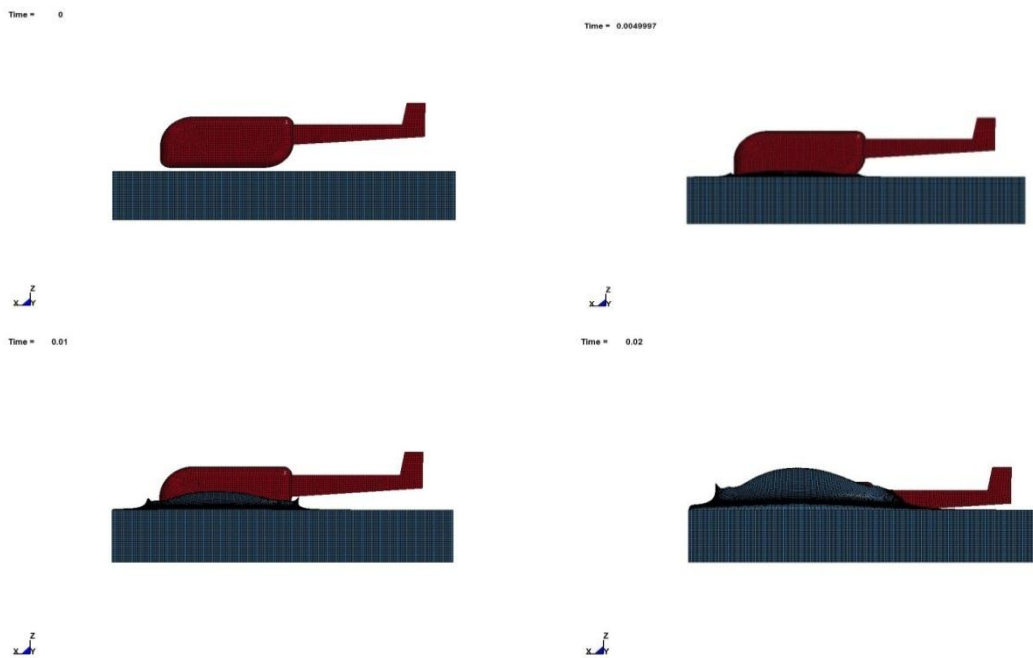


Figure 5.3 Lagrangian simulation of rotorcraft in water.

Figure 5.4 shows deformation of the helicopter structure in the impact analysis on water. Figure 5.4 (a) is at the beginning of the simulation, which represents no stress, and Figure 5.4 (b) is the final step of the simulation where structural deformation is observed. The red fringe pattern represents a stress area where the structure may fail.

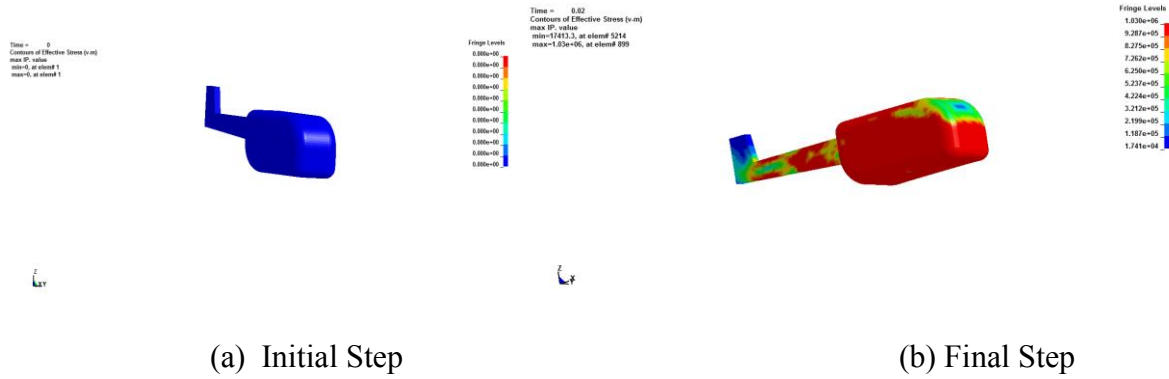


Figure 5.4. Deformation of rotorcraft.

Figure 5.5 is a plot of acceleration vs. time in the Lagrangian simulation. As can be seen, the maximum acceleration is at 71 g, and another peak is near 11 g. The g-values are identical to that of experimental g-values obtained near the co-pilot seat, which are around 69 g.

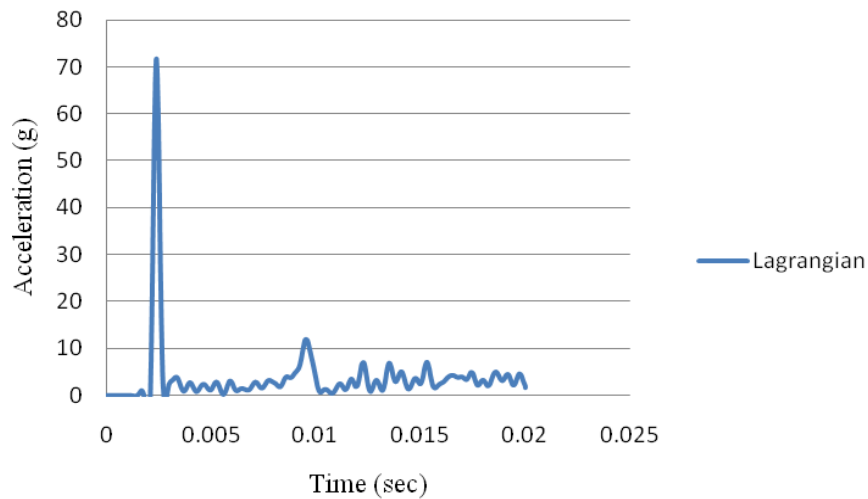


Figure 5.5 Graph of acceleration vs. time for rotorcraft in water in Lagrangian simulation.

5.1.1.2 ALE Approach for Water Impact Analysis with Rotorcraft

In this simulation, the material properties of water and the rotorcraft are shown previously in Table 3.2 and Table 5.1, respectively. The mesh seeding was 300x143x25. Figure 5.6 shows the simulation with ALE analysis where the air mesh is hidden. In the simulation,

water splash can be observed, while material is flowing from the actual mesh of the water to the dummy mesh of the air, as shown in Figure 5.6.

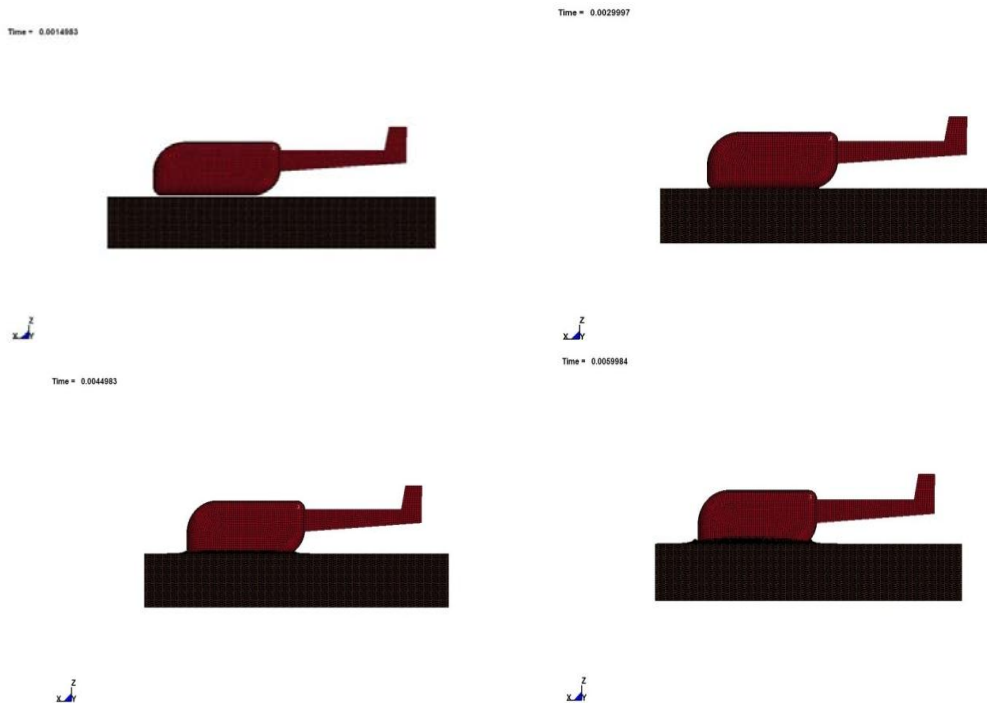


Figure 5.6 ALE simulation of rotorcraft in water.

Figure 5.7 is a graph of acceleration vs. time in the ALE simulation. The maximum acceleration obtained was 74 g, and another peak occurred at around 40 g. The g-values are similar to the experimental g-values obtained near the co-pilot seat, around 69 g, which is assumed to be the center of gravity.

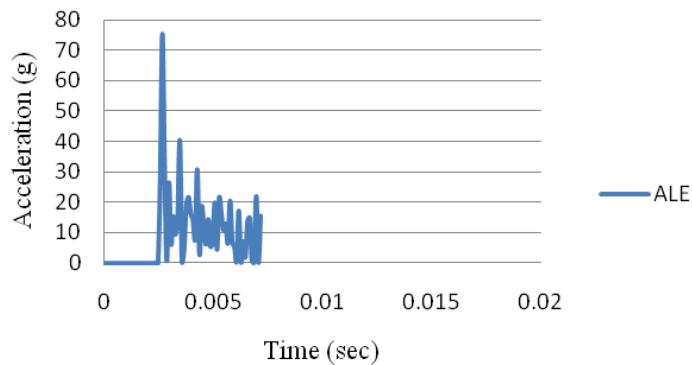


Figure 5.7. Graph of acceleration vs. time for rotorcraft in water in ALE simulation.

5.1.1.3 SPH Approach for Water Impact Analysis with Rotorcraft

The SPH analysis was similar to that of the water impact analysis in the earlier chapter on SPH. The time taken for the analysis to terminate was less than all simulations using Lagrangian and ALE approaches. The distance between each node was 0.005 m. The mesh seeding was 300x143x50, and the pit size was 1.5x0.71x0.25. In Figure 5.8, water splash formation can be observed in the form of nodes, which are closely modeled to the specified mesh size.

Figure 5.9 is a graph of acceleration vs. time. Maximum acceleration obtained from the analysis is 73 g, and another minimal peak is observed around 11g. The g-values from the analysis are similar to the experimental g-values obtained near the co-pilot seat, around 69 g, which is assumed to be the center of gravity. The error percentage estimation between the experimental method and the FEM in the Lagrangian process is 4%. Due to the presence of more nodes, the computational time was more than in the Lagrangian analysis, so analysis was limited to less time because the results obtained from Lagrangian analysis were similar to that of the SPH analysis because of the same nodal formulations.

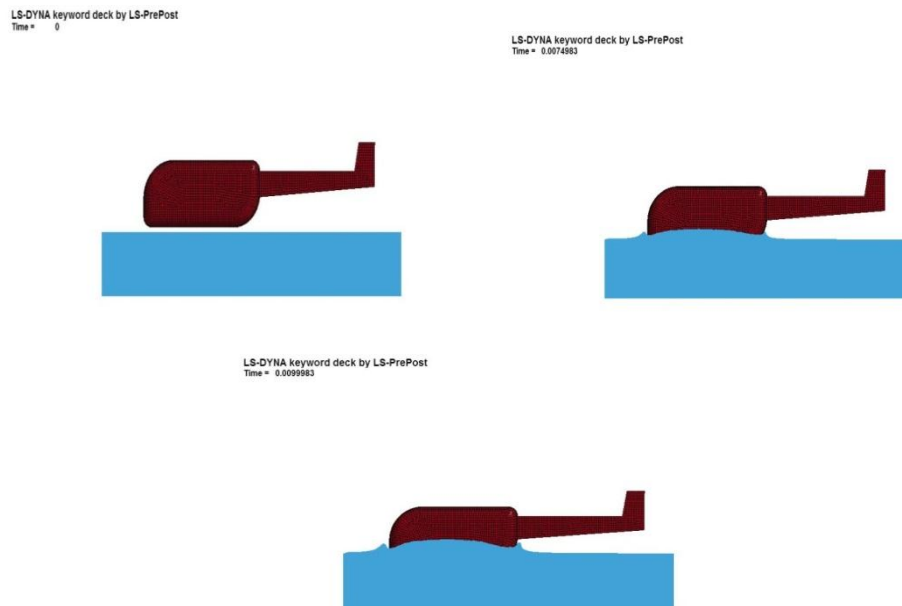


Figure 5.8. SPH simulation of rotorcraft in water.

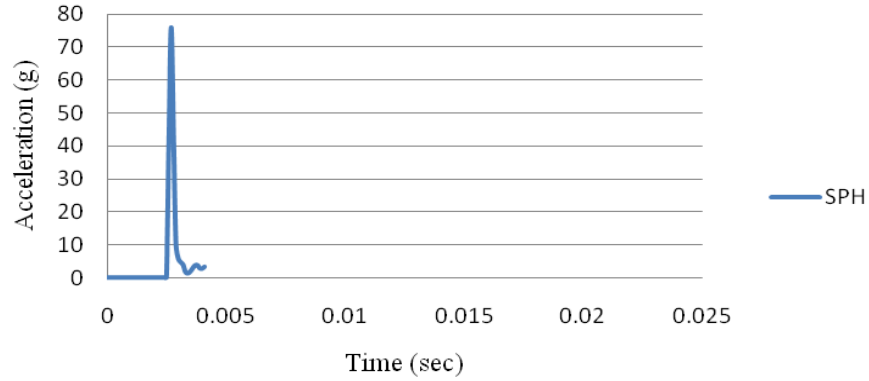


Figure 5.9. Graph of acceleration vs. time for rotorcraft in water in SPH simulation.

5.1.2 Rotorcraft Soil Impact

Rotorcraft soil impact was also similar to that of the soil impact analysis with the penetrometer, which was discussed in Chapter 4. In the analysis, the rotorcraft model was meshed as described in Section 5.1.1, and mesh size and the mesh used for the soil impact analysis on rotorcraft were the same as for the soil test discussed in Chapter 4. The model was scaled to the dimensions of the soil pit, and analyses were carried out on soil using Lagrangian, ALE, and SPH simulations.

Figure 5.10 (a) shows the initial stage of a helicopter before landing on soil, and Figure 5.10 (b) shows the helicopter after landing on soil. In the analysis, the floor of the helicopter fuselage was badly damaged, which might have caused severe injuries to the legs of the co-pilot. A bump in the floor of the helicopter was also observed.

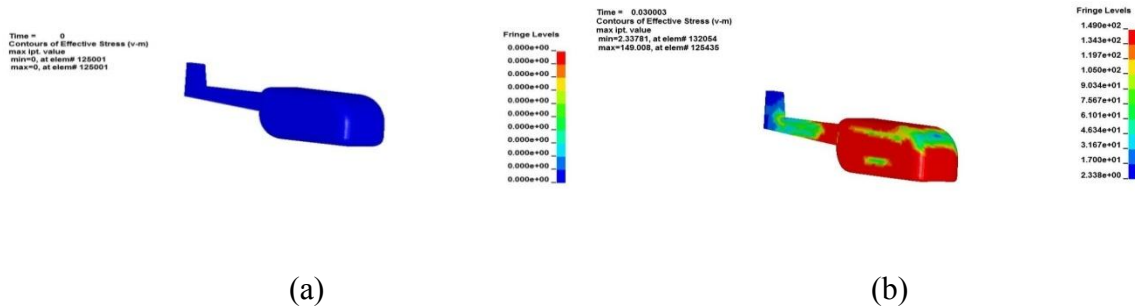


Figure 5.10. Deformation of rotorcraft in soil.

5.1.2.1 Lagrangian Approach for Soil Impact Analysis with Rotorcraft

In the Lagrangian method, all LS-DYNA cards and soil material properties were similar to the previous analysis on soil as discussed in Chapter 4 (4.2.1). The mesh and material properties of the rotorcraft were similar to the analysis conducted on water. In the analysis, soil and rotorcraft material properties were similar to that found in Tables 4.1 and 5.1. Deformation of the rotorcraft resulting from soil impact was more than deformation of the rotorcraft as the result of water impact, which can be seen in Figure 5.11.

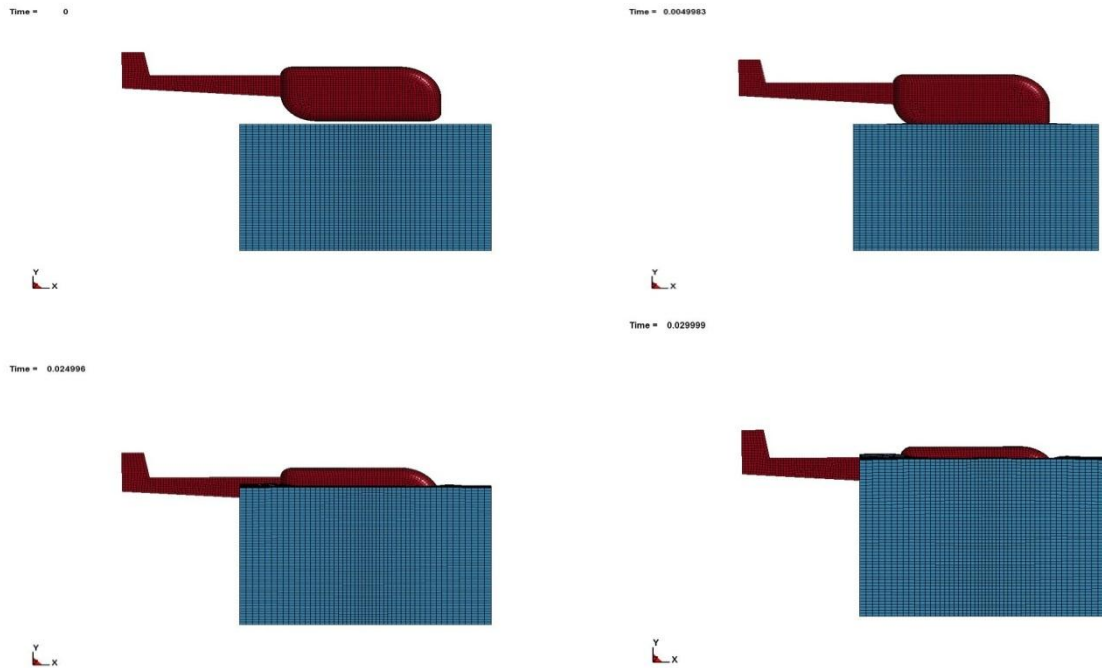


Figure 5.11. Lagrangian simulation of rotorcraft in soil.

Figure 5.12 shows the relation of acceleration vs. time where the curve is plotted with respect to the helicopter model. In this graph, the maximum acceleration obtained is 99 g, and another peak can be seen around 80 g. The g-value obtained in the experiment near the co-pilot's seat is around 69 g, which is assumed to be the center of gravity.

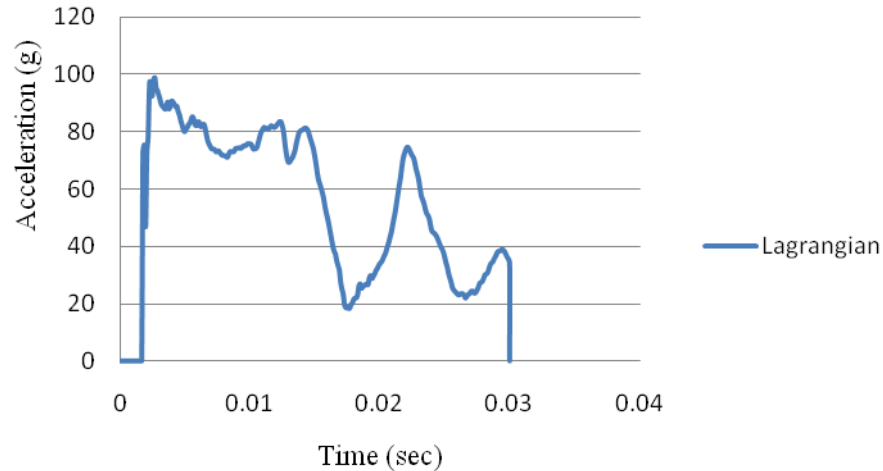


Figure 5.12. Graph of acceleration vs. time for rotorcraft in soil in Lagrangian simulation.

5.1.2.2 ALE Approach for Soil Impact Analysis with Rotorcraft

In the ALE method, the LS-DYA card and soil material properties were similar to that of the previous analysis on soil, as discussed in Chapter 4 (4.6.2). The mesh and material properties of the rotorcraft were similar to that of the analysis conducted on water. Soil and rotorcraft material properties were similar to those shown in Tables 4.1 and 5.1. The material dimensions of the air was 0.91x0.91x0.13, and the mesh seeding was 50x50x11. Another ALE approach was adapted to complete the soil impact analysis. In SECTION_SOLID, the 11th formulation (multi-material group) was replaced with the 12th formulation. The INITIAL_VOID card was used to nullify the mesh material properties and was considered for the air material analysis. This mesh was constructed above the soil body mesh so that the material properties would flow into the empty meshes, thus causing the formation of a crater, which can be seen in Figure 5.13. The deformation of the rotorcraft was greater with respect to ALE method, as evidenced in Figure 5.13. The dimensions of the soil and air were similar to that discussed in Chapter 4 (4.1.2).

Figure 5.14 is a graph of acceleration vs. time in the ALE simulation. The maximum acceleration obtained is 89 g. Moreover, another minimal peak occurs around 80 g, and the g-

value obtained near the co-pilot's seat in the experiment when the rotorcraft impacted the water is around 69 g.

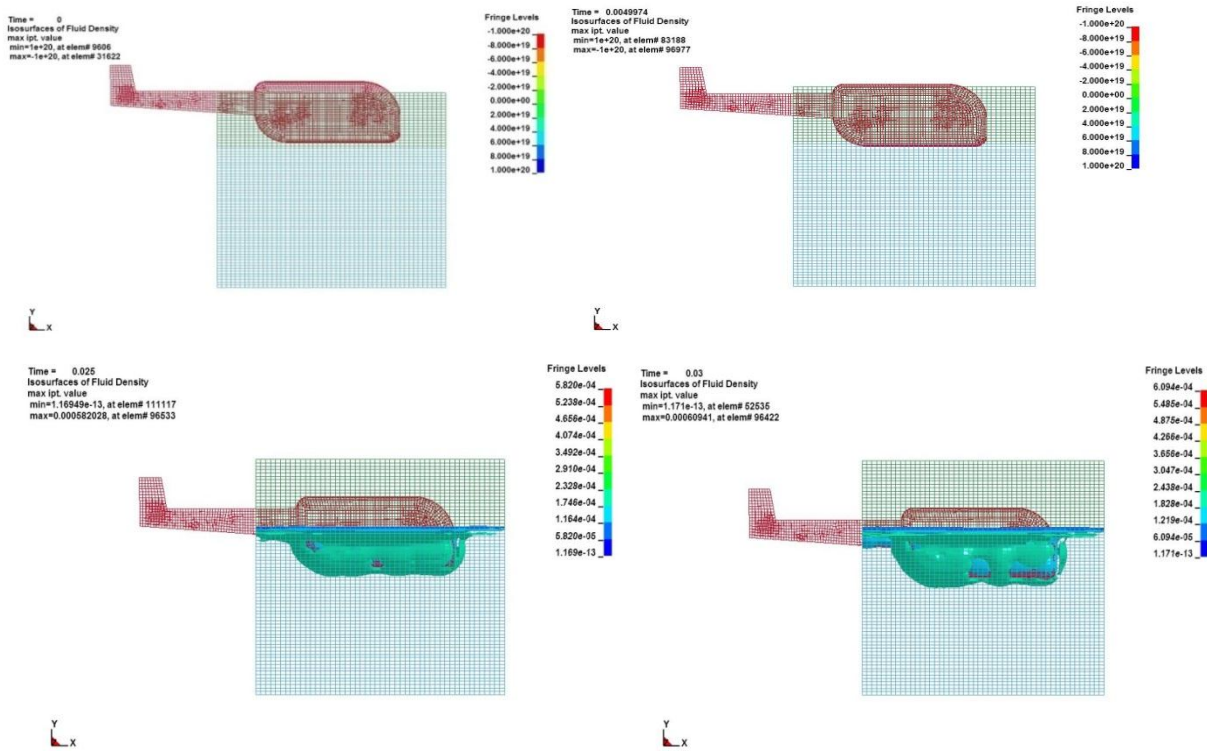


Figure 5.13. ALE simulation of rotorcraft in soil.

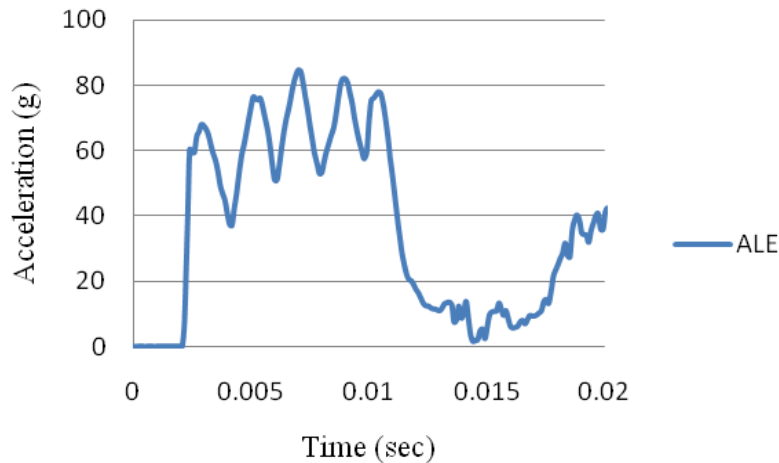


Figure 5.14. Graph of acceleration vs. time for rotorcraft in soil in ALE simulation.

5.1.2.3 SPH Approach for Soil Impact Analysis with Rotorcraft

The SPH soil impact analysis with the rotorcraft was carried out in the same way as in the SPH analysis of the soil test, as discussed in Chapter 4 (4.1.3), and all cards and contacts were similar. This simulation replicated the actual crater formation during impact on soil, as shown in Figure 5.15.

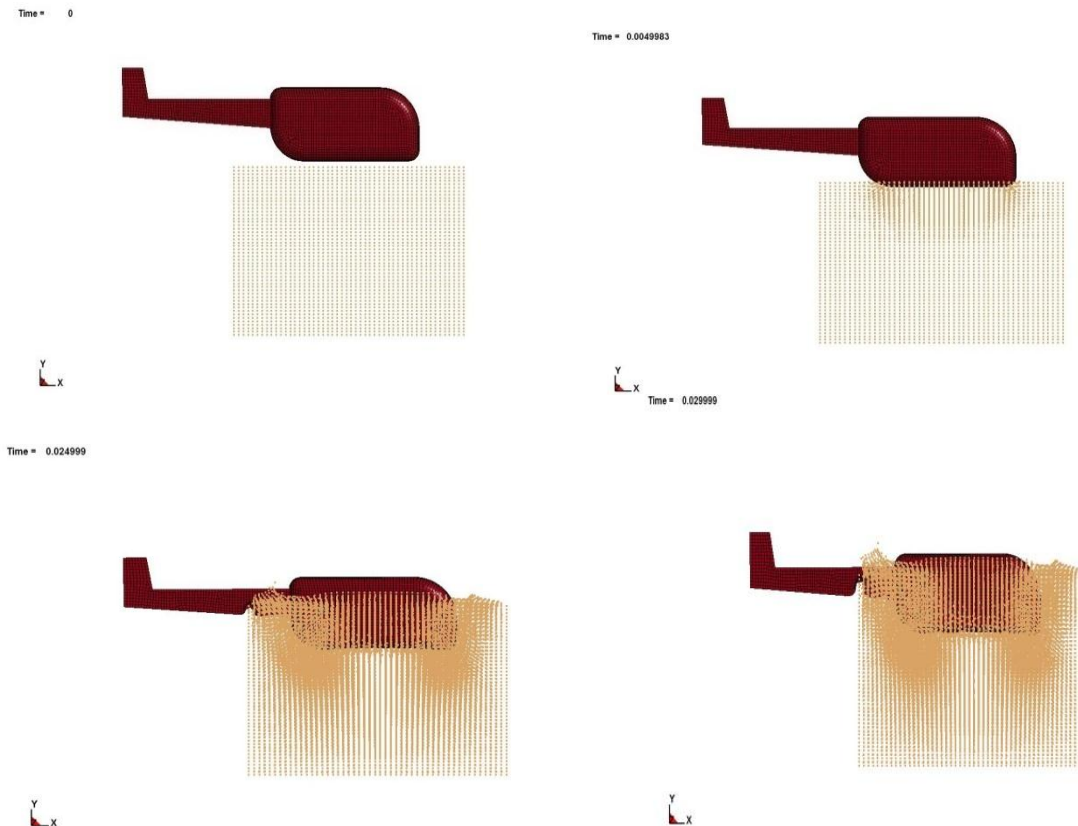


Figure 5.15. SPH simulation of rotorcraft in soil.

Figure 5.16 is a graph showing acceleration vs. time in the SPH simulation. The maximum acceleration obtained is 75 g, and another minimal peak occurs around 40 g. The g-value obtained in the experiment near the co-pilot's seat is around 69 g when the rotorcraft impacted in water. Because the water pit was small, as the helicopter hit the constraint region, the acceleration predominantly increased to 120 g. After 0.015 sec, the results obtained were nullified or not considered. Only the initial and second peaks were considered for this analysis.

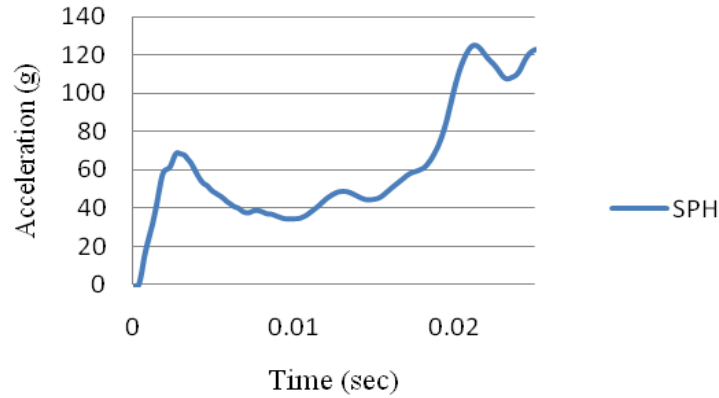


Figure 5.16. Graph of acceleration vs. time for rotorcraft in soil in SPH simulation.

5.2 Airplane Impact Application

5.2.1 Airplane Soil Impact

The aircraft was modeled in CATIA V18 and meshed in Hypermesh. The soil pit dimensions were 0.91x0.91x0.61 m, and the mesh seeding was 50x50x50. In the airplane impact analysis on soil, the mesh used for the soil was biased with density 1.5, and the properties were those previously shown in Tables 4.1 and 4.2. The airplane fuselage was used for studying the impact. The biased mesh was used in the impact region to properly capture results of the aircraft analysis. The aircraft prototype is shown in Figure 5.17, which also shows the data-collection points. The soil test was similar to that conducted on the helicopter or rotorcraft. In the soil test, the airplane was impacted on a soil body at a velocity of 25 m/sec. The material properties of the airplane are listed in Table 5.2.

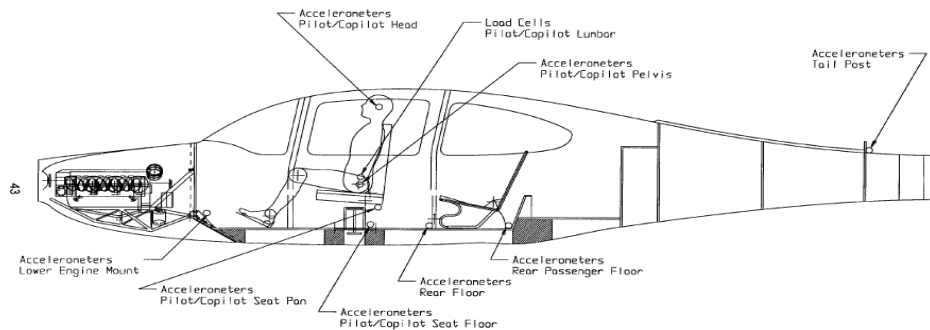


Figure 5.17. Airplane with dummy used in experiment [35].

TABLE 5.2

MATERIAL PROPERTIES OF AIRPLANE [27]

Young's Modulus (Pa)	2.1e11
Poisson's Ratio	0.33

Deformation as the aircraft impacted the soil can be seen in Figure 5.18. Figure 5.18 (a) shows the aircraft before impact, and Figure 5.18 (b) shows the final deformation of the aircraft after analysis. In this experiment, the behavior of the aircraft was similar to that observed for the rotorcraft. The engine of the airplane was pushed inside the cockpit, which would have severely damaged the co-pilot's legs, according to the findings of research conducted by Vaughan and Hayduk [18]. The aircraft deformation plot is similar to Lagrangian, ALE, and SPH simulations of aircraft impact with the soil surface.



Figure 5.18. Deformation of airplane.

5.2.1.1 Lagrangian Approach for Soil Impact Analysis with Airplane

The Lagrangian analysis was similar to that described in previous Chapters 4 and 5 (4.1.1 and 5.1.2.1), and the material properties are similar to that described in Chapter 4 on soil impact. The Lagrangian simulation is shown in Figure 5.19, where the fuselage penetrating the soil can be observed. The velocity with which the airplane impacted the surface of the soil was 25 m/sec, and at this high velocity, a large deformation can be observed in Figure 5.19. In the analysis, the

engine-mounted structure impacted the ground first, again causing severe damage to the co-pilot's leg region, as shown in Figure 5.19 (b).

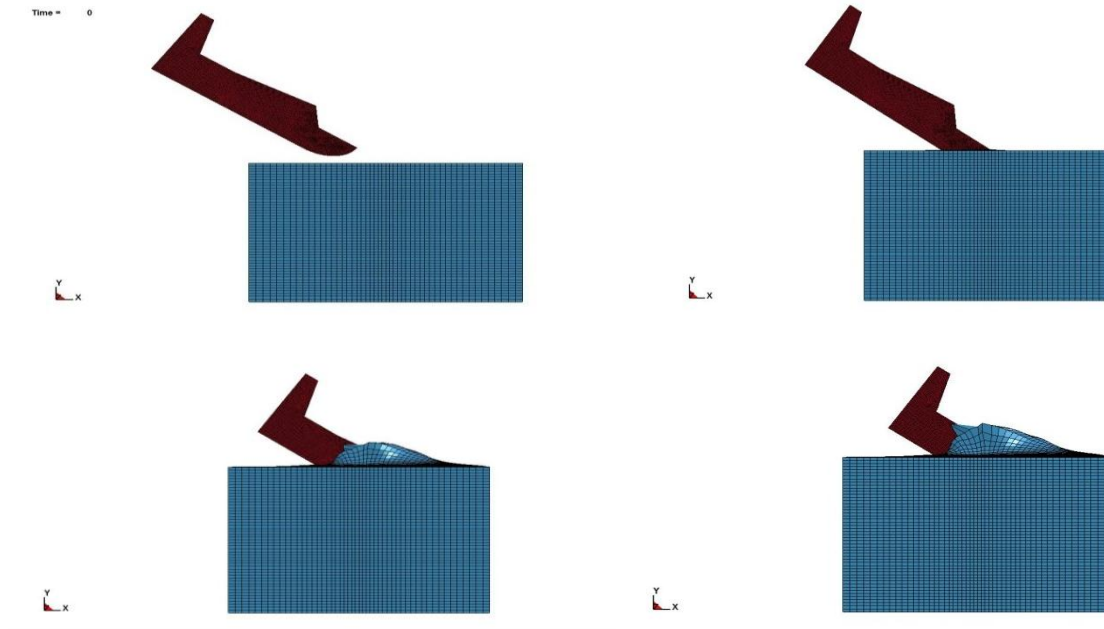


Figure 5.19 Lagrangian simulation of airplane in soil.

The maximum peak obtained during simulation is 22.5 g, as shown in Figure 5.20. The second highest peak is at 21 g. The results in the analysis are similar to results obtained from the research of Ramalingam [26], where the acceleration in the soil impact analysis ranges between 20 g and 25g.

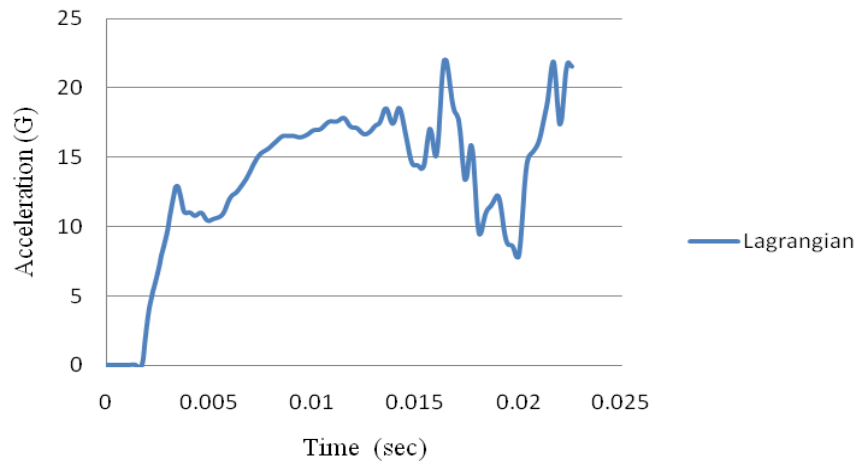


Figure 5.20. Graph of acceleration vs. time for airplane in soil in Lagrangian simulation.

5.2.1.2 ALE Approach for Soil Impact Analysis with Airplane

In this analysis on aircraft, soil and air material properties were assigned from those described in Chapter 4. In Figure 5.21, the red region is considered soil, and the blue region is the air. The ALE simulation can be carried out using the multi-material group, but in this analysis, the initial void-based method was used. In the void-based method, air was used as a medium with null properties. By using the `CONSTRAINED_LAGRANGE_IN_SOLID` card, the Lagrangian mesh underwent deformation during the impact analysis.

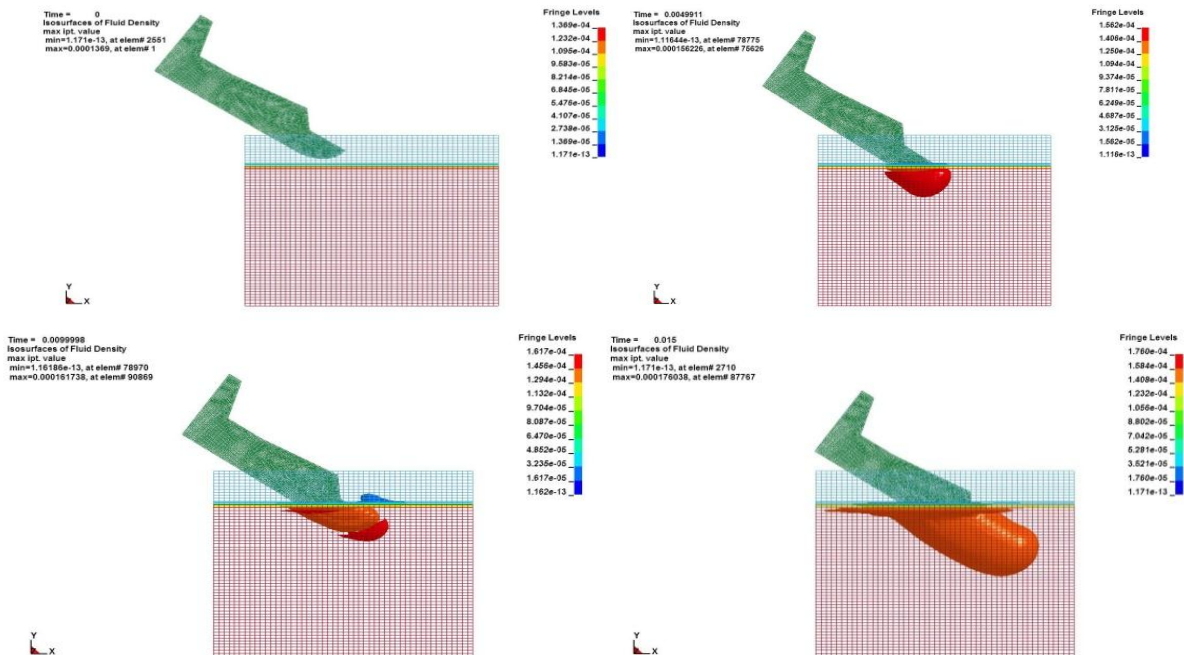


Figure 5.21. ALE simulation of airplane in soil.

The graph in Figure 5.22 shows the acceleration vs. time in the ALE simulation. With the help of this graph, the g-values were calculated during the soil impact analysis. The maximum peak obtained during simulation is at 21 g, and the second highest peak is at 19 g. The results in this analysis are similar to results obtained from Ramalingam [26], where the acceleration plots in the soil impact analysis ranged between 20 g and 25g. It can be seen in Figure 5.22 that at 0.02

sec, the aircraft is coming to a halt as it impacts the soil, which is assumed to be accurate in a real-time simulation.

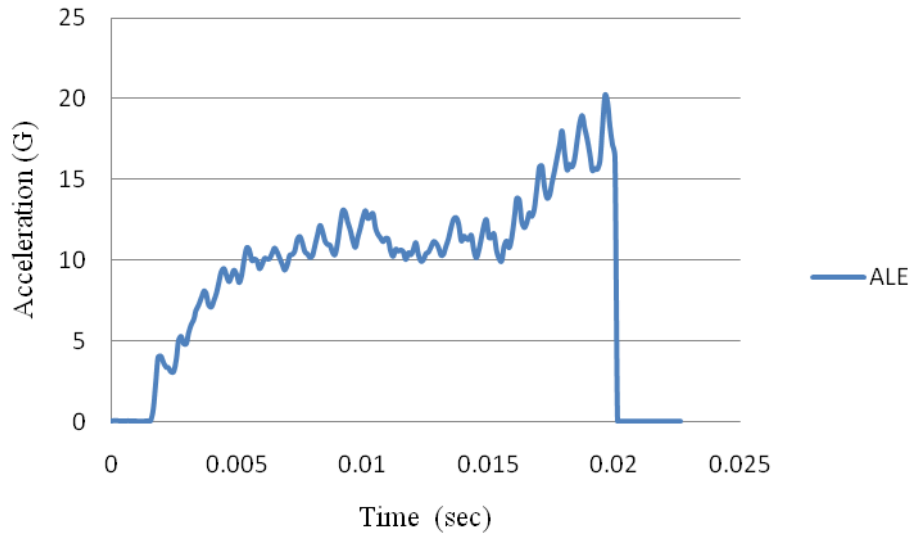


Figure 5.22. Graph of acceleration vs. time for airplane in soil in ALE simulation.

5.2.1.3 SPH Approach for Soil Impact Analysis with Airplane

In the SPH approach, Lagrangian mesh was replaced with SPH mesh, and nodes replaced the elements. The card CONTACT_AUTOMATIC_SURFACE_TO_NODE was used to assign the contact. In addition, all other cards were similar to that of the Lagrangian mesh. As discussed previously, the Lagrangian formulation used in the Lagrangian method and SPH method are similar. Figure 5.23 shows the SPH simulation of the airplane impacting soil.

The graph in Figure 5.24 shows acceleration vs. time in the SPH simulation. With the help of this graph, the g-values were calculated during the soil impact analysis. The acceleration graph obtained during simulation has a maximum peak of 20.5 g, and the second highest peak is 18 g. The results of this analysis are similar to those obtained from the research of Ramalingam [26], where the acceleration plots in the soil impact analysis range between 20 g and 25 g.

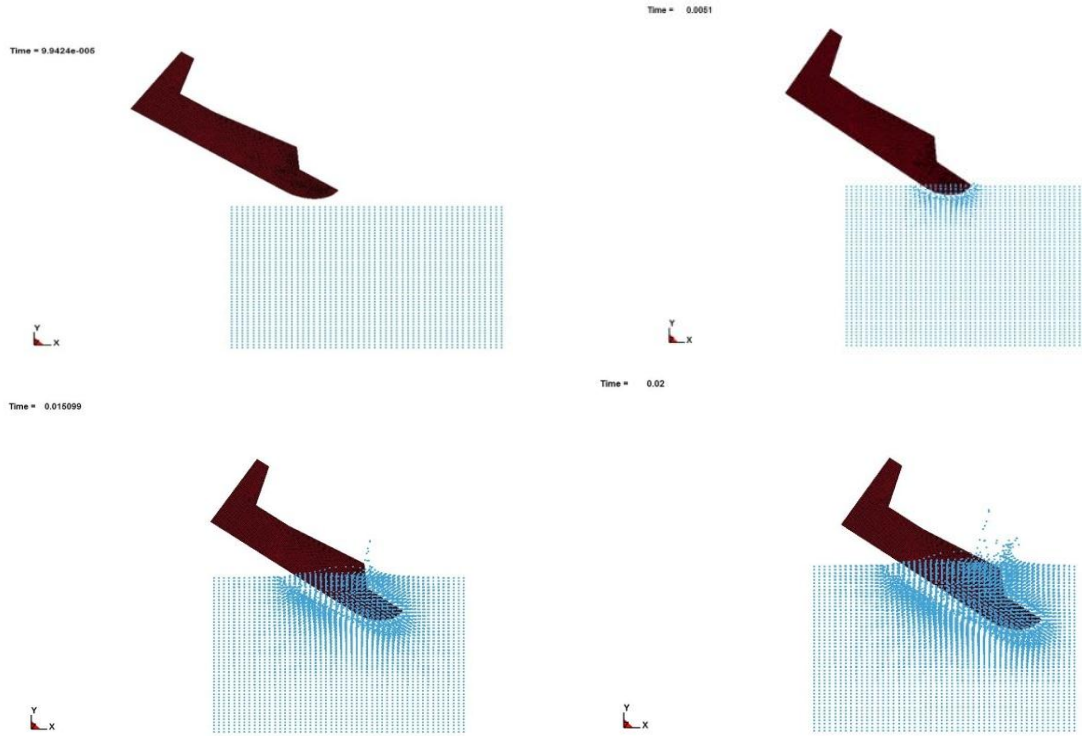


Figure 5.23 SPH simulation of airplane in soil.

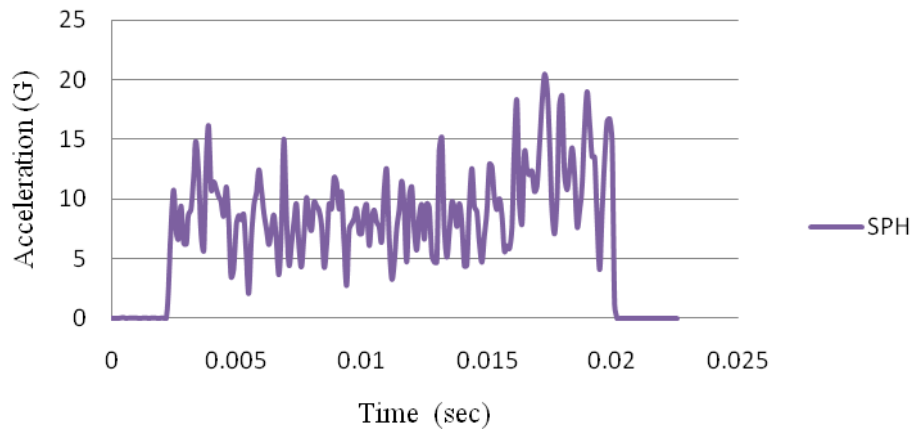


Figure 5.24. Graph of acceleration vs. time for airplane in soil in SPH simulation.

5.2.3 Airplane Water Impact

An aircraft was subjected to a water impact to obtain the g values, which were used as load conditions for further analysis. The material properties of the aircraft used in this soil test are listed previously in Table 5.2. The deformation of the aircraft is shown in Figure 5.25.

Figure 5.25 (a) shows the initial stage, and Figure 5.25 (b) is after 0.02 seconds of impact, which is considered the end time of the simulation. The velocity of the aircraft was the same as mentioned in the soil impact analysis of the aircraft.

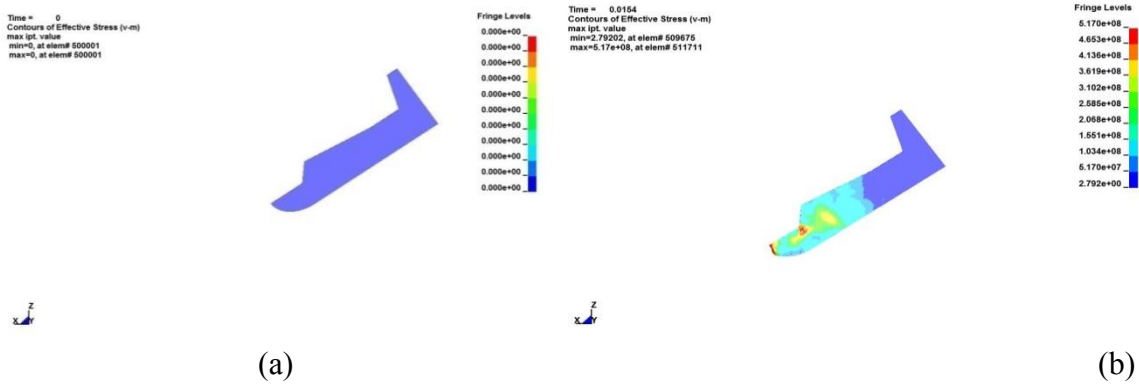


Figure 5.25. Deformation of airplane with respect to von Mises stress.

5.2.3.1 Lagrangian Approach for Water Impact Analysis with Airplane

The Lagrangian analysis for an airplane water impact was also similar to the analysis carried out in the Lagrangian methods mentioned earlier in Chapter 5 (Section 5.1.1.1). In this simulation, a splash formation during impact is shown in Figure 5.26.

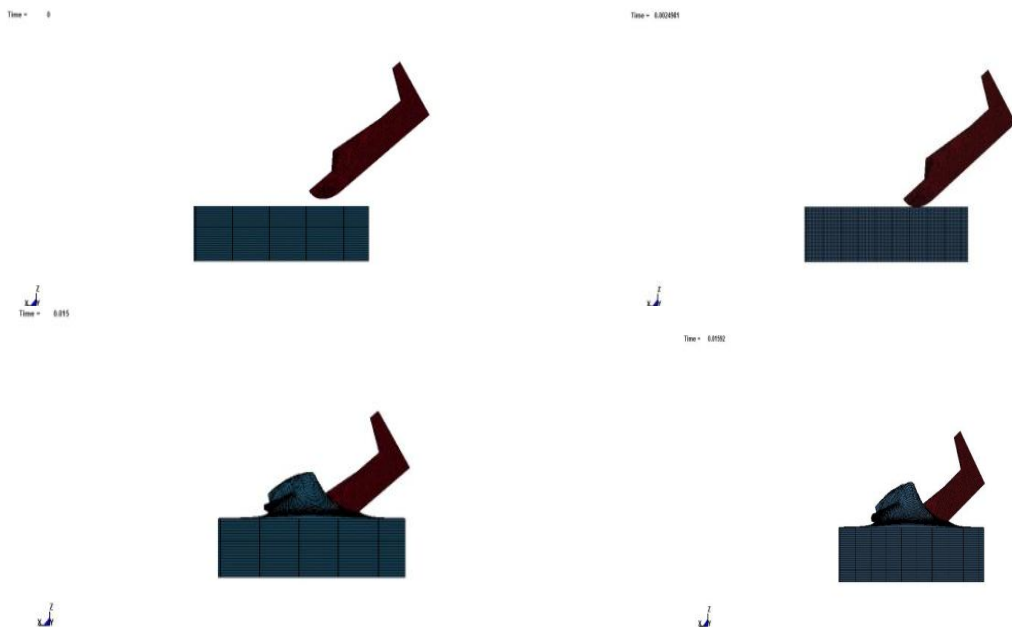


Figure 5.26 Lagrangian simulation of airplane in water.

Figure 5.27 shows a graph of acceleration vs. time carried out in the Lagrangian simulation. The maximum peak is around 7 g, and the second peak is at 5.7 g. This graph is in the acceptable range because water impact has less g-value than soil impact, so the obtained g-value is less than 20 g to 25 g.

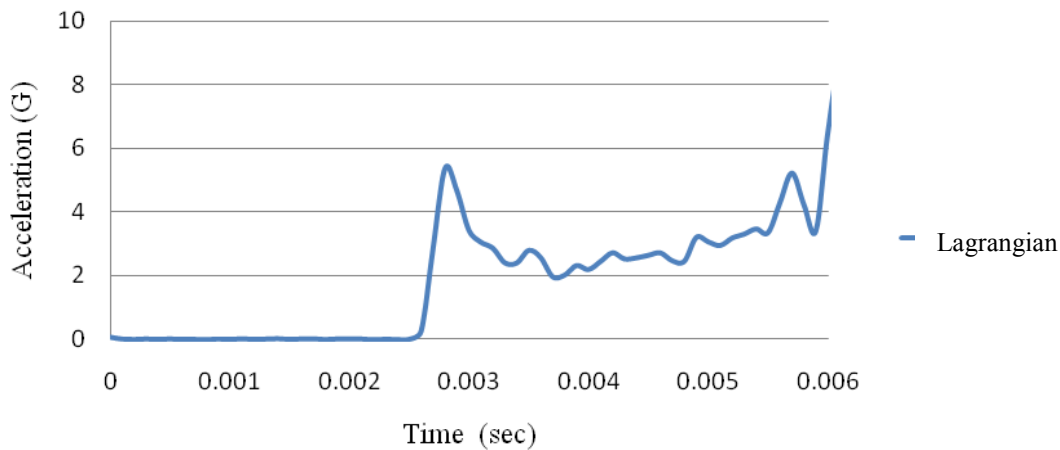


Figure 5.27 Graph of acceleration vs. time for airplane in water in Lagrangian simulation.

5.2.3.2 ALE Approach for Water Impact Analysis with Airplane

The ALE analysis for and airplane water impact is the same as mentioned earlier. This simulation was carried similarly as for the other ALE simulations and analyses except for the fuselage. Figure 5.28 shows the simulation at a particular time step. Splash formation and deformation during impact can be observed in this simulation. This analysis was carried out on a multi-material group. The air model was MAT_NULL and EOS_LINEAR_POLYNOMIAL. This simulation failed because of a negative advection cycle, and it ran for only 0.01 second.

Figure 5.29 shows a graph of acceleration vs. time for aircraft in water in the ALE simulation. The analysis termination time is 0.006 second. The maximum peak is around 27 g, and the second peak is 25.7 g. This graph is in the acceptable range because water impact has less g-value than soil impact, so the value obtained is less than 20 g to 25 g. The graphs obtained

from this analysis failed to obtain a solution due to an advection algorithm and boundary conditions. Rotations, translations, and deformation of the solid elements should be within the solid element range, and this imposed restrictions to the topology and thus a limit in deformation, which introduced a stabilize energy to solve the model, and this might skew results. The results from this analysis took a much longer period of time to obtain, compared with results from the Lagrangian and SPH analyses.

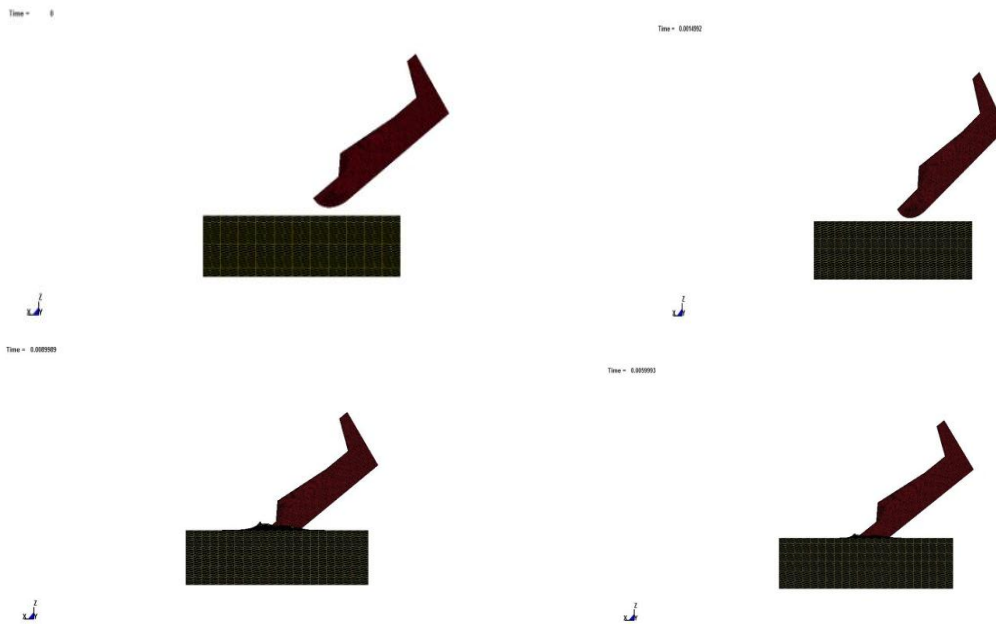


Figure 5.28 ALE simulation of airplane in water.

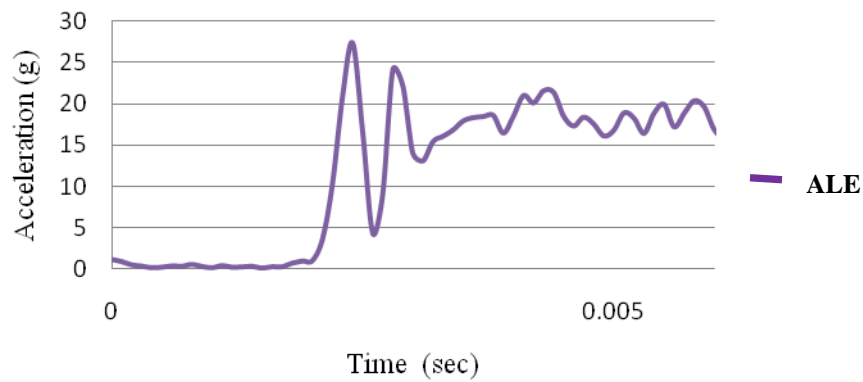


Figure 5.29. Graph of acceleration vs. time for aircraft in water in ALE simulation.

5.2.3.3 SPH Approach for Water Impact Analysis with Airplane

In the SPH simulation of aircraft in water, shown in Figure 5.30, the Lagrangian element mesh replaced the nodes in the SPH mesh. Contact was made using the CONTACT_AUTOMATIC_SURFACE_TO_NODE card, and all other cards were similar to that of the Lagrangian mesh. As discussed earlier, the Lagrangian formulation used in the Lagrangian method and SPH are the same. Therefore, the process boundary condition and some LS-DYNA cards are similar. Overall, the analyses on water impact SPH results were found to be acceptable.

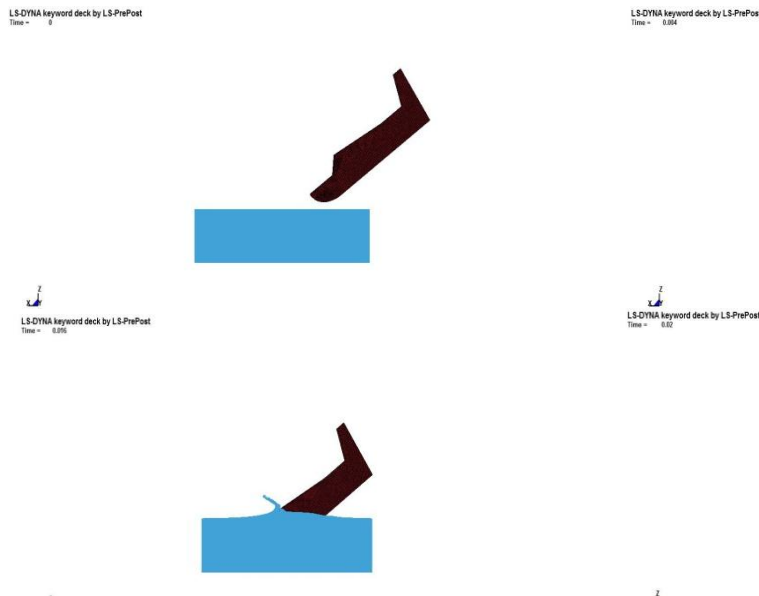


Figure 5.30. SPH simulation of aircraft in water.

The graph in Figure 5.31 shows the acceleration vs. time for an aircraft in water in the SPH the simulation. The analysis termination time was 0.006 seconds. The maximum peak is around 3.8 g, and the second peak is at 3 g. This graph is in the acceptable range because the water impact has a lower g-value than the soil impact. Therefore, the value obtained is less than 20 g to 25 g.

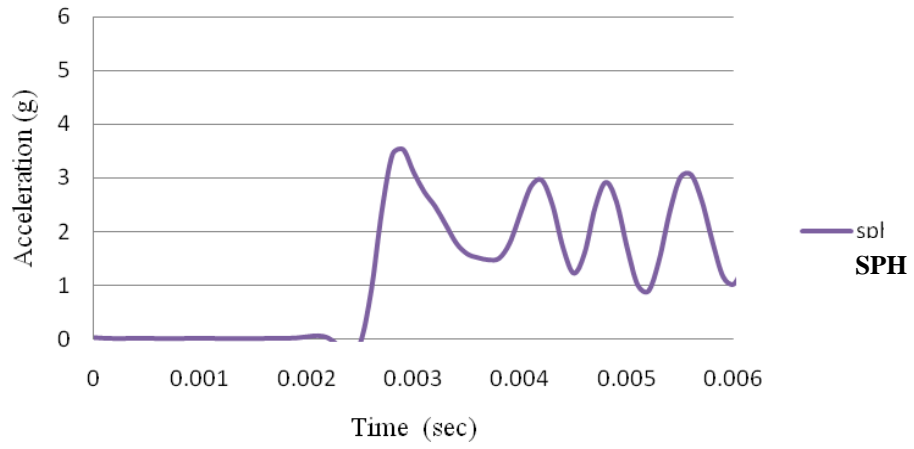


Figure 5.31. Graph of acceleration vs. time for aircraft in water in SPH simulation.

CHAPTER 6

MODEL COMPARISON, RESULTS, AND DISCUSSION

Results from the previous chapter are discussed in detail in this chapter, and results from the Lagrangian, ALE, and SPH simulations are summarized with the experimental results.

6.1 Water Impact Simulation

6.1.1 Rigid Ball Impact on Water

A rigid ball was subjected to impact on a water surface using Lagrangian, ALE, and SPH formulations, and the results were validated with the Pentecote and Kindervater experiment. Figure 6.1 shows acceleration vs. time from the Lagrangian, ALE, and SPH approaches, and they are summarized with the experimental results.

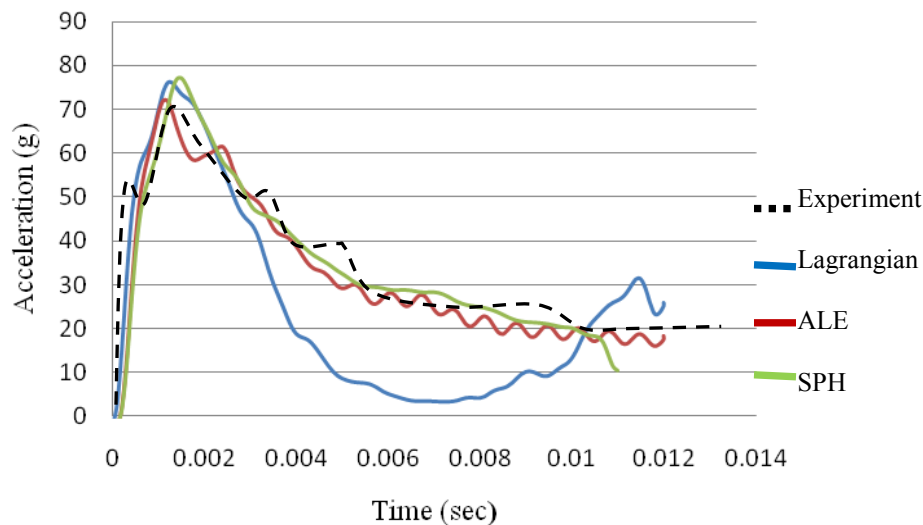


Figure 6.1. Graph of acceleration vs. time for rigid ball impact on water comparing Lagrangian, ALE, and SPH approaches to experiment.

The experimental graph in Figure 6.1 indicates a peak at 69 g. From the FEA, the Lagrangian simulation showed a peak of 75 g, the ALE method showed a peak of 72 g, and the SPH method showed a peak of 75.5 g. Comparing the results with the experiment, the ALE approach showed a promising result. Due to similarities in the Lagrangian and SPH simulations,

similar results were observed. ALE results were close to the validation graph because of the capability of solving a fluid-structure interaction under high-velocity conditions.

6.1.2 Ball Impact on Water in Flask

A rigid ball was subjected to impact on water in a flask using Lagrangian, ALE, and SPH formulations, and the results were validated with the experimental water material properties found by Randhawa [27]. Figure 6.2 shows a graph of displacement vs. time for the ball impact on water in a flask in Lagrangian, ALE, and SPH simulations compared to the experiment.

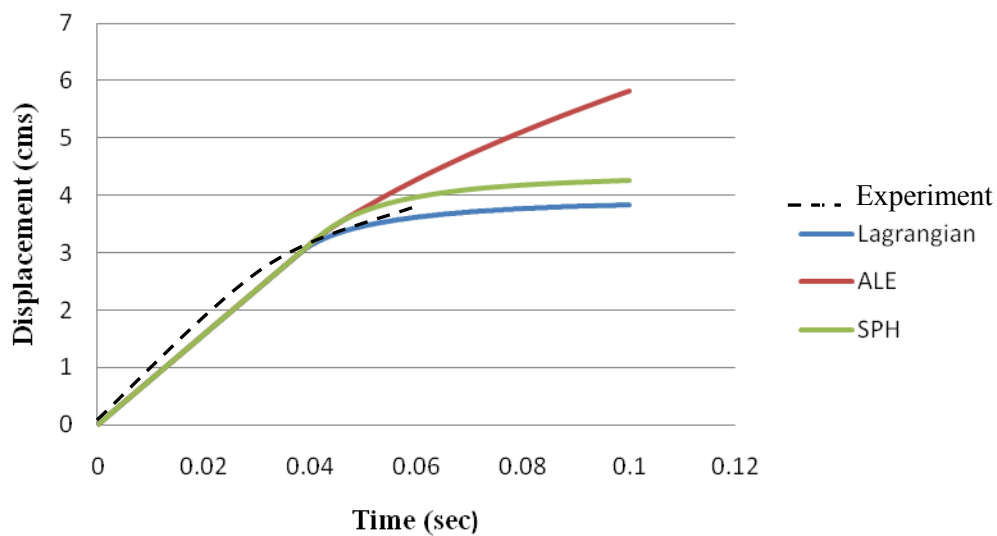


Figure 6.2. Graph of displacement vs. time for ball impact on water in flask comparing Lagrangian, ALE, and SPH approaches to experiment.

The Randhawa [27] experiment was carried out on the displacement parameter. A graph from the Lagrangian method was almost similar to the experimental graph. Due to similarities in the formulations of Lagrangian and SPH, the same results were observed. The ALE approach showed a linear curve, which is almost similar but not accurate, compared to that of the Lagrangian method. In impact analysis, the displacement parameter is less significant than the acceleration parameter, which was revealed in the literature review in Chapter 2.

6.1.3 Penetrometer Impact on Water Surface

In the penetrometer study, a rigid body was subjected to impact on a water surface using Lagrangian, ALE, and SPH formulations. An acceleration vs. time graph was extracted from the experiment carried out by Jackson and Fuchs [31] and validated water material properties at free-fall instances. As can be seen in Figure 6.3, there is correlation between the experimental approach, and the Lagrangian, ALE, and SPH approaches.

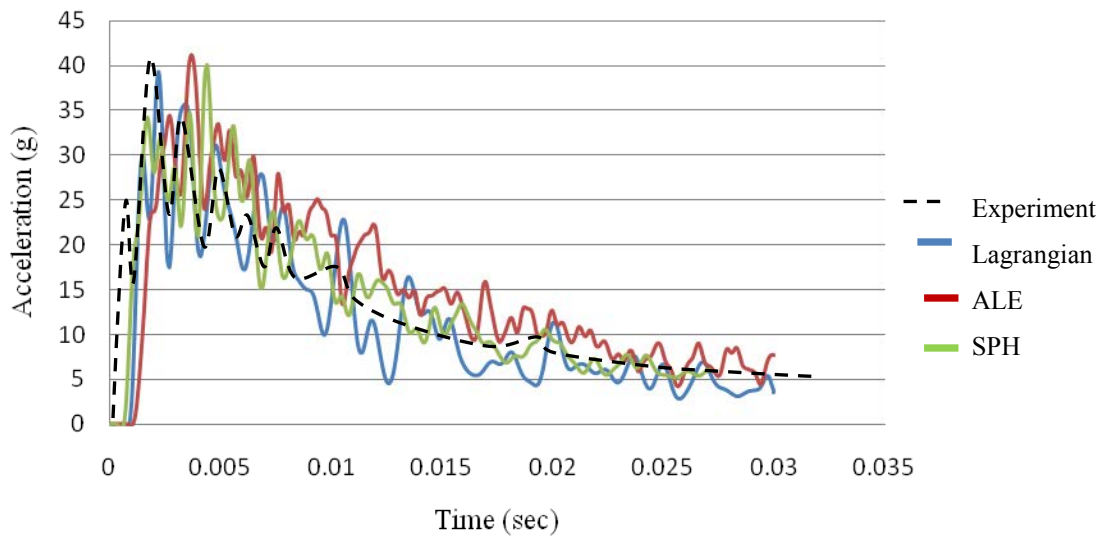


Figure 6.3. Graph of acceleration vs. time for penetrometer impact on water comparing Lagrangian, ALE, and SPH approaches to experiment.

As shown in Figure 6.3, the initial peak obtained from the experiment is at 39 g, in comparison to the initial peaks obtained from Lagrangian, ALE, and SPH analyses, which are 40 g, 42 g, and 39.5 g, respectively. ALE results were close to the experimental results. Due to similarities in the Lagrangian and SPH formulations, the same results were observed. The ALE approach has shown promising results due to its capability of solving the fluid-structure interaction. As mentioned earlier, high-velocity impact analysis using the ALE approach has shown promising results, but in a free-falling condition, all approaches had similar results, with an error percentage in the Lagrangian method of 2.56%, ALE method of 7.69%, and SPH

method of 1.28%. In finite element analysis, the error percentage should be below 10% due to model and boundary condition irregularities.

6.2 Soil Impact Simulation

A penetrometer was subjected to impact on the surface of soil to validate the soil properties using Lagrangian, ALE, and SPH formulations. The results were validated with the experiment conducted by Fasanella et al. [19]. The g-values obtained had to be in the range of 16 g to 21 g. In Figure 6.4, the formulations are correlated with the experimental results, and a comparison is made between Lagrangian, ALE, and SPH approaches.

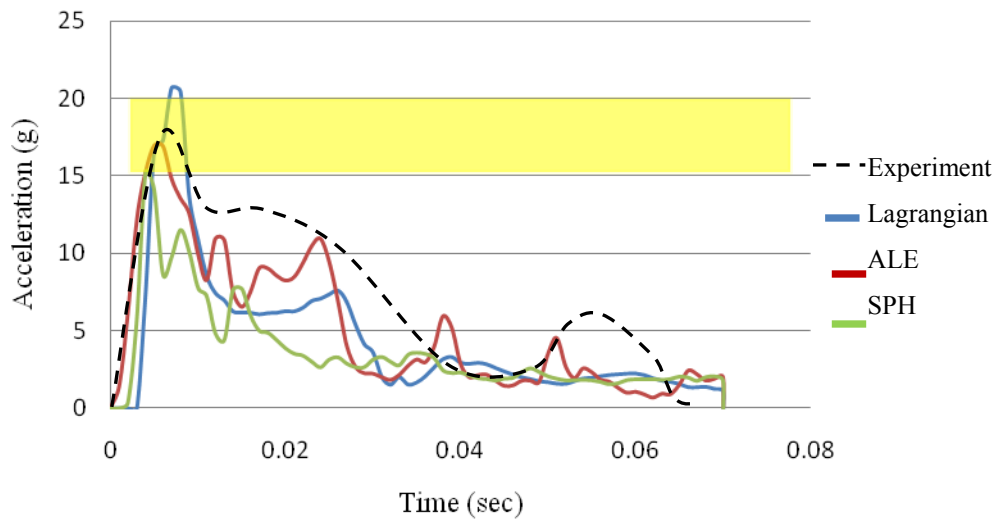


Figure 6.4. Graph of acceleration vs. time for soil test comparing Lagrangian, ALE, and SPH approaches to experiment.

As can be seen in Figure 6.4, results ranged from 16 g to 20 g, as indicated by the yellow strip. The peak values of the finite element method are as follows: Lagrangian 17 g, ALE 21 g, and SPH 15.6 g. Lagrangian results were close to the experimental results. Due to similarities in Lagrangian and SPH formulations, the same results were observed. Material properties of soil are similar to material properties of foam (MAT 5) in LS-DYNA, but for solving soil problems,

the FSI equation of state must be mentioned for effective use of the ALE formulation. The robust application of the Lagrangian formulation made this method effective for solving soil problems.

6.3 Rotorcraft Impact Simulation

6.3.1 Rotorcraft Impact on Water

Simula Technologies Inc. and the U.S. Army conducted a ditching experiment [36] where a rotorcraft frame was subjected to impact on the surface of water using an accelerometer to obtain g-values. Similar tests were conducted in FEA using Lagrangian, ALE, and SPH formulations, and the results correlated with the experimental results, as shown in Figure 6.5.

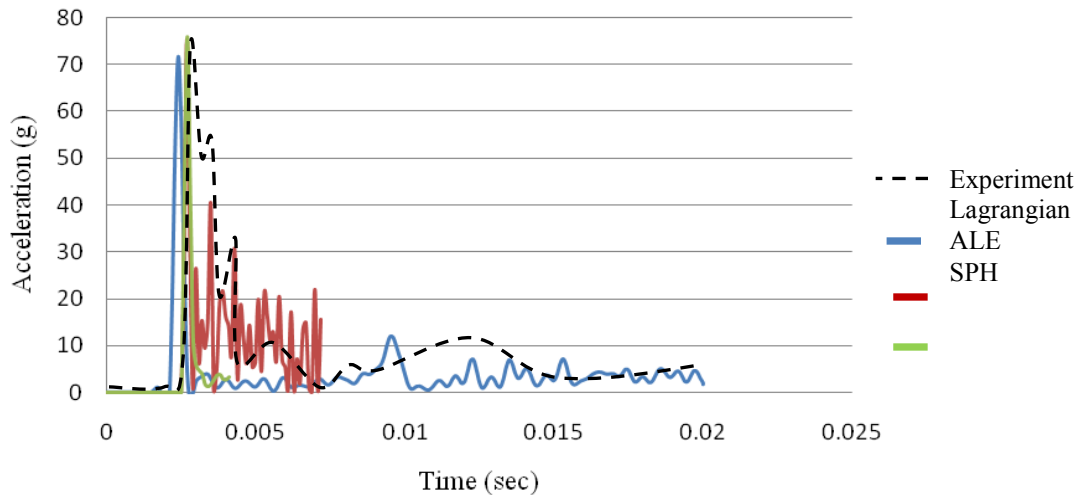


Figure 6.5. Graph of rotorcraft impact on water comparing Lagrangian, ALE, and SPH approaches to experiment.

As shown in Figure 6.5, the initial peak obtained in the experiment is 69 g, and the initial peaks obtained in the Lagrangian, ALE, and SPH analyses are 71 g, 70 g, and 74 g, respectively. The ALE results were closest to the experimental results. Due to similarities in the Lagrangian and SPH formulations, the same results were observed. The ALE approach has shown promising results due to its capability of solving the FSI. Because of its robust application, the Lagrangian approach has resulted in obtaining good results compared to that of the ALE approach, but the computational time required by the ALE formulation is more than that required for the

Lagrangian formulation. Considering the computational times required for all formulations, the Lagrangian method took less time than the other methods: 72 hours of wall clock time with an 8 core CPU to complete 0.02 sec of analysis, in comparison to the ALE method completing 0.08 sec of analysis, and SPH method completing 0.05 sec of analysis. However, in impact analysis, the initial peak determines the g-value at the initial time period, and the integration time step for the ALE method was smaller than that of the Lagrangian method.

6.3.2 Rotorcraft Impact on Soil

The rotorcraft model was impacted on water using Lagrangian, ALE, and SPH formulations with the validated soil material property. In this analysis, the water pit was replaced with a soil pit to determine the g-value at impact. Figure 6.6 shows a comparison study of the Lagrangian, ALE, and SPH formulations.

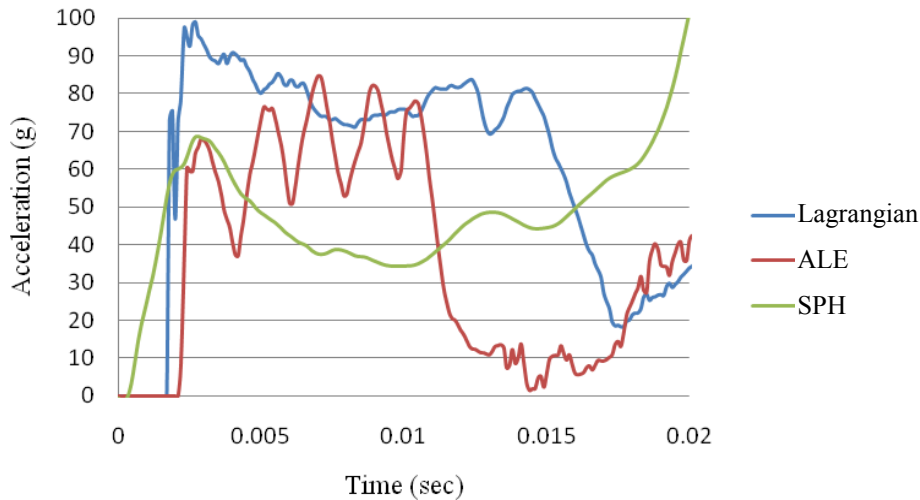


Figure 6.6. Graph of acceleration vs. time for rotorcraft impact on soil comparing Lagrangian, ALE, and SPH formulations.

In Figure 6.6, the initial peaks obtained from the Lagrangian, ALE, and SPH methods are 100 g, 85 g and 65 g, respectively. The ALE method did not show promising results due to its capability of solving the fluid-structure interaction. Material properties of soil are similar to material properties of foam (MAT 5) in LS-DYNA, but for solving the FSI, the equation of state

must be mentioned for effective use of the ALE formulation. The robust application of the Lagrangian formulation made this method effective for solving soil problems. The SPH method did not show promising results, because in high-impact analyses, the nodes could not withstand the increased impact due to the exhibited high accelerations. Another reason was contact of the node to surfaces.

6.4 Airplane Impact Simulation

6.4.1 Airplane Impact on Soil

The Vaughan and Hayduk [18] experiment was conducted to determine the angle of approach during a crash landing. The g-value where data is acquired was determined to be at the center of the gravity, which in the co-pilot seat location. Results obtained from the experiment were between 20 g and 25 g. Figure 6.7 shows a comparison of acceleration vs. time for an airplane impact on soil using Lagrangian, ALE, and SPH formulations.

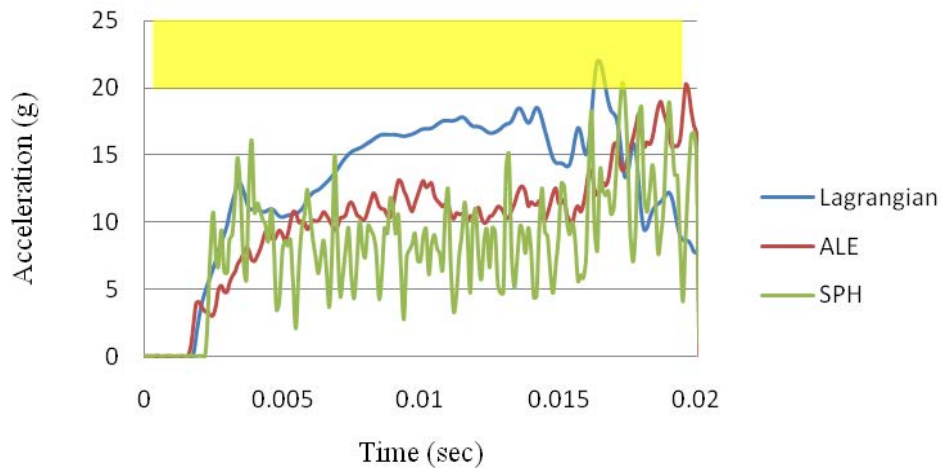


Figure 6.7. Graph of acceleration vs. time for airplane impact on soil comparing Lagrangian, ALE, and SPH formulations.

Figure 6.7 shows the initial peak obtained from the analysis and is summarized as follows: the obtained g-value in the Lagrangian method is 22 g, in the ALE method is 20 g, and in the SPH method is 20 g. The experimental results ranging from 20 g to 25g is indicated by the yellow strip in Figure 6.7. The Lagrangian results were close to the experimental results, but due

to formulation similarities in the Lagrangian and SPH method, the same results were observed. The ALE method did not show promising results due to its capability of solving the FSI. Material properties of the soil are similar to material properties of foam (MAT 5) in LS-DYNA for solving the FSI. The equation of state must be mentioned for effective use of the ALE formulation. Because of robust application of Lagrangian formulations, this method is effective for solving soil problems.

6.4.2 Airplane Impact on Water

The airplane model considered in this analysis used the same material properties as those from previous soil impact analyses. Figure 6.8 shows a graph of acceleration vs. time comparing Lagrangian, ALE, and SPH approaches. In this analysis, the g-value obtained should be less than 20 g. However, previous rotorcraft analyses have proven that water impact analysis has less g-value compared to soil impact analysis. A free falling body condition was assumed for the rotorcraft impact analysis on water. In the airplane analysis, a high-velocity parameter was considered as a condition of impact, so that Lagrangian, ALE, and SPH formulations could be studied for a high-velocity impact.

Experimental results range from 20 g to 25 g for a water analysis g-value to be less than a soil analysis g-value. As shown in Figure 6.8, the initial peaks obtained from the analysis are 6 g in the Lagrangian method and 4 g in the SPH method. The ALE approach results did not match the limits, with a g-value higher than 20 g. Lagrangian and SPH analyses results were nearer the required g-values, the maximum peaks being 5 g and 3 g, respectively, as can be seen in Figure 6.8. These obtained g-values were similar due to the similarity in Lagrangian and SPH formulations. The ALE value was assumed to have closer results to the experimental value, but ALE has not shown promising results in spite of its capability of solving the fluid-structure

interaction. As can be seen in this graph, it is not advisable to use the ALE method to simulate impact analysis.

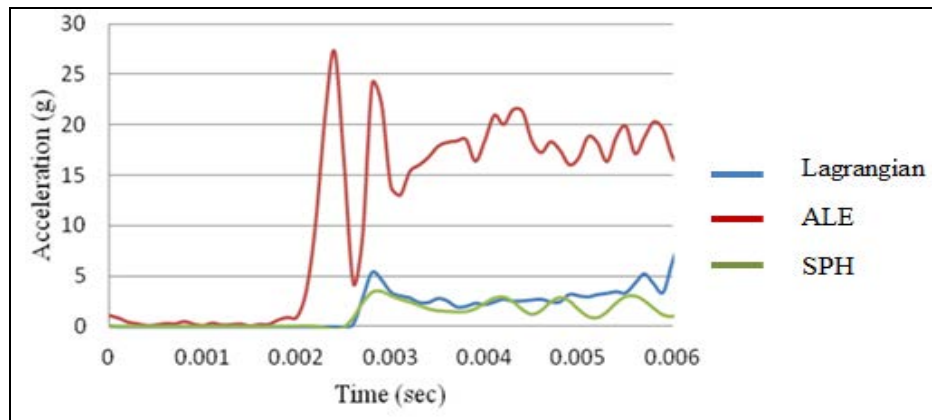


Figure 6.8. Graph of acceleration vs. time for aircraft impact on water comparing Lagrangian, ALE, and SPH formulations.

6.5 Summary

Table 6.1 shows a summary of the g-values obtained in this study.

TABLE 6.1

SUMMARY OF G-VALUES

Application / Method	Rigid Sphere	Penetrometer in water	Penetrometer in soil	Rotorcraft on Water	Airplane on Soil	Rotorcraft on Soil	Airplane on Water
Experimental	69	39	16-21	69	20-25	-	-
Lagrangian	74	38	17	72	22.5	96	7
ALE	72	42	21.5	74	21	86	25.7(*)
SPH	76	39	15.5	75	21	72(#)	4

(*) Failure was due to advection algorithm and boundary conditions. Rotations, translations, and deformation of the solid elements should be within the solid element range restrictions imposed to the topology. Because it has a limit in deformation, this introduced a stabilize energy to solve model, and the result was skewed.

(#) In the SPH approach, the node meshing order will be distorted from the order, which causes the impact body to merge into it. This phenomenon is caused by improper contact between the nodes and surfaces. Contact between the two surfaces must be either a surface-to-surface or node-to-node contact. For this reason, the results from the rotorcraft soil analysis are skewed.

As shown in Table 6.2, the Lagrangian approach was shown to be effective. For the ALE approach, the time step was dependent on the characteristic length of the element, and for the SPH approach, more nodes were present in the analysis.

TABLE 6.2
COMPUTATION TIME FOR SIMULATION
(8 CORE CPU IN HIPECC)

Approaches	Time taken to complete 0.02 sec
Lagrangian	72 hr
ALE	140 hr
SPH	280 hr

A comparison of deformation of the rotorcraft in water and soil is shown in Figure 6.9 and Table 6.3. The height in these analyses was 2.7 m and the velocity was 7.3 m/sec.

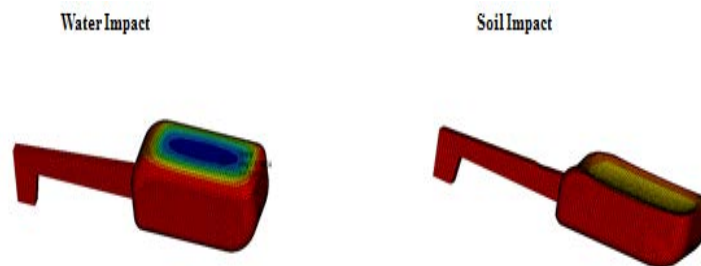


Figure 6.9. Deformation of rotorcraft in water and soil.

TABLE 6.3
DEFORMATION OF ROTORCRAFT IN WATER AND SOIL

Rotorcraft Deformation in Water	Rotorcraft Deformation in Soil
0.001 m (negligible)	0.05 m

CHAPTER 7

CONCLUSIONS AND RECOMMENDATIONS

7.1 Conclusions

Full-scale dynamic certification testing on aircraft and rotorcraft airframes is an expensive and time-consuming process. One reliable solution to reducing this cost is through simple numerical modeling techniques. Advances in computer software allows for analyzing complex systems by using a numerical simulation rather than that of full-scale testing, thus providing low-cost, fast computational time, and the capability of handling large deformations in a crash test. As a result, FEM techniques can be used to carry out these experiments. In this study, different approaches were carried out on water and soil impacts. Because of an aircraft's landing process, airframe structures can be improved in order to resist a crash. The analyses discussed in this study can provide the designer with information about stress distribution in which to model an airplane or rotorcraft in the preliminary state in order to withstand a crash landing, and to observe the stress and principal maximum stress tensor in order to analyze the stress distribution and model the aircraft efficiently

Some observations and conclusions from this study are as follows:

- This study was motivated by the frequent accidents of airplanes and rotorcrafts on water and soil surfaces.
- Finite element material models for the impact on water and soil were developed.
- Three finite element techniques—Lagrangian, ALE, and SPH—were considered for the impact analyses.
- Correlation of Lagrangian, ALE, and SPH data with experimental data was obtained.

- Results obtained in these analyses are similar to those in the experimental data. The error percentage was less than $\pm 10\%$.
- As an example, error percentage was studied using a penetrometer impact on water with the following results: Lagrangian method 2.6%, ALE method 7.7% and SPH method 1.3%. The ALE and SPH approaches showed good results with water and soil impact analysis. However, the Lagrangian approach showed consistency in results.
- In terms of computational time, the Lagrangian technique is faster than ALE and SPH approaches.
- The results from the rotorcraft with water and soil impact analyses indicated that water impact produces 33% less g-value and around 90% deformation compared to that of soil impact, which indicates that impact on water might be safer than impact on soil.
- If study is intended to determine the general deformation behavior or the g-value for structural analyses only, the Lagrangian approach is recommended, if the soil or water is of small interest.

7.2 Future Recommendations

The following recommendations for future work in this area are as follows:

- The study of the stress tensor could be extended and the results used for developing stronger structures, as shown in Figure 7.1.

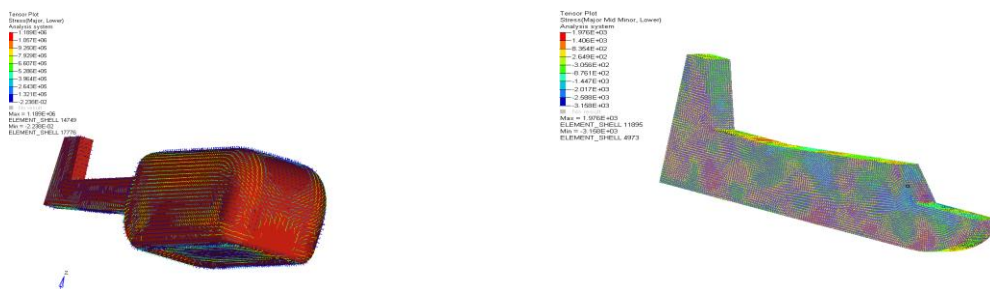


Figure 7.1. Stress tensors for improving structure.

- A detailed study could be carried out on a structure by building a full-scale model of the aircraft and helicopter, including all components, such as the engine, landing gear, etc.
- A more comprehensive method, such as a coupled Lagrangian-Eulerian, could be developed.
- In some cases with the ALE method, a negative advection cycle must be solved.
- Experiments could involve water with waves, unlike these analyses that involved still-water conditions.
- A study involving thermal effects could be conducted.

LIST OF REFERENCES

LIST OF REFERENCES

- [1] Federal Aviation Administration, "Certification of Transport Category Rotorcraft," Advisory Circular AC29-2A, Change 2, pp. 553-559, September 24, 1991.
- [2] Aviation Safety Network, ASN Safety Database summary, <http://aviation-safety.net> [cited April 2011].
- [3] Von Karman, T., "The Impact on Seaplane Floats during Landing," NACA TN-321, October 1929.
- [4] Electronic Code of Federal Regulation, Title 14-Aeronautics and space , chapter 3 , http://ecfr.gpoaccess.gov/t/text/text-dx?c=ecfr&tpl=/fribrowse/Title14/14cfr121_main02.tpl [cited April 2011].
- [5] Johnson, D., "Study on Transport Airplane Unplanned Water Contact," Report No. DOT/FAA/CT-84/3, Federal Aviation Administration, Technical Center, Atlantic City, January 1984.
- [6] Patel, A. A, and Greenwood, R. P. Jr., "Transport Water Impact and Ditching Performance," Report No. DOT/FAA/AR-95/54, March 1996.
- [7] Jackson, K. E., and Fasanella E. L., "Development of an LS-DYNA Model of an ATR42-300 Aircraft for Crash Simulation," *Proc. 8th International LS-DYNA Users Conference*, Dearborn, MI, 2004.
- [8] Society of Automotive Engineers, "Instrumentation for Impact Test," Warrendale, 1995.
- [9] Toso, N. R. S., "Contribution to the Modeling and Simulation of Aircraft Structures Impacting on Water," Doctoral Dissertation, Department of Aerospace Engineering and Geodesy, Universität Stuttgart, 2009.
- [10] Applied Research Associates, Inc, "Constitutive Soil Properties for Cuddeback Lake, CA and Carson Sink, NV," NASA CR, to be published, draft February 2008.
- [11] Liu, G. R., and Liu, M. B, *Smoothed Particle Hydrodynamics. A Meshfree Particle Method*, World Scientific Publishing, 2003.
- [12] Hallquist, John O., *LS-DYNA Theory Manual*, Livermore Software Technology Corp., March 2006.
- [13] Civil Aviation Authority, "Emergency Alighting on Water," British Civil Airworthiness Requirements, Paper No.G779, October 7, 1985.
- [14] <http://www.nasa.gov/centers/langley.html> [cited April 2011].

LIST OF REFERENCES (continued)

- [15] –U.S. Army AVSCOM TR 89-D-22 (Volume A-E),” 1989.
- [16] Society of Automotive Engineers, —Performance Standard for Seats in Civil Rotorcraft, Transport Aircraft, and General Aviation Aircraft,” SAE Aerospace, 2005.
- [17] Wang, J. T., and Lyle, K. H., —Simulating Space Capsule Water Landing with Explicit Finite Element Method,” *Proc. 48th AIAA/ASME Conference*, Waikiki, HI, 2007, pp. 23-26.
- [18] Vaughan, V. L., Jr., and Hayduk, R. J., —Crash Tests of Four Identical High-Wing Single-Engine Airplanes,” NASA TP 1699, April 1980.
- [19] Fasanella, E. L., Jackson, K. E., and Kellas S.,—Soft Soil Impact Testing and Simulation of Aerospace Structures,” *Proceedings of the 10th LS-DYNA Users Conference*, Dearborn, Michigan, June 8-10, 2008.
- [20] Flightsim Aviation Zone, http://www.flightsimaviation.com/data/FARS/part_125.html, [cited April 2011].
- [21] Electronic Code of Federal Regulation, Title 14-Aeronautics and space , chapter 1 , http://ecfr.gpoaccess.gov/cgi/t/text/text-idx?sid=600dd4b347592d4bd9446056f4ec1cbd&c=ecfr&tpl=/ecfrbrowse/Title14/14cfrv4_02.tpl#300 , [cited April 2011].
- [22] Fasanella, E. L., and Jackson, K. E., —Water Impact Test and Simulation of a Composite Energy Absorbing Fuselage Section,” *Journal of the American Helicopter Society*, 50: 150, 2005.
- [23] Pentecote, N., and Kindervater, C., —Airframe Water Impact Analysis Using a Local/Global Methodology,” *Proc. 55th American Helicopter Society International Annual Forum*, Montreal, Quebec, Canada, May 25–27 1999, vol. 1, pp. 680–691.
- [24] Ramalingam, V. K., and Lankarani, H. M., —Analysis of Impact on Soft Soil and its Application to Aircraft Crashworthiness,” *International Journal of Crashworthiness* 7(1): 57-66, 2002.
- [25] Reddy. J. N., *An Introduction to the Finite Element Method*, Tata McGraw-Hill, 2006.
- [26] Ramalingam, V. K., —Finite Element Analysis of Impact on Soft Soil and its Application to Aircraft Crashworthiness and Occupant Safety,” Master's Thesis, Department of Mechanical Engineering, Wichita State University, 2001.

LIST OF REFERENCES (continued)

- [27] Randhawa, H. S., –Finite Element Analysis of Impacts on Water and its Application to Helicopter Water Landing and Occupant Safety,” Master's Thesis, Department of Mechanical Engineering, Wichita State University, 2001.
- [28] Federal Aviation Administration, –FARs Part 25—Airworthiness Standards: Transport Category Airplanes,” Special Federal Aviation Regulation No. 13, December 19, 2000.
- [29] Federal Aviation Administration, –FARs Part 29 -Airworthiness Standards Transport Category Rotorcraft,” 7 August 2006
- [30] Jackson, K. E., and Fasanella, E. L., –Crash Certification by Analysis. Are We There Yet?,” NASA Center for AeroSpace Information, Hanover, Maryland, 2006.
- [31] Jackson, K. E., and Fuchs, Y. T., –Comparisons of ALE and SPH Simulations of Vertical Drop Tests of a Composite Fuselage Section into Water,” *10th International LS-DYNA Users Conference*, 2008.
- [32] Randhawa, H. S., and Lankarani. H. –Finite Element Analysis Of Impacts on Water and its Application to Helicopter Water Landing and Occupant Safety,” *International Journal of Crashworthiness* 8(2): 189-200, 2003.
- [33] Aviation Safety Network, ASN Safety Database summary, <http://aviation-safety.net/database/record.php?id=20100522-0> [cited December 2010].
- [34] Pilotfriend, Ditching aircraft, <http://www.pilotfriend.com/safe/safety/ditching.htm> [cited December 2010].
- [35] Tutt, B. A., and Taylor. A. P., –The Use of LS-DYNA to Simulate the Water Landing Characteristics of Space Vehicles,” *8th International LS-DYNA Users Conference*, Dearborn MI, 2004.
- [36] Richards, M. K., and Kelley, E. –Development of a Water Impact Dynamic Test Facility and Crash Testing a UH-1 H Aircraft onto a Water Surface,” *Proc. 55th AHS International Annual Forum*, Montreal, Canada, 1999.
- [37] Belytschko, T, and Liu, W, *Nonlinear Finite Elements for Continua and Structures*, Wiley, 2000.
- [38] Terry, J., and Hooper. S., –Design and Test of an Improved Crashworthiness Small Composite Airframe-Phase II Report,” NASA SBIR Contract NAS1-20427, Terry Engineering, Andover, KS, October 1997.

LIST OF REFERENCES (continued)

- [39] Laananen, D., Aircraft Crash Survival Design Guide. Volume 2, Aircraft Crash Environment and Human Tolerance, SIMULA, Inc., Tempe, AZ, 1980.
- [40] Jianming, W., and Na, G., –Abrasive Water Jet Machining Simulation by SPH Method,” *International Journal of Advanced Manufacturing Technology* 50(1): 227-234, 2010.
- [41] Jackson, K. E., and Boitnott, R. L., –A History of Full-Scale Aircraft and Rotorcraft Crash Testing and Simulation at NASA Langley Research Center,” NASA TM 20040191337, 2004.
- [42] Bell Helicopter, The Bell Huey II Specification and operational manual, http://www.bellhelicopter.com/MungoBlobs/285/848/UH1Y_PG_3-06_web.pdf [cited April 2011].
- [43] Fasanella, E. L., and Jackson, K. E., –Water Impact Test and Simulation of a Composite Energy Absorbing Fuselage Section,” *International Journal of Crashworthiness*, 6(1): 107-121, 2001.
- [44] Mayo, –Analysis and Modification of Theory for Impact of Seaplanes on Water,” National Advisory Committee for Aeronautics, Washington, D.C., 1945.
- [45] Hallquist, J. *LS-DYNA. Keyword User’s Manual. Version 971*, Livermore Software Technology Corporation, 2007.